ELECTRODYNAMIC STEERING OF ELECTROSPUN POLYMER (PEO) NANOFIBERS

by

Rudolf Kyselica

A Dissertation Submitted to the Faculty of the

DEPARTMENT OF AEROSPACE AND MECHANICAL ENGINEERING

In Partial Fulfillment of the Requirements
For the Degree of

DOCTOR OF PHILOSOPHY
WITH A MAJOR IN MECHANICAL ENGINEERING

In the Graduate College

THE UNIVERSITY OF ARIZONA

2019

THE UNIVERSITY OF ARIZONA
GRADUATE COLLEGE

As members of the Dissertation Committee, we certify that we have read the dissertation prepared by Rudolf Kyselica
entitled Electrodynamic Steering of Electrospun Polymer (PEO) Nanofibers
and recommend that it be accepted as fulfilling the dissertation requirement for the Degree of Doctor of Philosophy.

Eniko T. Enikov — Date: 4/15/2019

Eleonora Tubaldi — Date: 4/15/2019

Mathieu Joerger — Date: 4/15/2019

Roberto Furfaro — Date: 4/15/2019

Final approval and acceptance of this dissertation is contingent upon the candidate's submission of the final copies of the dissertation to the Graduate College.
I hereby certify that I have read this dissertation prepared under my direction and recommend that it be accepted as fulfilling the dissertation requirement.

Dissertation Director: Eniko T. Enikov — Date: 4/15/2019

Acknowledgements

I like to express my deep appreciation to my advisor, Dr. Eniko T. Enikov for his mentorship, patience and guidance he provided me, all the way from the day I decided to apply for a PhD study at The University of Arizona, trough to the completion of this degree. Without his advice, this dissertation would not have been possible. It has been a great experience to work with him.

I thank my committee members Dr. Roberto Furfaro, Dr. Eleonora Tubaldi and Dr. Mathieu Joerger for their time and patience in reviewing this dissertation.

My deepest appreciation goes to my whole family for their countless patience, love, care and support.

I am also grateful for involvement of the following individuals, without whom this work would not have been possible: Dr. Peter P. Polyvas, Gergo Edes, Mohsen Azimi, Benito N. Pimienta, Kyle P. Bearden and Vlad Neagu.

This work was supported by the National Science Foundation under grant number 1462752.

Dedication

This dissertation is dedicated to my beloved wife Mirka for her continuous support, encouragement, patience and love. She has always stood by my side and has sacrificed tremendously, so that I could focus on my dissertation and have the determination to complete it.

Table of Contents

Table of Contents – *Continued*

List of Figures

List of Figures – *Continued*

List of Figures – *Continued*

List of Figures – *Continued*

List of Figures – *Continued*

List of Figures – *Continued*

List of Figures – *Continued*

Abstract

Polymer nanofibers and structures composed of these nanofibers, with their set of physical parameters and material properties are favorable for various biomedical applications. Examples of these are scaffolds for artificial tissue engineering, stents production, or a localized and dosage-controlled medication administration. Because of this, interest in these polymer structures has been increasing significantly over the past decades. To align with the specific set of requirements for different applications, stiffness, porosity, conductivity, biodegradability and other parameters of such structures need to be controlled by adjustment of the nanofiber diameter, fiber‘s organization and used material.

Electrospinning proved itself to be very versatile and inexpensive fiber extrusion technique, capable of nanometer-sized fibers production. For these reasons, electrospinning became the most widely used continuous nanofiber production technique. Since it was developed (early in the 20th century), it has been extensively researched and optimized, especially in terms of the instrument design and in the ability to spin wide variety of polymers. However, the electrospinning process parameters, with their significant impact on the extruded fiber are not yet fully understood. Especially if in combination with different fiber collection techniques. These techniques are designed to achieve a desired fiber alignment or woven fibers. Most commonly used collection technique for aligned fiber collection is a dynamic collector electrode.

This work discusses extrusion, deposition, modeling and applications of aligned electrospun polyethylene-oxide nanofibers. Capability of multiple-axis electrostatic focusing and electrodynamic fiber steering is investigated in a series of experiments, where static electrode was used. Identified minimum required axial component of

the electric field of $E_z = 1.6 \times 10^6\,[V/m]$, needed for fiber extrusion, introduces limitation on electric potential applied to the auxiliary electrodes of the electrospinning device. Consequently, minimum steady-state circular fiber deposit area achieved with implementation of such focusing was found to be $A = 40\,mm^2$ (for 5% PEO in DiH_2O).

Electrodynamic fiber steering, as opposed to the electrostatic focusing, allows to actively steer the fiber into various fiber deposits, dependent of the electric field distribution created inside the device by a set of auxiliary electrodes. The size of the deposit is defined by the frequency of the steering. With linear(1D) fiber steering, sharp line deposit composed of parallel fibers was achieved, with length of the deposit as a function of forcing frequency $L_{1D} = 4.832\,f^{-1.43}\,[m]$ on interval $f = [40\ 200]\,Hz$. Addition of another set of electrodes in plane perpendicular to the first one, allowed for expansion of the line deposit to almost circular. Length of the semi-major axis of the elliptical deposit now follows the function of $L_{2D} = 1.45\,f^{-1.332}\,[m]$ on the same frequency interval. Fiber still undergoes mechanical buckling upon contact with the static collector electrode.

Capability of the developed electrodynamic steering method to deposit parallel fibers is demonstrated on preparation of two different fibrous structures for biomedical application. Both of these structures were prepared with application of 1D electrodynamic steering in combination with slowly rotating collector rod. First is a tubular structure, composed of axially deposited fibers, deposited on a latex substrate, and allowing for its radial inflation without fiber damage. Such structure could be then used as coronary drug-eluting stent. SEM imaging of inflated tube, however suggest certain fiber loss, possibly due to fiber rupture. Second structure is a solid cylinder, with no underlying substrate and composed of highly oriented and straight fibers. Such structure than could be used as a nerve graft for nerve regeneration. SEM imaging of produced cylindrical structure of 1.5 mm in diameter

show very high level of fiber alignment and straightness.

Alongside, the experimental work, two mathematical models of fiber (one assuming solid fiber Kelvin-Voigt material model, second assuming viscoelastic fiber material Maxwell material model) extrusion and deposition are built and evaluated by comparison to experimental results. This way, capability of individual models to predict fiber behavior under various settings of the electrospinning device with electrodynamic fiber steering was examined. To better match the simulation and experimental results, Stokes drag coefficient had to be increased in both models (720 times in Kelvin-Voigt model and 40 times in Maxwell model), to reduce the lateral movement of the fiber. A need for such increase of the air friction coefficient is presumably caused by bending stiffness and bending friction not being implemented into neither of the two models. Then the excessive lateral movement of the fiber is corrected by this increase of air friction. High sensitivity of both models to changes of this friction coefficient suggests that the air drag, even if small, cannot be neglected, as other researchers previously reported.

Chapter 1

Introduction to Electrospinning

1.1 History and Overview

Electrospinning is a fiber extrusion method [8, 9, 10], where electric forces are used to draw a thin, electrically charged threads of polymer or ceramic fibers from a liquid solution or melt.Even though the method is quite old, its more significant improvement came in 1930, when Formhals patented the electrospinning process and basic apparatus. Taylor [11] in 1964, and later in 2004 Reznik et al. [12] studied the mechanism of droplet deformation and disintegration due to the strong electric field, and the initial stage of fiber extrusion. The electrospun fiber behavior and properties were most extensively studied and described by Renecker et al. [8, 10, 13, 14, 15, 16], in a series of articles published since 1995. These articles studied the appropriate device settings, under which the electrospinning technique is capable of producing smooth, continuous nanometer-sized fiber(nanofibers), and generally popularized electrospinning as a nanofiber production technique. Even though various materials can be electrospun, in this work, water-based polyethylene-oxide(PEO) solution of various concentrations was used. PEO was chosen because it is non-toxic and stable under standard pressure and temperature conditions used in the process. Hence, PEO, resp. polymer nanofibers alone will only be discussed.

1.2 Electrospinning Apparatus

The basic laboratory electrospinning apparatus requires a liquid polymer solution container with a blunt needle serving as a spinneret (or a nozzle), a DC high voltage

power source connected to it, and a lower potential collector electrode (usually grounded). Two different approaches can be used to feed the polymer solution into the needle. First is a gravitation force-based method, using the hydrostatic pressure of a polymer solution at rest in opened container. The polymer feed rate, in this case, is a function of height of the fluid column above the needle. For this reason, it is diminishing with the use of the polymer and with its decreasing level in the container. Desired constant pressure can be achieved by high open surface area to container volume ratio, where the level drop over time is negligible. However, increase of the free surface of the polymer solution increases the water evaporation rate and the polymer solidification. This not only changes the properties of the polymeric solution, but eventually causes stoppage of solution flow into a needle and so the electrospinning interruption. For these reasons, syringe pump producing constant velocity flow is mostly used. As it is a closed system, it also prevents the water evaporation from the polymer solution and so keeps constant polymer concentration. The basic electrospinning device with constant solution flow system is shown in Fig. 1.1

As the high DC electric voltage is applied to the spinneret, it creates the electrostatic repulsion forces (internal Coulomb forces) between particles of the polymeric solution inside it. This electrostatic repulsion grows with an increase of the applied potential. Electric charges migrate to the surface and create tangential stresses that deform the meniscus into a cone-like projection, or Taylor cone, at the limit of stability. When the internal Coulombic repulsion overcomes the surface tension, a thin charged liquid jet is ejected from the apex of the Taylor cone. The process of formation of the Taylor cone is depicted in Fig. 1.2

This jet after its ejection still carries its electric charge. Therefore, its particles are still under the influence of repulsive internal Coulomb forces, and the external Coulomb forces, pushing the fiber away from the spinneret in direction to a grounded

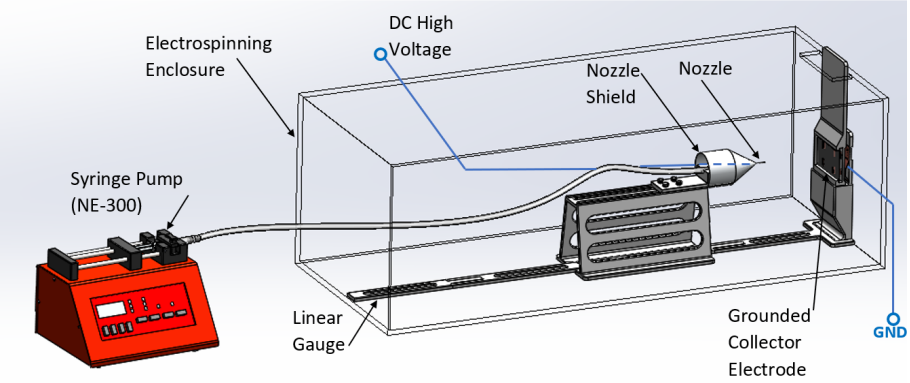

Figure 1.1: Basic electrospinning device containing the electrospinning enclosure, polymeric solution supply, nozzle or spinneret with DC high voltage applied to it and a grounded collector electrode. The conical nozzle shield is not necessary, but was added to shield the electric connection on the nozzle, to keep the electric field distribution inside the device symmetrical.

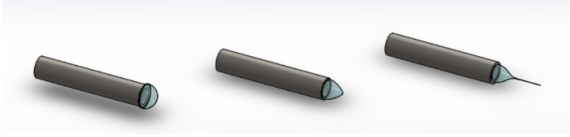

Figure 1.2: Process of creation of the Taylor cone with gradual increase of applied electric potential to a spinnaret containing the polymer solution

collector electrode. As the jet propagates trough the air to the collector electrode, it stretches and solidifies, as the water evaporates from its surface. Because the surface area to volume ratio of this jet is very high, the evaporation rate is high as well. This leads to a dry fiber collection already after about 50-80mm fiber travel distance. The minimum travel distance (nozzle to collector distance) is a function of multiple device working parameters influencing the jet initial thickness, its velocity, evaporation rate and more.

Because of the internal Coulomb forces, the fiber quickly undergoes the electric charge driven bending instability. This means, that the fiber starts to bend and spiral as it progresses to the collector. Researchers have shown, that this liquid

jet at the beginning has a stable, straight segment right after the extrusion, which starts to spiral just after about 10mm. The length of this segment is mostly function of the electric charge carried by the jet, and so the electric potential applied to the spinneret. It was also shown, that this spiraling progresses, and higher orders of bending instabilities starts to build up on top of each other. On top of the bending instability, the fiber also undergoes a buckling instability caused by the collection on the static collector electrode. This occurs when the fiber movement at high axial velocity is suddenly stopped after the contact with the collector. These two instabilities combined, consequently leave the fiber with no macroscopic or microscopic alignment after its collection on the collector electrode. Such fiber deposit can be seen in Fig. 2.4 and a fiber undergoing first three orders of the bending instability is shown in Fig. 1.3. In [8],Reneker at al. proved that the smallest fiber loops (buckles) in the deposit are consequence of the menioned mechanical buckling of the fiber upon contact with the collector. These buckles were of about $10\,\mu m$ in diameter, where the highest observed order of electric charge driven bending instability lead to loops of about $200\,\mu m$. To collect straight fiber- avoid mechanical buckling,researchers generaly use three different techniques, that are in more detail described in 1.4.

1.3 Motivation and Objectives

Interest in electrospinning was renewed about 15 years ago, what can be attributed to electrospinning's adaptability, relative ease of use, and the ability to fabricate nanomiter-sized fibers. Such polymer nanofibers have in many applications very significant benefits over other micro-structures or thin film membranes. Structures composed of nanofibers inherently have very high surface area to volume ratio, what is especially beneficial for tissue engineering, as it provides sufficient surface for the cell attachment. For some tissue engineering applications, like vascular

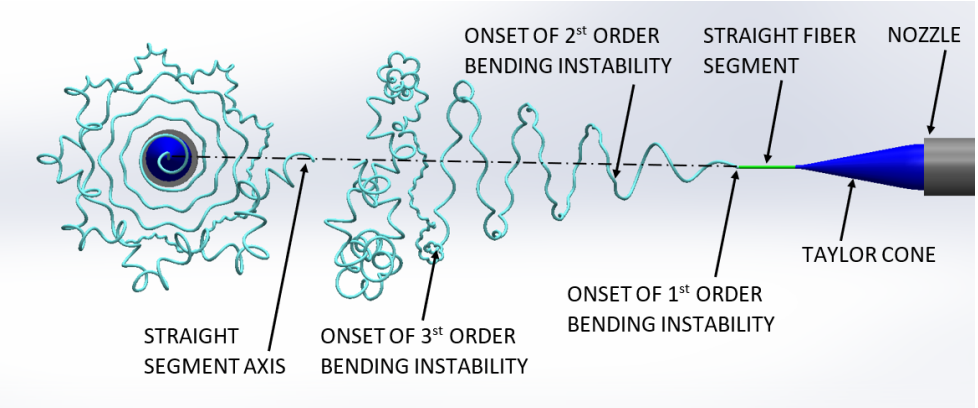

Figure 1.3: Illustration of the polymer fiber after the extrusion in electrospinning device. After short straight segment fiber undergoes the electric charge bending instability. First three successive orders of bending instability are shown.

graft or bone cell ingrowth, with required pore diameters of $20 - 60\,\mu m$ [17] resp. $70 - 100\,\mu m$ [18], randomly deposited nanofibers create ideal scaffold. This is one of the benefits of the electrospinning process, as it affords the opportunity to engineer scaffolds with micro to nanoscale topography. In this case, achieving high porosity similar to the natural extracellular matrix (ECM) by deposition of differently oriented, loosely layered nanofibers[19]. Pore size control is important for another electrospun microstructure, which is medication delivery. Drugs ranging from antibiotics and anticancer agents to proteins, DNA, and RNA can be incorporated into such electrospun structure and release rate can be controlled by its pore size and density.

Orientation and organization of the fiber also allows control over the bulk mechanical properties and biological response of scaffolds. A wide variety of spinnable polymers also allows to design the biodegradability of such electrospun polymer microstructures as required by the application, achieving needed mechanical properties and stability of the structure, so it provides sufficient support and regulation for the cell activities. Aligned, electrospun polymer fibers have shown

considerable promise in nerve regeneration, both in vitro and in vivo [20]. This is of extreme importance, as the mature neurons do not replicate- they don‘t undergo cell division. In minor nerve defect, axons (long fibers of a neuron cell) can bridge the gap trough the formation of fibrin cable and Bungner bands. However, in larger lesions, denuded peripheral nervous system axons are unable to regenerate inherently[21]. There are two approaches to nerve regeneration of such major damage.

First is the use of autografts to bridge the larger gaps, what however leads to a permanent functional loss at the donor site (as a segment of another nerve is used to bridge the gap). Also, this method often leads to a painful neuroma formation, nerve permanent compression or a compliance mismatch [22].

Second, to avoid the negative impacts of autografts, use of artificial nerve grafts. This offers a viable alternative to the conventional autografts to treat neural defects [23]. In the case of larger nerve gaps, creation of the fibrin cable and Bungner band formation is compromised. For this reason, scaffolds with well defined architecture, that supply directional support are desirable. Researchers have found, that aligned nanofiber scaffold provide such support and they determine the direction of the neurite extension [24]. Schematic of such nerve regeneration is shown in Fig. 1.4 [1].

Another application of the tube consisting of axially oriented fibers could possibly be an inflatable catheter or a stent. In this application, the tube needs to support high radial strains without rupturing. Test results and SEM images of such tubes and scaffolds are described in chapter 6 of this work.

Even though the application of highly oriented electrospun nanofibers are well known, preparation of microstructures consisting of such fibers, deposited on any substrate is still problematic. In the following section 1.4, different approaches

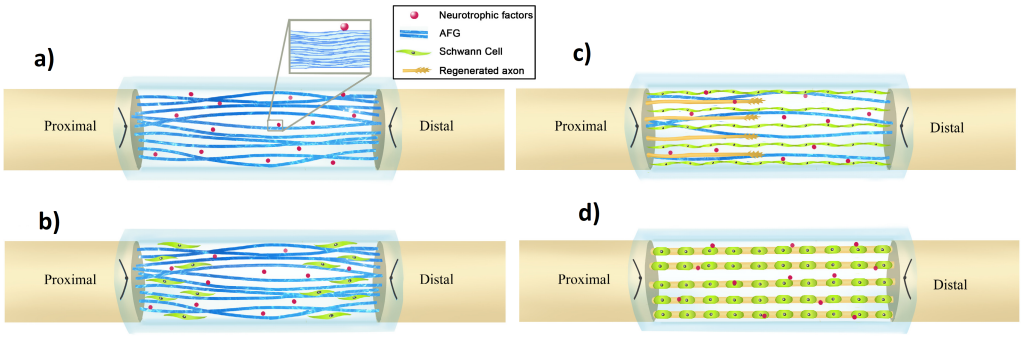

Figure 1.4: Summarized Schematic of regenerative process occurring within AFG@CST. (a) AFG implantation: AFG was implanted to bridge the proximal and distal nerve stumps; (b) Cell cable formation: Schwann cells migrate from the proximal and distal nerve stumps, align and proliferate along AFG forming a biological tissue cable ; (c) Newly regenerated axonal sprouting: axons regrowth along this biological tissue cable toward the distal targets; (d) Myelination of regenerated axons: Schwann cells switch to a myelinated phenotype and associated with regenerated axons forming mature myelinated axons [1]

to collection of aligned fibers are described. However, none of these methods is universal, material effective and without need of material manipulation - mechanical transfer or organization. This work is focusing on development of such method, that would consistently lead to a deposition of aligned fibers of certain properties, by application of steering, external electric field to the electrospinning device.

1.4 Fiber Deposition Control

Researchers, in effort to collect straight fibers, are implementing various mechanisms to the electrospinning apparatus. The three major collection techniques can be recognized, and are listed here in such order, that the first is the most widely used and last is the least used.

1.4.1 Dynamic collector electrode

Most often, rotating drum or mandrel with the axis of rotation perpendicular to the fiber propagation direction is used [25, 26, 27]. Fiber then collects on the surface of this dynamic collector and is winded around it. If the circumferential velocity equals the fiber velocity, and so the collector is winding the fiber at the same rate as at which it is produced, straight and parallel fibers can be obtained. If the circumferential velocity was lower than optimal - the fiber would not be fully straightened, and if higher than optimal - the fiber would be torn into pieces. Applying this technique, researchers were able to achieve not only straight fibers, but also various fiber alignments, if the collector was able to move along or rotate about another axis [28]. Fig. 1.5 shows examples of use of such dynamic collectors and aligned fibers that were collected.

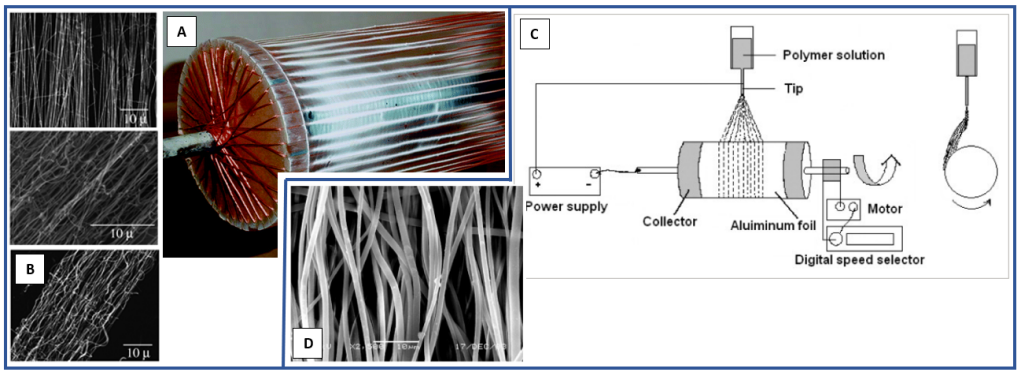

Figure 1.5: Examples of dynamic collector electrode leading to a collection of aligned fibers -wire drum (A,B) [2] or a full drum (C,D) [3]

1.4.2 Specially shaped/designed collector electrode

This method mostly involves a fiber collection between multiple edges [29, 30]. In this case, fiber deposition is varying between multiple surfaces of the collector. This oscillating nature of the fiber is propelled by the residual charge it caries and by

its slow dissipation after the collection. If for instance using collector with two edges, the fiber collects on the first one, but as the electric charge on that edge starts to build up, the fiber is deflected by this charge to the other edge of the collector. This keeps repeating due to continuous charging and discharging of these two surfaces. This repetitive change in fiber deposition surface leads to straight parallel fibers between these individual surfaces of the collector. If woven fibers are required, collector in form of a flowing liquid can be used. The fibers lend on the surface of such flow and are carried and consequently collected on a mesh as a woven thread [31, 32]. Fig. 1.6 contains examples of such techniques leading to collection of aligned fibers via specially shaped collector.

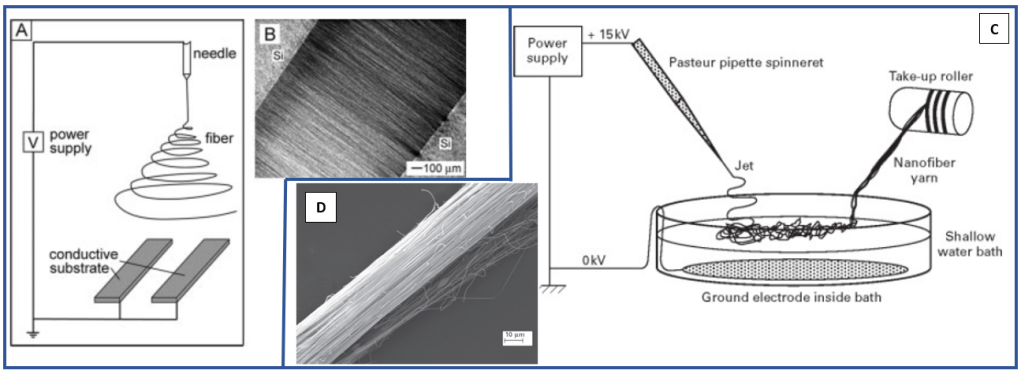

Figure 1.6: Examples of specially shaped collector electrode leading to collection of aligned fibers - deposition over a gap between electrically conductive objects(A,B) [4] or woven yarns, collected from the surface of the electrolyte (C,D) [5]

1.4.3 Electric field fiber steering

This method uses an external electric field created to exert external Coulomb forces on charged particles of the fiber. Multiple articles show how fiber steering in 1D (with a pair of auxiliary electrodes) influences the fiber propagation and collection, and how in connection with spinning drum collector it improves the fiber straightness [33, 34, 35]. This method has been used so far only in combination

with the dynamic collector, where it led to fiber straightness improvement. By itself however, it has not been successfully implemented. The parameters of the steering device are therefore not known, nor are the limitations of such device. Fig. 1.7 shows such application of auxiliary electrodes in 1D fiber steering, in combination with rotating drum, used as a collector electrode.

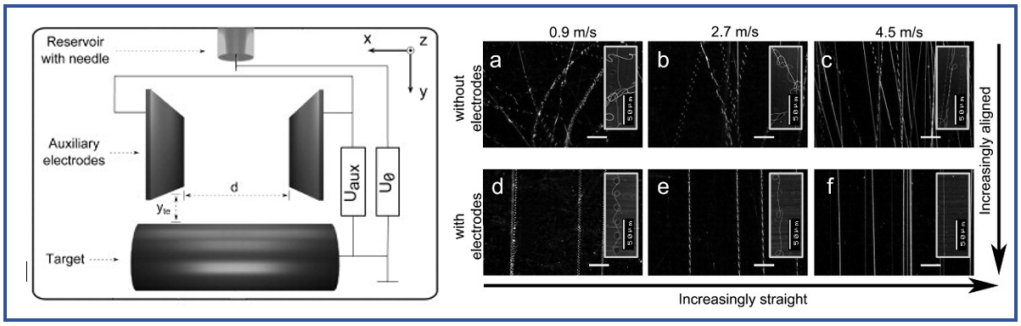

Figure 1.7: Combination of electodynamic fiber steering and application of dynamic collector. [6]

The first two methods are simple and yield very good result in terms of both fiber straightness and alignment. However, it requires a fiber transfer from the collector to the area of interest, what poses a significant risk. The nanometer sized fiber is prone to damage, deformation or introduction of internal tension. To avoid the fiber manipulation, and the complexity of a dynamic collector electrode (that would need to move in multiple axis), we introduce 1D and 2D electrodynamic steering to the electrospinning process, with fiber collection on a flat, static collector electrode. External electrodynamic field created by a set of auxiliary electrodes not only steers the charged fiber into the desired deposition pattern, but also influences the fiber alignment in microscopic scale. Different electric field distributions introduce different Coulomb forces applied on the charged fiber, what consequently leads to different fiber deposition patterns on the collector electrode. Different auxiliary

electrode organizations and positions within the electrospinning device are therefore investigated and described in 4. Proposed applications of developed method require deposition on electrically non-conductive substrate, and performance of such fiber deposition control is demonstrated in chapter 6 on a preparation of tubular scaffolds composed of axially oriented polymer nanofibers.

Mathemtical model of the fiber extrusion with application of electrodynamic steering, which was prepared to simulate the fiber extrusion and collection, is described in chapter 5.

In the following section, electrospinning working parameters and their impact on the extruded fiber are discussed.

Chapter 2

Working Parameters

In this section, electrospinning parameters with the most significant impact on the fiber extrusion and fiber properties are described[36]. These parameters can be divided into three main groups. Device parameters, solution parameters and environment or ambient parameters. On top of these, electrospinning device frequently contains various mechanisms to influence a fiber collection and to straighten this fiber. In this chapter, the main fiber control techniques and mechanisms are described.

2.1 Device Parameters

2.1.1 Nozzle voltage (NV)

After the threshold nozzle voltage is reached and a polymer jet is created, we observed, that the nozzle voltage can be reduced about 10% to 15%, without stopping the fiber from spinning. Generally, lower nozzle voltages lead to finer (lower diameter) fiber which dries faster. Increase in nozzle voltage leads to a more mass being pushed into a jet and so either thicker fiber or creation of multiple fibers are created. Neither of these cases are desirable for both electrostatic and electrodynamic fiber focusing. The thicker fiber might not have enough time to dry on its path to a collector and would deposit wet. This can be seen from Fig. 2.1, where electrospun PEO fiber is extruded with three different nozzle voltages. All the other electrospinning parameters were kept constant. From series of figures corresponding to NV=10 kV, it can be seen the fiber was partially spun as a thick fiber leading to

a wet deposition, and partially as multiple fibers leading to nanometer-sized fibers as with lower nozzle voltages. For electrostatic or electrodynamic focusing, multiple fiber creation is not desirable. These charged fibers are distorting the electric field created inside the device and are influencing the other fibers, as they repel each other. At the same time, we were not able to find any combination of parameters, that would lead to a specific number of created fibers.

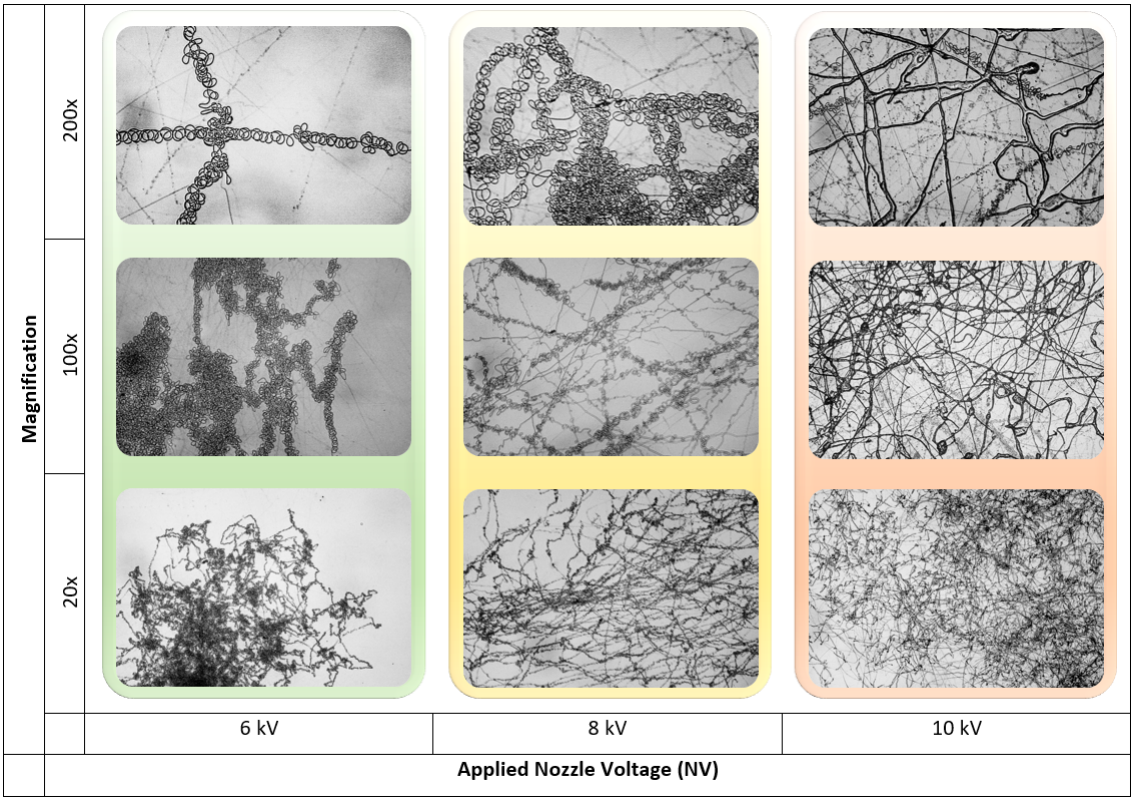

Figure 2.1: Investigation of experimentally obtained PEO nanofibers and its dependancy on applied nozzle voltage(NV). NC distance was kept constant for all the experiments at NC=60 mm

Nozzle voltage is one of the most signifficant factors in terms of achievement of the stable fiber extrusion. Fiber extrusion and parameters of the Taylor cone are

closly related. Stable fiber extrusion requires stable Taylor cone of ideal apex angle. This was found to be 98.6° [37]. On Fig. 2.2, Taylor cone with initial straight segment of the extruded PEO fiber is shown. It can be seen, that with increasing nozzle voltage, Taylor cone starts to loose stability. Based on the flow rate of the electrospun material, either Taylor cone stretches and thick fiber is extruded, or if the flow rate is not sufficient to support this thick fiber, multiple thin fibers are extruded at the same time. Each such fiber then extrudes from its own Taylor cone within the droplet at the tip of the spinneret. these multiple Talor cones are not stable and they form, move and fall apart unpredictably.

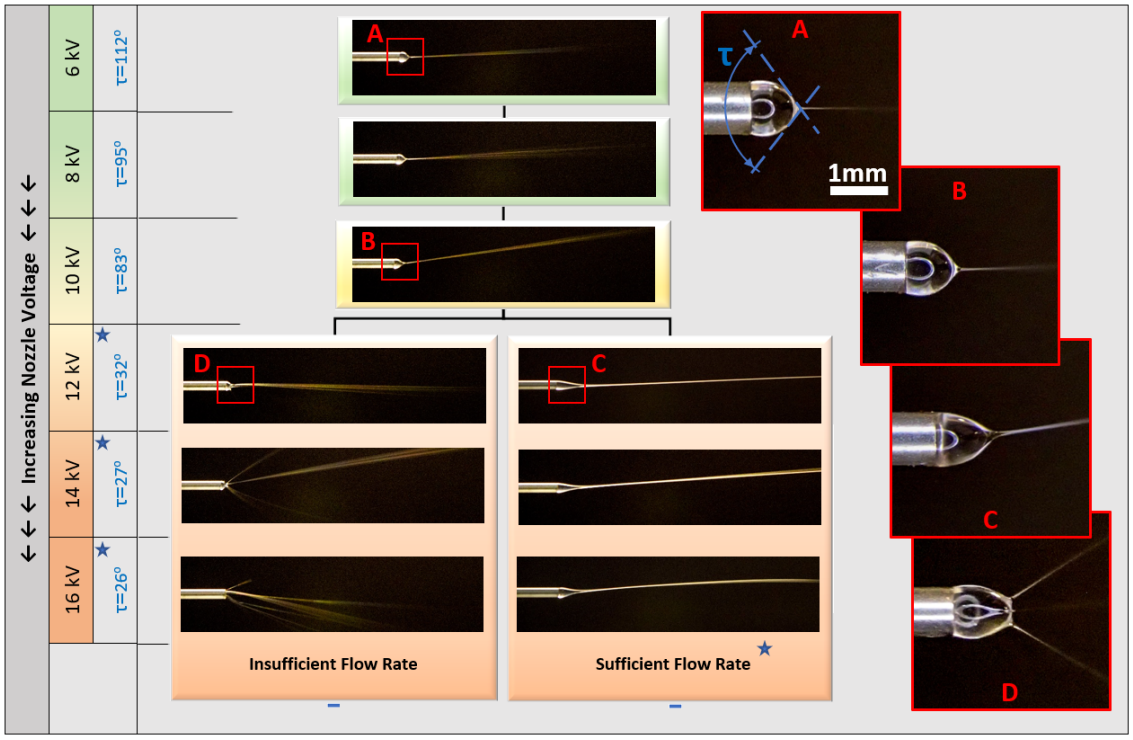

Figure 2.2: Taylor cone shape and stability as a function of nozzle voltage. Taylor cone apex angles marked by asterisk correspond to a Taylorcone with sufficient polymeric flow rate.

Unstable Taylor cone is undesirable as the thick fibers deposit wet (shown in Fig. 2.1), and the multiple fibers extruded at the same time are difficult to control. This is because their behaviour is unpredictable. Their location of extrusion changes with time, their amount changes, therefore their thickness and amount of charge carried by individual fibers changes as well. For these reasons, it is most benefitial to keep the nozzle voltage close to the treshold voltage and so keep stable Taylor cone and stable fiber extrusion. Treshold nozzle voltage, as a minimum voltage at which the electrospinning process can be initiated, is a function of multiple parameters. T.Lin & J.Fang [37] state the relationship between these parameters and treshold nozzle voltage as shown in Eqn. 2.1,

$$V_{TH} = 2\,\frac{H}{L}\sqrt{\ln\left(\frac{2\,L}{R} - \frac{3}{2}\right)\,(0.0117\,\pi\,R\,\gamma)} \tag{2.1}$$

where H is the nozzle-to-collector distance, L is the length of the capillary spinneret, R is the capillary radius, and γ is the solution surface tension. Experimental verification of Eqn. 2.1, however, shown its accuracy is fairly low. This is shown in Fig. 2.3, where 5 wt% PEO solution with surface tension of $\gamma = 0.05[N/m]$ was extruded. Possible reason to this difference between calculated and measured values of the treshold nozzle voltage is that too many electrospinning device parameters were neglected in this equation.

2.1.2 Nozzle to collector electrode distance (NC)

There are tradeoffs in nozzle to collector distance. With increase in this distance, fiber needs to travel longer distance before it deposits on the collector. This results not only in higher stretch of the fiber, but it also give it more time to undergo higher orders of bending instability, resulting in more buckled fiber. Decreasing the nozzle to collector distance is reducing the fiber flight time and so the drying time. If this distance is too short, wet fiber deposition will occur. This can be seen from Fig. 2.4, where the lowest nozzle-to-collector distance in fact led to a thick, wet fiber

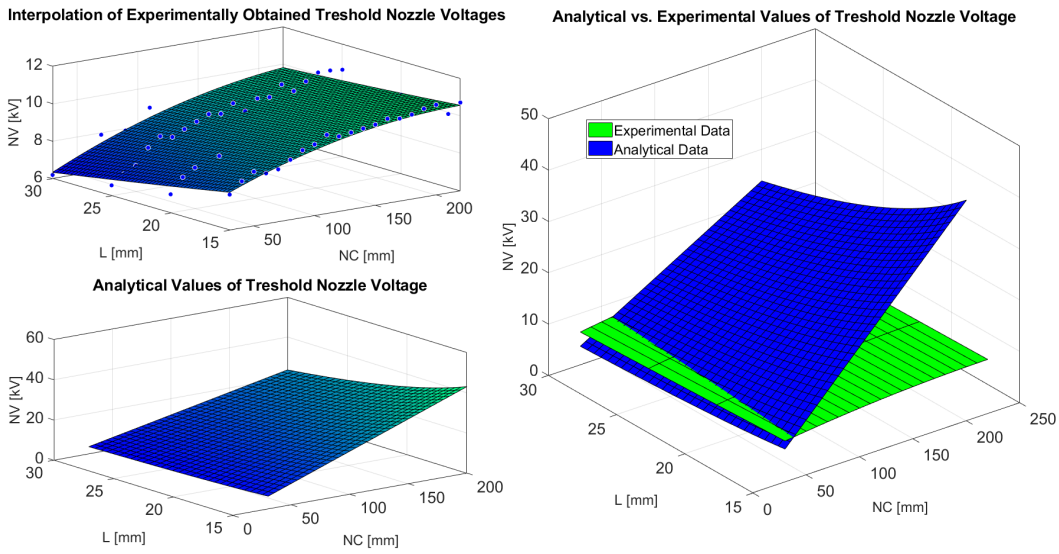

Figure 2.3: Comparison of calculated and experimentaly obtained treshold nozzle voltage for different spinnerets and different nozzle-to-collector distances

collection. It can also be seen, that the wet fibers shown here are straight and not buckled as in Fig. 2.1 for high NV. This is because at short NC distance, fiber did not have enough time to undergo multiple orders of bending instability as it did with longer distance traveled form the nozzle to collector.

2.1.3 Flow rate (FR)

Significance of flow rate of the polymer solution in the needle and its impact on the fiber parameters is not well understood. Some researchers found minimal impact across the tested range [19] and others found significant impact of flow rate on the fiber properties [20]. Our experiments support findings of the later article. The smoothest fiber, and a consistent fiber production were achieved with minimal flow rate, sufficient to provide consistent polymer solution supply to the Taylor cone and to the electrospun fiber. With lower flow rate, electrospinning was stopped and restarted after accumulation of sufficient solution in the needle. With increasing flow

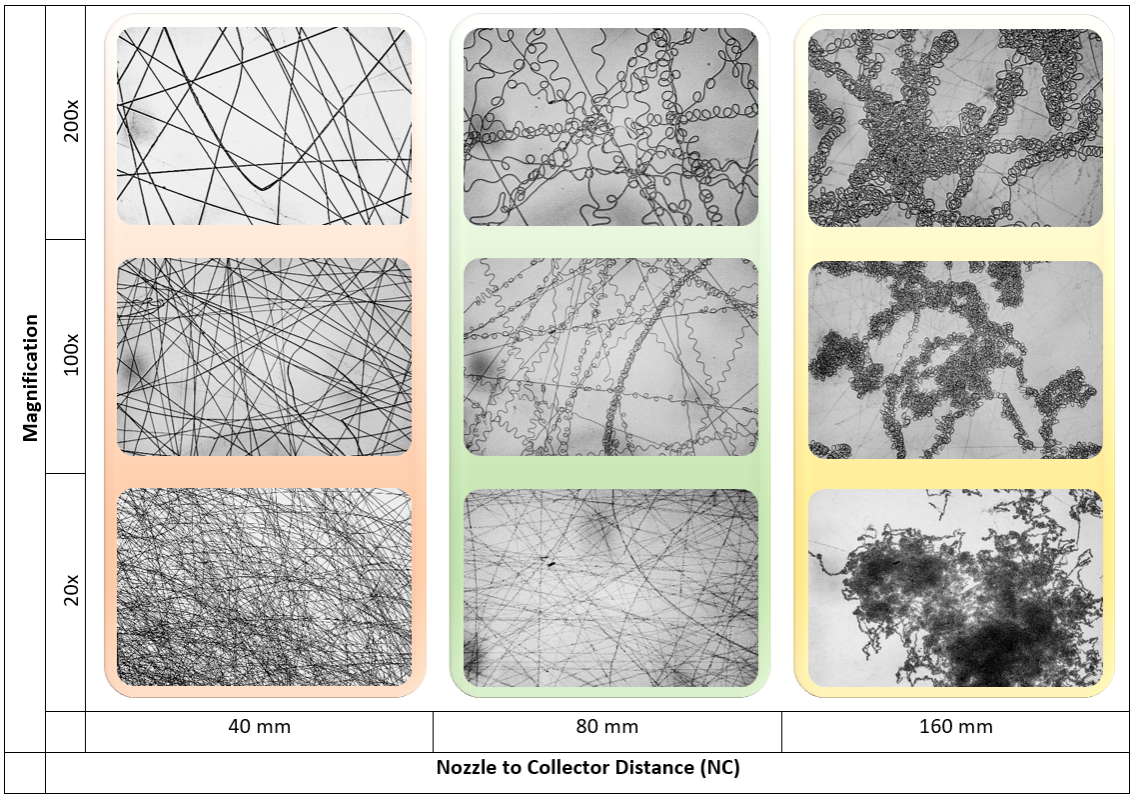

Figure 2.4: Investigation of experimentally obtained PEO nanofibers and its dependancy on Nozzle-to-Collector distance (NC). NV was kept constant for all the experiments at NV=8 kV

rate above the optimal level, fiber thickness was first increased, polymer solution droplet formed at the tip of the nozzle and multiple fibers were often created. This is shown in Fig. 2.5

2.1.4 Needle Diameter(D)

No significant impact of the spinneret diameter on the fiber or electrospinning process was found. With its larger diameters, it is however, more difficult to set the optimal polymer flow rate, as it is not evident if the droplet at its tip is of a constant size. No significant impact of this parameter was confirmed by multiple researchers

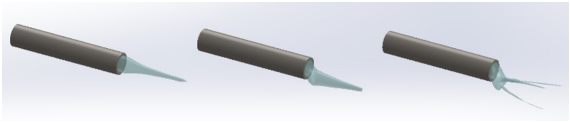

Figure 2.5: Process of creation of the Taylor cone with gradual increase of applied electric potential to a spinnaret containing the polymer solution

[38, 39]

2.1.5 Collector Electrode Resistivity

As the fiber propagates trough the air, some of its charge is dissipated into the environment, but some residual charge is still deposited on the collector. For this reason, the collector must have high electric conductivity, to be able to dissipate the charge quickly and so to prevent this charge from building up on the collector electrode. If the residual charge on the collector builds up, it repels the incoming fiber, and causes the deposition region drift. This drift can not be avoided entirely, and is especially difficult to avoid, if multiple layers of fiber are deposited on top of each other, as the previously deposited polymer layers are non-conductive, and the charge dissipation is therefore much slower.

2.2 Solution Parameters

2.2.1 Solution concentration (CC)

Polymeric concentration [40] is one of the most important parameters, that significantly influences the electrospinning process. In this study three different concentrations of poly ethylene oxide (PEO) in water were investigated. 5%, 7.5%, and 10%. It influences the stretch-ability and material integrity of the fiber trough viscosity resp. surface tension. In general, if the concentration is too low, it leads to electrospraying where non-fibrous elements are collected. At optimal concentration, fiber

after extrusion is evenly stretched by internal Coulomb forces and smooth fiber is obtained. With further increase in concentration, premature drying of the polymeric solution at the tip of the nozzle might occur, and defective (mostly beaded) fiber is collected. From the performed set of experiments, I found that the 5% solution provides the best results.

2.2.2 Electric conductivity

Can be increased by addition of ionic salts, and it influences not only a formation of the Taylor cone, but also the fiber parameters, like its diameter or porosity. As the number of ions (charge carriers) increases in the solution, surface charge density increases, and so do internal and external Coulomb forces. Therefore, fiber gets stretched more in the electrospinning process, and also is expected to become more responsive to electrostatic and electrodynamic steering. At the same time, as the number of charge carriers increases, the conductivity of the polymer solution increases, what negatively influences the Tayler cone formation and if certain threshold is reached, electrospinning would be terminated [41, 42]. From measurements reported in [43], it can be seen, that the surface tension grows very slowly with increase of salt concentration compared to increase in electric conductivity of the solution. My experiments confirm this conclusion, as the diameter of the fiber or its responsiveness to the external electric field did not measurably change, however, the ability to extrude the fiber was significantly impaired and the fiber started to lose integrity at LiBr salt concentration of 0.2 wt%. With LiBr concentrations at 0.5 wt%, mostly electrospraying was observed.

2.2.3 Surface tension and Viscosity

Are parameters dependent on material composition of the polymeric solution and on its concentration. It was proven, that there exists an optimal viscosity range, for which smooth fibers can be extruded. With lower than optimal viscosity, electro-

spinning tends to change to electrospraying, and for higher than optimal viscosities, the fiber extrusion initiation is problematic and beaded fibers are often collected. For the surface tension, it can be adjusted by corresponding solvent selection. It was shown, that it influences the morphology of the fiber and that if the beaded fiber is extruded, reduction of the surface tension can smoothen such fiber [44] and [45] report, that the smoothest fiber can be achieved with high ratio of viscosity to surface tensions.

2.3 Environment parameters

Ambient parameters can also influence the parameters of the fiber. As the solution‘s viscosity is inversely dependable on the temperature, higher environment temperatures lead to lower fiber diameter as shown by [46, 47]. Humidity influences the evaporation rate and electric discharge into an environment. As the charge is neutralized faster at higher humidity of the environment, the internal Coulomb forces on the fiber are decreased, and so is the stretch of the fiber. This thicker fiber dries slower not only because of the lower surface area to volume ratio, but also the solvent evaporation is impaired by the high ambient humidity. Result of this could consequently be a collection of wet fibers. All experiments described in this work were performed in the lab conditions, in the vented enclosure.

As described in the introduction, the fiber collected on a flat electrode is due to the mechanical buckling and the electric charge driven bending instability it undergoes highly buckled, and with no alignment, as shown in Fig. 2.1 and 2.4. No combination of parameters previously discussed in this section would lead to a straight and aligned fibers. To influence the fiber deposition alignment, additional fiber collection device or specific collection method must be implemented. This is discussed in the following section.

Chapter 3

Electrostatic Focusing

3.1 Electrostatic Focusing

External Coulomb forces applied on the fiber from electrostatic field created inside of electrospinning device are not capable of straightening the electrospun nanofibers. This is known from the Earnshaw‘s theorem, stating that the charged particles cannot be kept in a stable equilibrium solely by electrostatic forces. The electrostatic field is rather applied to the electrospinning device to investigate its ability to constrain the fiber movement in some extent. Also, as an initial step to the electrodynamic steering, impact of this electrostatic focusing on the fiber extrusion itself was investigated. Generation of the external electrostatic field and so application of external Coulomb forces on the charged fiber should be able to constraint the fiber movement envelope and so consequently also the fiber deposition region. The simplest way to create this electrostatic field is by an introduction of auxiliary electrodes placed within the electrospinning device. The most effective application region is in between the nozzle and a collector electrode. Initially, a pair of flat auxiliary electrodes symmetrically placed along the axis of the device was considered. In this configuration, the fiber after extrusion needs to pass trough the region between these auxiliary electrodes to reach the collector electrode. This configuration of the electrospinning device can be seen in Fig. 3.1 and in schematic view on Fig. 3.2

As the fiber and auxiliary electrodes have the same charge polarity, the fiber is repelled away from the surface of these electrodes. This results in confinement of the fiber movement and therefore also the fiber deposition area on the collector. Different electric field configurations inside the device were achieved by varying the

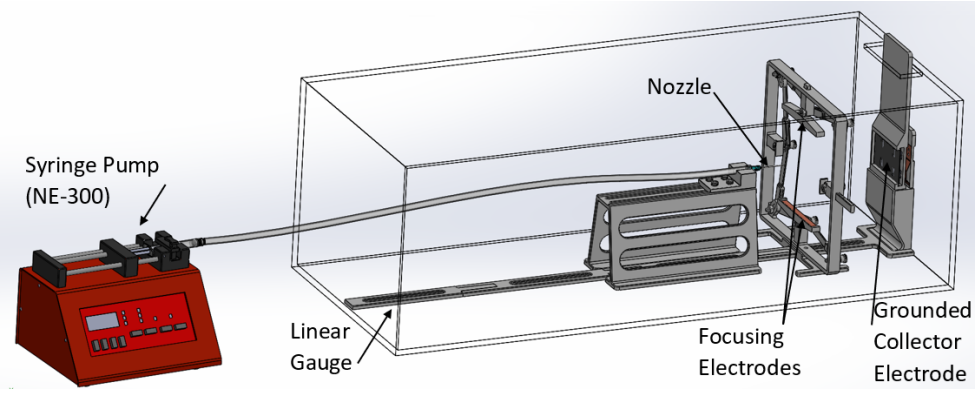

Figure 3.1: Model of used electrospinning device with a pair of auxiliary electrodes used for electrostatic focusing.

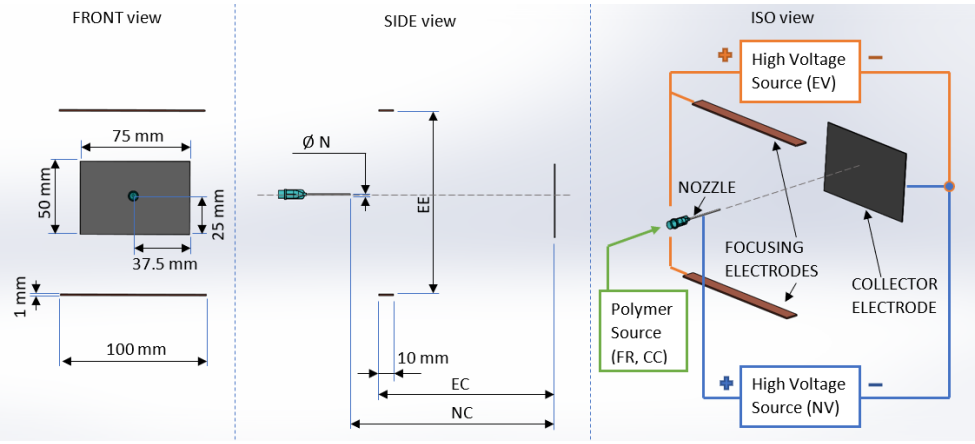

Figure 3.2: Schematic view of the Electrospinning device with elestrostatic focusing. Individual components and device parameters are shown and named

position of focusing electrodes along the device axis (EC), their separation (EE) and applied voltage onto these electrodes (EV). Different electric field inside of the electrospinning device introduces different external Coulomb forces applied to the fiber, what leads to different fiber deposition pattern on the grounded collector electrode.

The auxiliary electrodes were designed to have dimensions of 10x100x1 mm and

were kept constant for all the experiments. Impact of the rest of the auxiliary electrodes parameters on the electrospinning device and on the extruded fiber is described in the following subsection.

3.2 Stable extrusion regimes

From the electrospinning parameters and electrostatic focusing parameters, nozzle to collector distance (NC), confining electrode voltage (EV), electrode to collector distance (EC) and nozzle voltage (NV) were found to be the most influential in terms of stability of the fiber extrusion. Stable extrusion was defined as a continuous production of a single nanofiber, that is deposited dry. Varying these most influential parameters, different fiber extrusion regimes were found. These three regimes, for three different nozzle-to-collector distances, are shown in Fig. 3.3, where the stable extrusion regime is marked in yellow. The bottom surface of this region shows the threshold nozzle voltage for given combination of electrospinning parameters. There is no fiber extrusion below this surface. The upper boundary surface shows at what nozzle voltage the device starts spinning multiple fibers or thicker fibers that deposit wet. Above this surface, device operates in the unstable fiber extrusion regime. It can be seen, that for the lowest nozzle to collector distance of NC=50 mm, the stable fiber extrusion regime is very limited. Reducing this distance even further would result in always wet or multiple wet fibers collection. After securing the steady nanofiber extrusion, electrostatic focusing parameters can be discussed. This is done in the following subsection.

3.3 Electrostatic Focusing Analysis

As previously stated, different electric field distributions inside of the electrospinning device lead to different fiber deposition patterns on the grounded collector electrode.

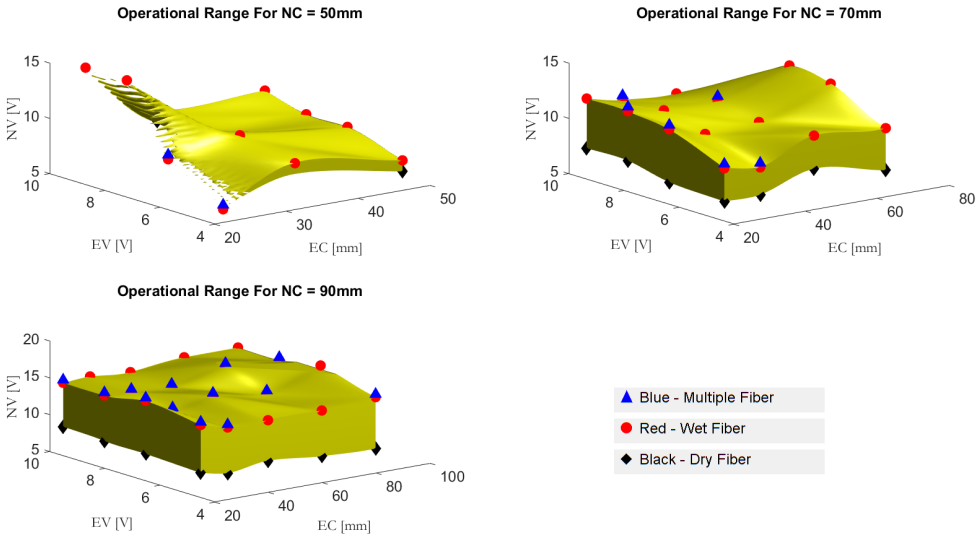

Figure 3.3: Schematic view of the Electrospinning device with elestrostatic focusing. Individual components and device parameters are shown and named

In terms of fiber focusing, obtained experimental data suggest, that the focusing effect of focusing electrodes is highest, when these electrodes are placed approximately in the middle of the distance from the nozzle to the collector electrode (NC). Separation (EE) and electric potential (EV) applied to the focusing electrodes are two parameters which need to be set together, to form a desired electric field inside the device. Increase in separation of focusing electrodes is effectively equal to lowering the electric potential on these electrodes. FEA analysis of a device with a pair of focusing electrodes was performed, and results of this numerical analysis are shown in Fig. 3.4, where external electric field components along axes of the device are plotted.

Fig. 3.4 shows that the $x-$ component of the electric field is non-zero, even without deflection electrodes operating along this axis. This is an effect of the low width of the focusing electrodes ($z-$ direction dimension) and a close presence of the nozzle (at high potential), and grounded collector. As an effect of this, the device becomes confining in both $-$ and $y-$ directions, where y direction external

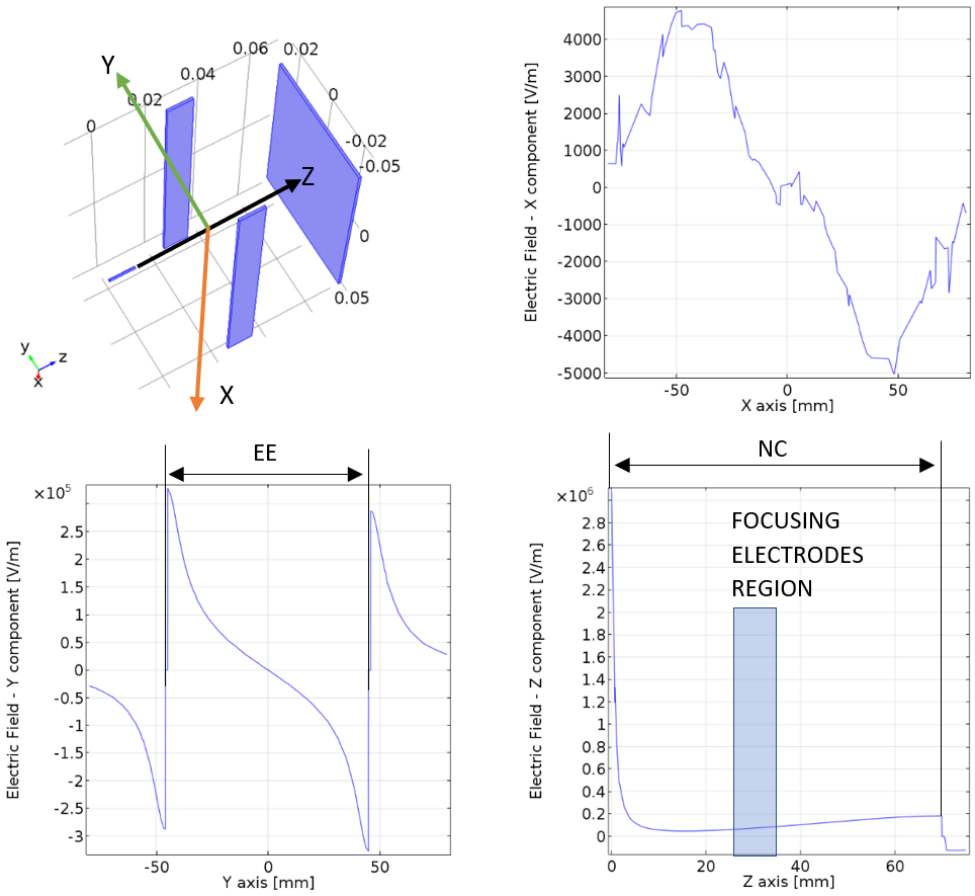

Figure 3.4: FEA analysis of the electric field distribution in electrospinning device. Top-Left: electrospinning device layout; Top-Right: Electric field $x-$ component along the x axis between the focusing electrodes; Bottom-Left: Electric field $y-$ component along y axis, between the focusing electrodes; Bottom-Right: Electric field $z-$ component along the z axis of the design (from the nozzle to the collector electrode). Top-Right figure shows, that the electric field $x-$ component is non-zero along the $x-$ axis, even though there are no focusing electrodes on this axis.

Coulomb forces are still about two orders of magnitude higher than those in $x-$ direction. Fig. 3.4 also shows, that the $y-$ direction electric field is no longer linear as expected(Eqn. 5.3). However, considering only the region close to the device axis ($z-$axis), where the fiber moves, it stays very close to linear. The steering effect of

the electric fields was investigated further in order to establish optimal conditions.

Fig. 3.5 shows three different electrospinning setups with electrostatic focusing are investigated in terms of focusing electric forces. Based solely on the electric field component in direction to the center plane of the device ($y-$axis), setup with lowest separation of these electrodes and highest applied electric potential (green/asterisk marked setup) would be chosen. This decision would be given by the fact that the highest electric field in this direction leads to the highest coulomb forces applied on the fiber by a set of focusing electrodes. However, limitations to the separation and potential on focusing electrodes exist. Firstly, limitation on the electric potential on focusing electrodes is introduced by the air breakdown voltage. As the space inside the device is in some setups limited, it becomes difficult to keep safe distances between components of the device to prevent electric breakdown and potential damage on the apparatus. The air breakdown potential is even increased by increased humidity accumulated inside of the device from drying fiber. Secondly, and more importantly, if the electric potential along the axis of the device is plotted, for the case shown in green/asterisk in Fig. 3.5, it has a non-decreasing or even increasing character on some region along this axis. This leads to elimination of the electric field in $z-$ direction or even making it negative, what means that there is no or negative electric force along the axis of the device and so the fiber is not attracted to the collector electrode any longer, forcing it to collect on the walls of the device.

Set of figures from FEA analysis in Fig. 3.6 show, how the electric potential distribution in horizontal plane and electric field lines (originating at the tip of the nozzle) change with increasing electric field in lateral direction and decreasing in axial direction. Electric field lines are just a visualization of a vector field (Electric Field), and they represent a direction in which electric forces are acting on a charged particle in the particular location of this electric field. Even though they do not represent the exact trajectory of the fiber, as the initial acceleration of the fiber is not assumed nor the repulsion forces between the particles of the fiber or the mechanical

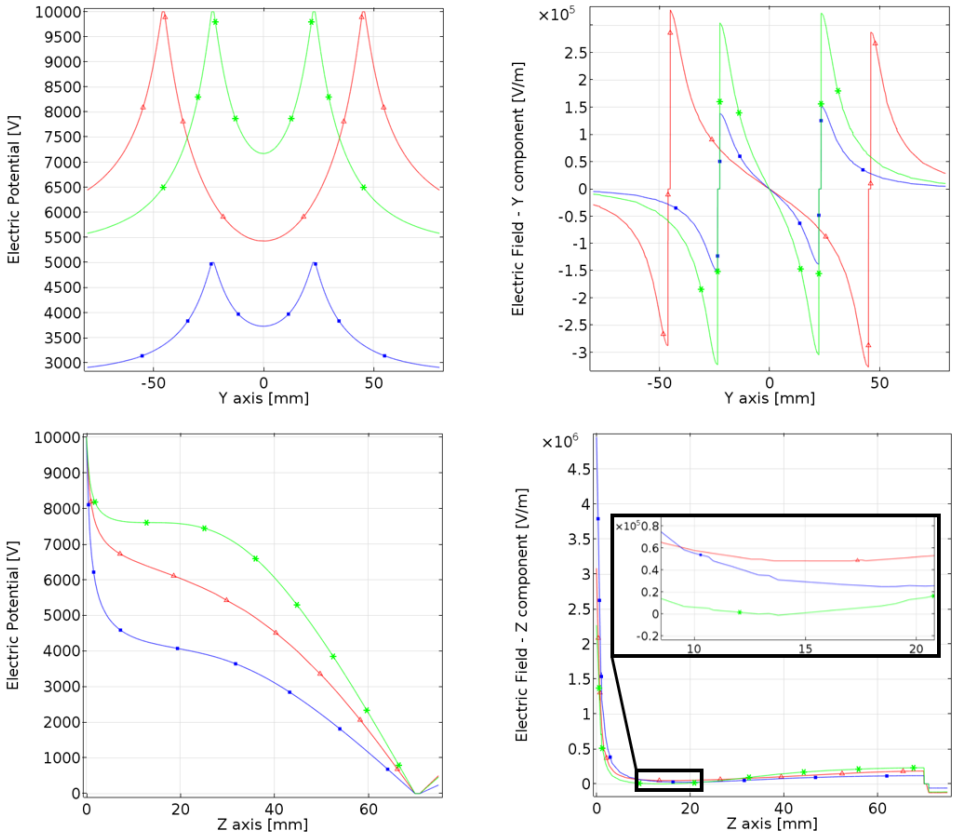

Figure 3.5: FEA analysis of the electric potential and electric field distribution in the electrospinning device for three different setups of focusing electrodes. Fixed parameters: $NV = 10\,kV, NC = 70\,mm, NE = 30\,mm$; variable parameters: $EE = 90\,mm, EV = 10\,kV$ (red traces); $EE = 50\,mm, EV = 5\,kV$ (blue traces); $EE = 50\,mm, EV = 10\,kV$. (green traces)

forces, they give an insight on how the electrospinning device is influencing the fiber movement. Based on the field lines, four different electric field distribution regimes can be identified. These regimes labeled (A-D) are shown in Fig. 3.6 The location of the two confining electrodes, shown in blue and red in Fig. 3.5, both lead to field distribution regime (B). Setup shown in green leads to distribution regime (D), as it doesn't allow fiber to pass between the focusing electrodes and form a deposit on a collector.

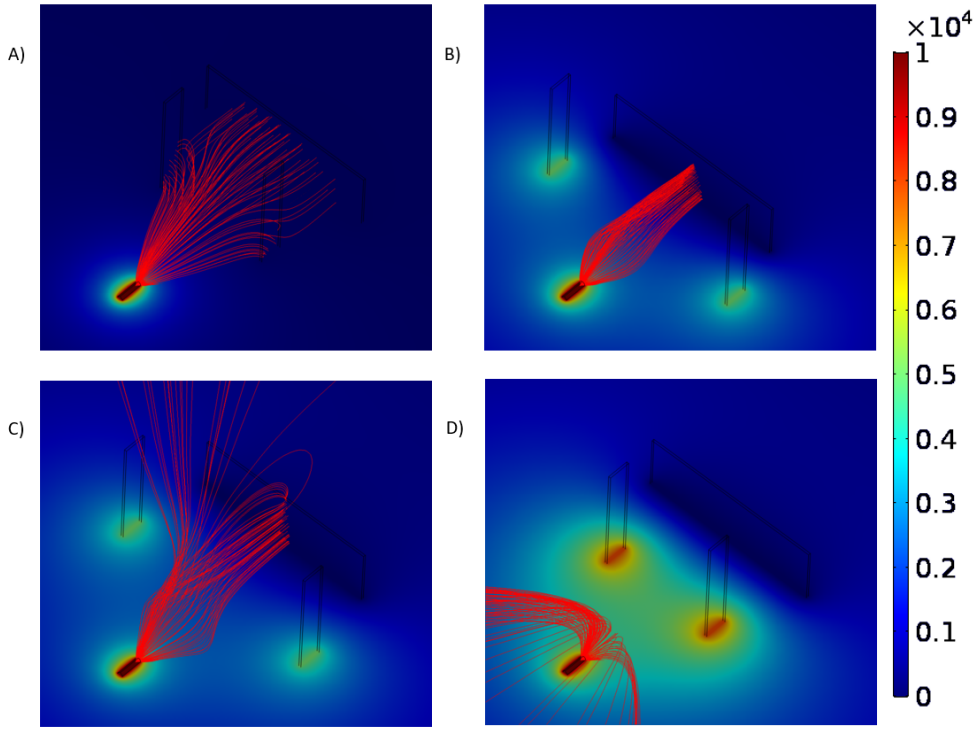

Figure 3.6: FEA analysis of the electrospinning device with a pair of focusing electrodes. Electric potential distribution in horizontal plane and electric field lines originating at the tip of the nozzle are shown. Based on distribution of the electric field lines, four different electric field distribution regimes can be recognized: A-Attracting regime (fiber is at least partially collected on focusing electrodes); B-Focusing regime; C-Focusing and reverting regime (Some part of the fiber is collected outside of the collector electrode); D-Reverting regime (No fiber collection on collector, nor focusing electrodes)

Existence of all four of these regimes was experimentally verified and the results are described in the following section.

3.4 Experimental Results

Among the four electric field distribution regimes, regimes B and C are the most important ones, and so this section will focus on these two. Except of these two

electric field distribution regimes (Fig. 3.6), this section refers also to the fiber extrusion regimes shown in Fig. 3.3. Performed series of 120 experiments showed, that when the fiber extrusion was stable, and it was operated under field distribution regime B, it always collected in an almost circular deposition area within 1 cm in diameter (Fig. 3.7-Left). The size of this deposition region can be decreased by increase of focusing effect of electrodes increasing applied electric potential or decreasing the electrode separation, while remaining within the field distribution regime B. After reaching the field distribution regime C, the fiber is forced to a larger area of attraction and the deposition region increases in size and stretches in direction parallel to the focusing electrodes (Fig. 3.7-right).

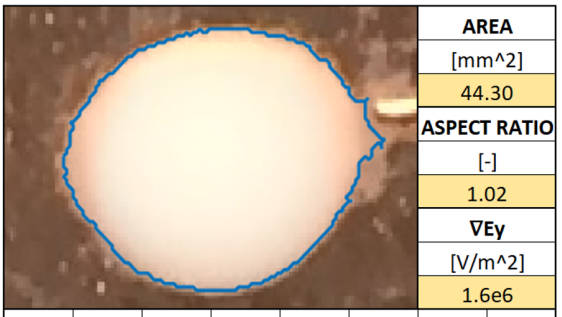

AREA
[mm^2]
44.30
ASPECT RATIO
[-]
1.02
∇Ey
[V/m^2]
1.6e6

NC	NE	EE	NV	EV	FR	CC	N
[mm]	[mm]	[mm]	[kV]	[kV]	[ml/hr]	[w%]	[gage]
85	10	95	10	5	0.06	7.5	20

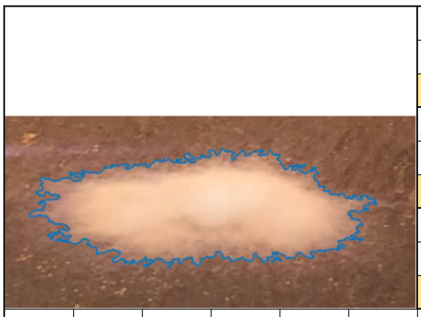

AREA
[mm^2]
136.52
ASPECT RATIO
[-]
3.11
∇Ey
[V/m^2]
4.0e6

NC	NE	EE	NV	EV	FR	CC	N
[mm]	[mm]	[mm]	[kV]	[kV]	[ml/hr]	[w%]	[gage]
85	50	70	10	7.5	0.06	7.5	20

Figure 3.7: PEO nanofiber deposit and its evaluation in MATLAB, with electrospinning parameters listed on the bottom of the figure. To the right from the experimental results are: area of fiber deposit, aspect ratio of the deposit(width/ height), and $\nabla E_y = \beta U_{DC}$ is a gradient of $y-$ component of the electric field along y axis between the focusing electrodes. Left: Stable fiber extrusion under electric field distribution regime B; Right: Stable fiber extrusion under electric field distribution regime B

If the electrospinning device is operated in an unstable fiber extrusion regime and it produces multiple fibers or disappearing/reappearing fibers, their behavior is also influenced by the electrostatic focusing. Multiple fibers can be collected as a

series of almost circular deposits for field distribution regime B, or a series of larger, non-circular, blown-up deposition regions for the field distribution regime C. These are shown in Fig. 3.8

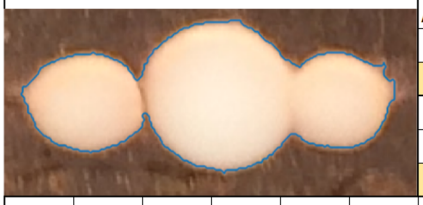

AREA
[mm^2]
58.76
ASPECT RATIO
[-]
2.56
∇Ey
[V/m^2]
1.6e6

NC	NE	EE	NV	EV	FR	CC	N
[mm]	[mm]	[mm]	[kV]	[kV]	[ml/hr]	[w%]	[gage]
85	30	95	10	7.5	0.06	7.5	20

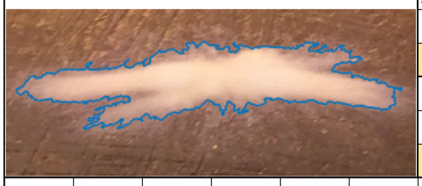

AREA
[mm^2]
121.70
ASPECT RATIO
[-]
4.47
∇Ey
[V/m^2]
2.2e6

NC	NE	EE	NV	EV	FR	CC	N
[mm]	[mm]	[mm]	[kV]	[kV]	[ml/hr]	[w%]	[gage]
85	30	95	10	10	0.04	7.5	18

Figure 3.8: PEO nanofiber deposit and its evaluation in MATLAB, with electrospinning parameters listed on the bottom of the figure. To the right from the experimental results are : area of fiber deposit, aspect ratio of the deposit(width/ height), and $\nabla E_y = \beta U_{DC}$ is a gradient of $y-$ component of the electric field along y axis between the focusing electrodes. Left: Unstable fiber extrusion (multiple fibers) under electric field distribution regime B; Right: Unstable fiber extrusion (multiple fibers) under electric field distribution regime B

After a fiber is created in the electrospinning device, it initially oscillates with higher amplitudes until it stabilizes. Therefore, disappearing and reappearing fiber from unstable extrusion regime oscillates much more than stably produced fiber. As this oscillatory motion of the fiber is compressed from sides by the electrostatic field created by focusing electrodes, the fiber deposits in an elliptical region if operated under field distribution regime B (Fig. 3.9-Left), or even more compressed line-like deposition region for stronger focusing electrostatic field in field distribution regime C (Fig. 3.9-Right)

On the bottom of the series of figures Fig. 3.7 - 3.9, fiber deposit parameters (deposition area and aspect ratio) are shown together with the gradient of $y-$ com-

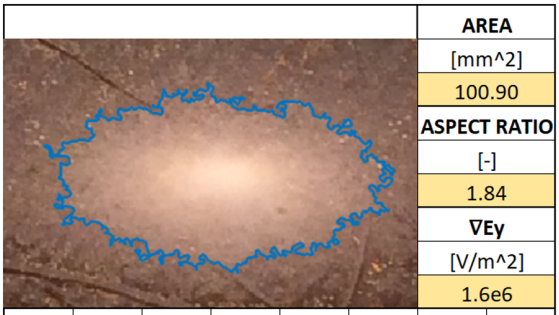

AREA	
[mm^2]	
100.90	
ASPECT RATIO	
[-]	
1.84	
∇Ey	
[V/m^2]	
1.6e6	

NC	NE	EE	NV	EV	FR	CC	N
[mm]	[mm]	[mm]	[kV]	[kV]	[ml/hr]	[w%]	[gage]
85	30	95	10	7.5	0.08	10	20

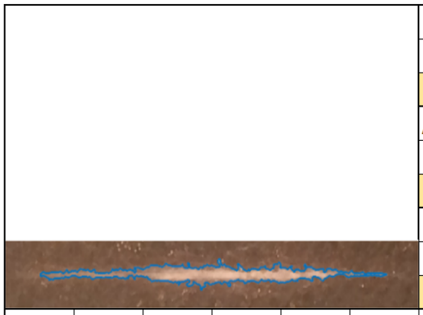

AREA	
[mm^2]	
30.72	
ASPECT RATIO	
[-]	
12.61	
∇Ey	
[V/m^2]	
2.3e6	

NC	NE	EE	NV	EV	FR	CC	N
[mm]	[mm]	[mm]	[kV]	[kV]	[ml/hr]	[w%]	[gage]
105	50	95	10	10	0.06	7.5	20

Figure 3.9: PEO nanofiber deposit and its evaluation in MATLAB, with electrospinning parameters listed on the bottom of the figure. To the right from the experimental results are: area of fiber deposit, aspect ratio of the deposit (width/ height), and $\nabla E_y = \beta U_{DC}$ is a gradient of $y-$ component of the electric field along y axis between the focusing electrodes. Left: Unstable fiber extrusion (single fiber) under electric field distribution regime B; Right: Unstable fiber extrusion (single fiber) under electric field distribution regime B.

ponent of the electric field along $y-$ axis in between the focusing electrodes. The electric field gradient is obtained from FEA analysis of the electrospinning device with given set of parameters. As shown in Fig.3.4, the electric field is linear in proximity to the axis of the device. This gradient of the $y-$ component electric field (βU_{DC} in Eqn. 5.11) shows, that if kept at about $\beta U_{DC} \approx 1.6e6\, V/m^2$, it results in field distribution regime B. If increased to about $\beta U_{DC} = 2.2e6 - 4e6\, V/m^2$, it changes the distribution to regime C, and partial loss of the fiber occurs. In all experiments with electrostatic focusing, fiber deposition only in macroscopic scale was influenced. Even for runs with highest focusing potential, the fiber propagates in chaotic movement and deposits buckled. To achieve a periodic/quasi-periodic fiber movement or to straighten the fibers, electrodynamic focusing must be used.

Chapter 4

Electrodynamic Steering

4.1 1D Steering

Initially, 1D electrodynamic steering was investigated, where only one pair of auxiliary electrodes were used. These electrodes were symmetrically placed with respect to the axis of the electrospinning device as shown in Fig. 4.1. Such placement of auxiliary electrodes, with applied electric potential described by Eqn. 4.1-4.2, apply external coulomb forces on the fiber in lateral, horizontal direction. These force the fiber to oscillate in horizontal plane, as it travels to the collector electrode, where it deposits in horizontal, line-like pattern. With frequencies ranging from 40 to 220 Hz, different lengths of the deposited line were achieved. With increasing frequency of applied forcing function, the fiber has less time to travel laterally before the electric forces change their orientation, and so it deposits in shorter line. This dependency of fiber deposit length on frequency of the forcing function is shown in Fig. 4.2, together with simulation results, which will be discussed later in the section 5 of this work.

$$U_1 = \frac{U_{Ampl}}{2}\left[(\mathrm{sgn}\left(\cos\left(\omega\, t\right)\right) + 1\right] + 660\, V \tag{4.1}$$

$$U_2 = \frac{U_{Ampl}}{2}\left[(\mathrm{sgn}\left(\cos\left(\omega\, t + \pi\right) + 1\right)\right] + 660\, V \tag{4.2}$$

Fig. 4.3 shows the PEO nanofiber deposit on the collector electrode. Lower density fiber deposition below the main deposition region is the transient effect occurring while uncovering and covering the collector electrode at the beginning and at the end of the experiment. Investigation of the fiber at the microscopical scale

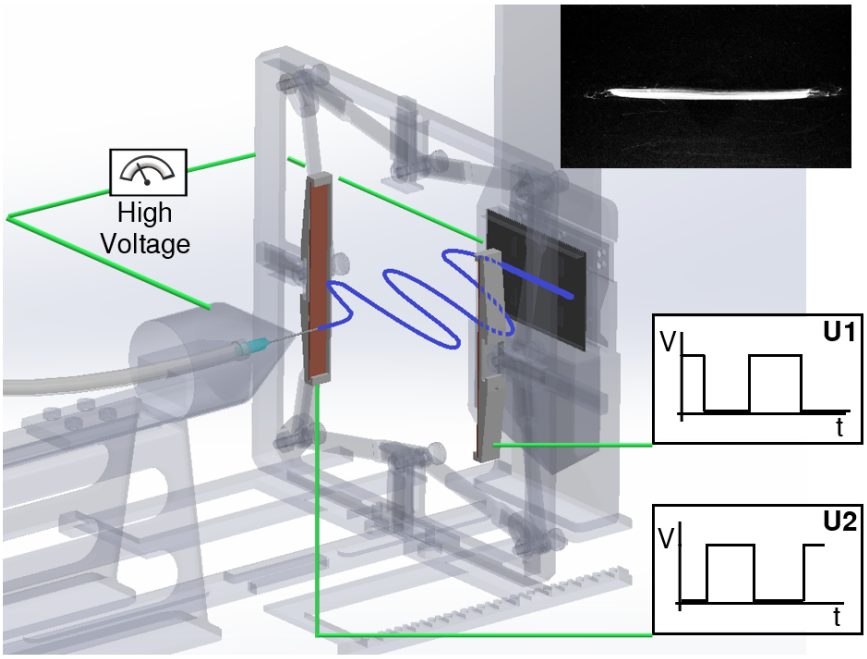

Figure 4.1: Model of used electrospinning device with auxiliary electrodes used for 1D electrodynamic steering, with visualization of electrospun fiber and its deposition pattern on the collector plate. In upper right corner, actual fiber deposit obtained experimentally with 1D electrodynaic steering is shown

reveals that the fibers are well aligned, but not straight. Fibers in the central region of the deposit are straighter, as the lateral velocity of the fiber is at maximum in that region. As the external forces change direction, the lateral velocity of the fiber diminishes and eventually vanishes, as the fiber turns at the end of the deposit. Therefore, the fiber is buckled much more in these regions. To increase this lateral component of the fiber velocity, the external electric forces would need to increase. To do so, separation of auxiliary electrodes would need to be smaller, to increase the electric field they generate, or the amplitude of the forcing function applied to them would need to be higher. With the current hardware, we are limited to amplitude of 10kV and so the separation of the auxiliary electrodes was reduced. To avoid collection of fiber on the surface of auxiliary electrodes, frequency of the

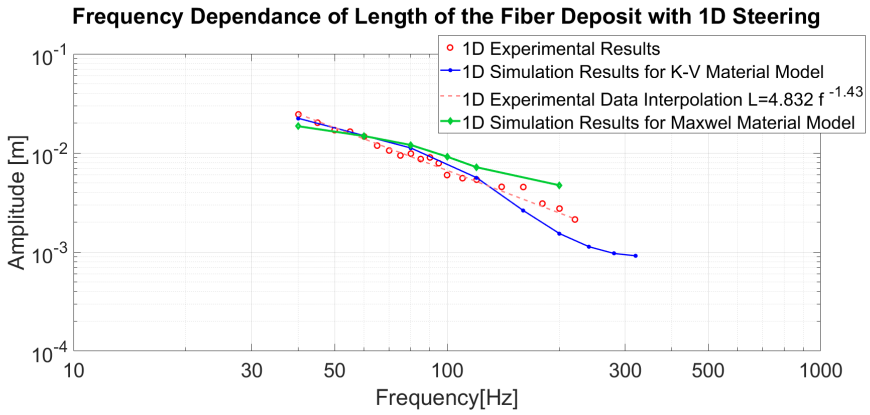

Figure 4.2: Dependence of the length of the fiber deposit on frequency of the forcing function. Electrospinning parameters: Nozzle to collector distance NC=70 mm, Nozzle to auxiliary electrode NE=25 mm, Electrode separation EE=80 mm, Nozzle voltage NV=7 kV, Flow rate FR=0.06 ml/hr.

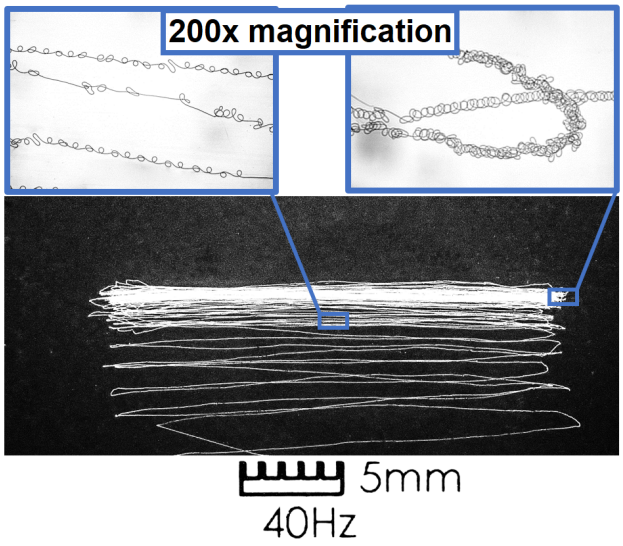

Figure 4.3: Macroscopic and microscopic alignment of the electrospun PEO nanofiber with 1D steering at 40 Hz.

forcing function was increased. This organization increased the external Coulomb forces applied to the charged fiber, and so increased the lateral acceleration of the fiber. At the same time, however, it reduced the time (half the period of the forcing

function) for which the fiber travels laterally in one direction. Even with higher acceleration, it never reached sufficient velocity to straighten the fiber.
Decreasing trend of the fiber velocity with increasing frequency of the forcing function is shown in Fig. 4.4. As the axial component of the electric field is not changed, fiber velocity in axial direction is not expected to change neither. Decrease in fiber velocity is then attributed to decrease in fiber velocity in transverse direction. Fiber velocity was calculated from the total fiber length deposited per half period of the forcing function. Precision of the measurement was significantly influenced by fiber loops counting, ranging from 4 100 loops at 20Hz to just 200 loops at 300Hz. In later described simulations, only one velocity value was used. Frequency of 140Hz was selected, leading to a fiber deposit with 520 loops per 4.3mm long deposit, and corresponding fiber deposition rate (fiber velocity) of 4.8m/s. The total length of the fiber deposited in this case (140Hz), was estimated to be about 4 times more than the length of the deposit. Frequency of 140Hz was not selected only because it lies in the center of the tested frequency range, but also because the fiber length measurement at this frequency is expected to be the most accurate. This is because at low frequencies, the fiber deposit is simply too long and consists of too many loops, what increases the error. At high frequencies, the deposit is short, with only few hundreds of loops, but they are much denser in concentration, what again increases the counting error.

To allow for more fiber movement, and to eliminate the sharp turns at the end of the deposited line-like pattern, additional auxiliary electrodes were introduced. This new steering device is described in the following sub-section.

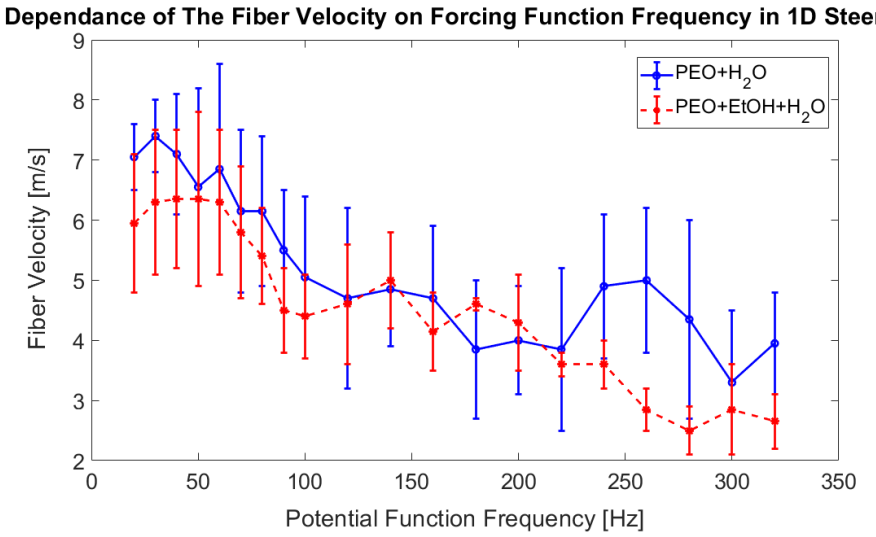

Figure 4.4: Experimental results of an indirect measurement of fiber velocity dependency on frequency of the forcing function in 1D steering. Fiber velocity was calculated from length of the fiber deposited over a half period of the forcing function.

4.2 2D Steering

If set-up properly, addition of another dimension in which the fiber is forced to move would increases the total distance traveled by the fiber in one period of the forcing function. This would lead to a collection of less buckled fiber. The 2D steering device can be set-up in various ways. First, the application of adjusted linear quadrupole trap was investigated.

4.2.1 Paul‘s linear qudrupole trap

Paul‘s quatdupole trap [48] is a type of the ion trap, that uses combination of electrostatic and electrodynamic fields to trap charged particles. It consists of two hyperbolic end-cups with their foci facing each other and another hyperbolic ring electrode placed symmetrically between these end-cups. DC voltage is then applied to the end-cups, and AC radio frequency voltage is applied to the ring electrode.

AC voltage is offset by DC voltage, so the mean potential on the ring electrode is equal to the potential applied to end-cups. Because of this, when the end-caps are at higher electric potential than the ring electrode, the positively charged particle inside the trap is pushed axially to the center of the trap and pulled radially off the axis of the trap. The axial force in this configuration is confining and the radial force is anti-confining. When the phase of the AC voltage changes, and ring electrode is at higher potential than the end-cups, the electric forces change their orientation. Confining forces become anti-confining and vice versa. These constantly changing confining and anti-confining directions inside the device trap the ion in a complex three-dimensional movement.

The Linear quadrupole trap works similarly, but instead of trapping the particles inside the trap in all directions, it allows for axial movement of the particles. Therefore the particles of certain mass-to-charge ratio are able to exit the trap in axial direction. External Coulomb forces exerted on these ions from the electric field created by electrodes of a trap are keeping them on a stable trajectory inside the trap, and preventing them from either exiting the trap in lateral direction or from colliding with these electrodes. Ions with different mass-to-charge ratios will have unstable trajectory inside the device and will eventually collide with the electrodes. Adjusting the amplitude and frequency of the electric potential function applied to the electrodes of the linear quadrupole trap, ions with different mass-to-charge ratios can be filtered. For this reason, this type of an ion trap is used in mass analyzers in mass spectrometry[49].

In Fig. 4.5, the cross-section of the Paul‘s linear quadrupole trap with U_{DC} applied to one pair of electrodes, and $U_{AC} = U_{amp} \cos(\omega t)$ on top of U_{DC} applied to the other electrode pair is shown. It depicts two different time instances within a half period of the AC cycle. LEFT: $t = 0$ and RIGHT: $t = \pi/\omega$. The upper two figures show the electric potential distribution together with the electric field vectors (with logarithmic length) inside the trap. The electric field vector has the

same orientation as the resulting external coulomb force exerted by this field on a charged particle, resp. charged electrospun fiber. The bottom two schematics show the corresponding confining (red) and anti-confining (blue) directions, together with the expected confinement region inside the trap.

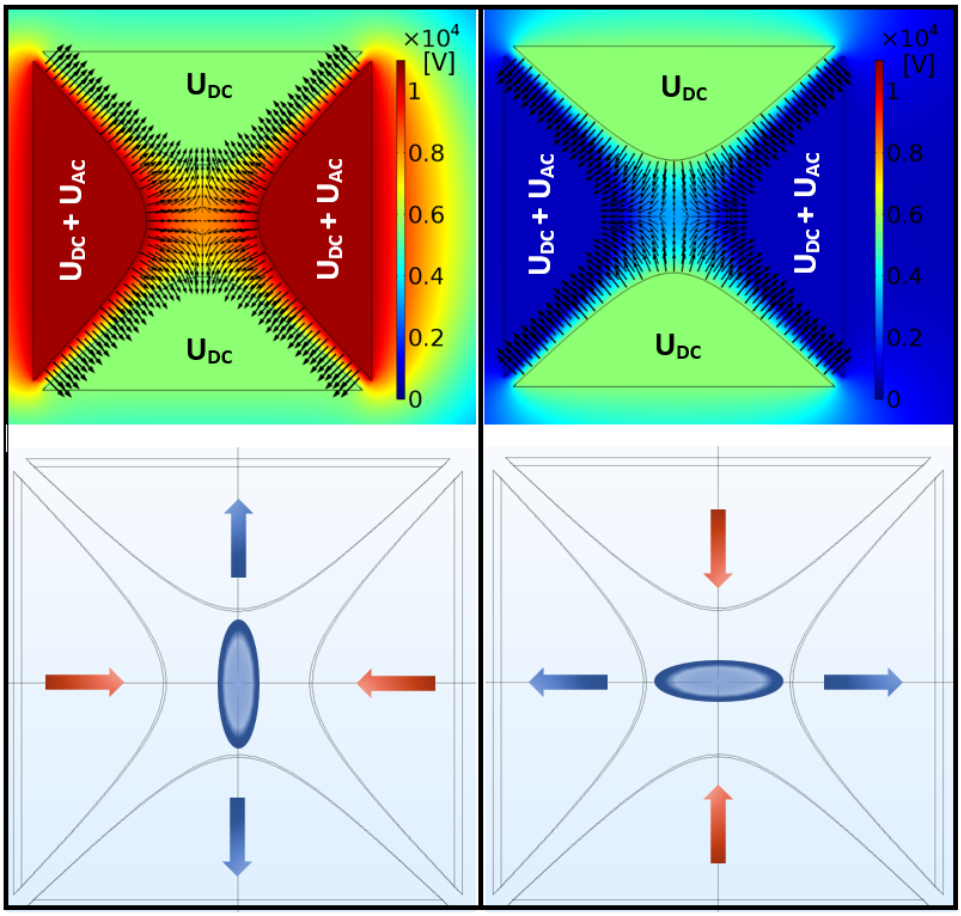

Figure 4.5: Cross-section over the Paul's linear quadrupole trap at two extreme time instances within a half period of the AC cycle. LEFT: $t = 0$ and RIGHT: $t = \pi/\omega$. The upper two figures show the electric potential distribution together with the electric field vectors (with logarithmic length) inside the trap. The bottom two schematics show the corresponding confining (red) and anti-confining (blue) direction, together with the expected confinement region inside the trap.

It was assumed, that the charged fiber inside the trap, under proper frequency and amplitude of the electric potential function applied to the trap electrodes, should propagate trough the trap in a periodic manner, constraint in its size, and deposit on the collector in confined deposition pattern. Fig. 4.6.
Performed series of experiments partially proved this hypothesis, but also shown

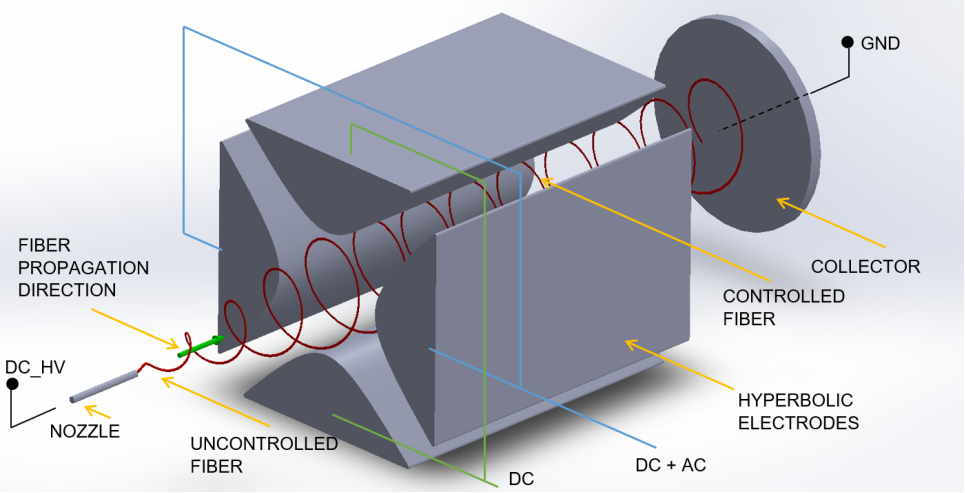

Figure 4.6: 3D schematic of a Paul's linear quadrupole trap acting on a electrospun charged fiber, constraining it from expansion and leading to a circular deposition.

significant limitations of this fiber steering method. With low frequency of the forcing function, regardles of its amplitude, the fiber was depositing on the surface of these auxiliary electrodes and so no or very little amount of fiber was collected on the collector electrode. With frequency of the forcing function increased above the threshold value, when the fiber can not reach the auxiliary electrodes, four different fiber extrusion regimes in terms of amplitude of the electric potential applied to these auxiliary electrodes were observed:

- Critically low applied electric potential - electric potential on the auxiliary electrodes lower than the potential on the fiber in given region of the trap, leading to fiber deposition on the surface of auxiliary electrodes

- Insufficient electric potential - auxiliary electrode electric potential is higher than the fiber potential at given location, but generated external electric field and Coulomb forces exerted on the fiber by this field are not sufficient to steer the fiber and trap it in a periodic or quasi-periodic movement.

- Optimal electric potential - external electric field generated by auxiliary electrodes effectively steers the fiber and keeps it in a periodic or quasi-periodic oscillatory movement leading to distinguishable deposition pattern.

- Overwhelming electric potential - analogically to reverting electric field described in electrostatic focusing, when the electric potential applied to auxiliary electrodes is higher than certain threshold potential given for the individual electrospinning setup, the fiber propagation direction is reverted, and fiber is forced to collect on other device components and enclosure walls.

Fig.4.7 shows the experimentally obtained deposition pattern as a function of the electric potential function applied to electrodes of Paul‘s linear quadrupole trap. Impact of the two cases of forcing function amplitude previously described were investigated. In upper row, the optimal forcing function amplitude was used, where the fiber deposit resembled the most visible pattern. In the bottom row, amplitude of the forcing function was lowered, and so the ability of the quadrupole trap to influence the fiber extrusion. Fiber than exhibited more random oscillation, longer time to converge to the stable deposition pattern or deposition pattern shift within the four quadrants of the trap. Fiber at lower frequency was partially able to move from quadrant to quadrant, as it had more time to travel laterally in one direction within one half cycle of the forcing function. As the frequency increased, fiber was trapped in one of the four quadrants, and oscillated only within the quadrant. Experiments showed, that the initial conditions did not pre-determine the quadrant of oscillation of the fiber, and it was rather given by the construction inaccuracy. Also, the previously deposited fiber on top of one of

the auxiliary electrodes sufficiently influenced the generated electric field and the fiber propagation quadrant. With listed electrospinning parameters, fiber deposited on surface of the auxiliary electrodes for frequencies lower than 50 Hz, and so the deposits for higher than this frequency are shown. From frequency of the forcing function f=100 Hz, the deposition pattern does not change with further frequency increase, only shrinks in size. At frequency about 200Hz, the deposit reached its minimal size of about 1mm and did not continue shrinking with increasing frequency. There are multiple possible reasons to this:

- Electric resistance of the collector plate is too high, leading to impaired charge dissipation from its surface, and therefore to a fiber deposition region drift.
- External electric field generated inside the trap is insufficient to focus the fiber to the axis of the device any further because the internal coulomb force from charged particles of this fiber is too high. With increase of the forcing function amplitude, the axial electric field would become negative and fiber would not be able to enter the trap and would be reverted.
- The fiber was de-focused in the region between the trap and the collector plate, as the quadrupole generated lateral electric field in this region is minimal, but fiber still retain some electric charge crating the internal coulomb forces causing the bending instability.
- Deposition region growth is caused by the mechanical buckling at fiber contact at high velocity with the static collector plate

When the collected nanofiber was investigated under the microscope, it showed no improvement in terms of straightness. The quadrupole trap was only partially able to control the macroscopic fiber alignment into previously described patterns,

while not influencing the microscopic alignment at all. If the lateral electric field components along corresponding lateral axes of the device (in between auxiliary electrodes) are compared, it could be seen, that quadrupole trap and previously studied (4.1) 1x2 electrode in anti-phase electrode setup generate the same maximum lateral electric field. This is, however, in proximity to the auxiliary electrodes. The fiber propagates only within millimeters from the axis of the device. In this region, lateral electric field generated by the quadrupole trap is almost negligible compared to the lateral electric field generated by the two electrodes in anti-phase. To increase the lateral electric field in the 2D electrodynamic focusing, the 1D electrode setup was expanded. Comparison of the lateral electric field components in between the auxiliary electrodes for these two 2D steering electrode setups is shown in Fig. 4.8.

If the electric field distribution over the trap is compared to a previously investigated 1D electrodynamic fiber steering, it can be seen, that in quadrupole trap it is significantly lower, eventhogh the potential function amplitude and electrode separation is the same. This is because the set of DC electrodes is kept at average of the AC electrodes and then the potential difference is half of the potential difference between two auxiliary electrodes used in 1D steering.

4.2.2 2x2 Electrodes in Anti-phase

Electrode Layout of the 2D steering expansion of previously described 1D steering in electrospinning device is shown in Fig. 4.9

In this case, the two pairs of auxiliary electrodes are offset along the axis of the device and rotated by 90 degrees with respect to each other. As the fiber travels through the region of the first electrode pair(vertical), it is aligned horizontally as previously described in 1D steering. The second, horizontally aligned, pair of electrodes stretches the fiber in vertical direction. Fig. 4.10 and Fig. 4.11 show

fiber deposits for tested frequency range of 40-200 Hz for two different solutions of PEO [50]. Water based, and ethanol-based. Comparing the fiber deposition pattern for the two used solutions, the solvent material composition did not influence it, and the fiber under 2D steering deposited in elliptical deposition regions in both cases. However, comparing the size of these elliptical deposits (with the two different polymeric solutions but same frequency of the forcing function), it can be seen, that the EtOH based solution led to smaller deposition regions. This can be attributed to multiple factors. EtOH has a lower boiling point and lower density than DiH_2O. Faster evaporation of the EtOH-based solvent leads to higher viscoelastic force, and fiber stretch is therefore limited. EtOH also has lower dielectric constant and dipole moment, hence this solvent is subject to lower elongation forces[51]. Effect of this can be also seen from Fig. 4.4, where the fibers spun from EtOH-based solution were reaching lower fiber velocity than the fibers spun from DiH_2O-based solution.

As with the 1D steering, also in 2D steering, higher forcing function frequency led to a smaller deposition region. Deposition time in these shown experimental results was from 10 to 20 seconds. For lower forcing function frequency, higher deposition time was used, as the fiber deposit is larger. Short deposition times were used to keep the deposit as sharp as possible. With longer deposition times, residual charge on the collected fiber causes the deposition pattern drift, and the deposition region is "de-focused". This can be seen from Fig. 4.12, where the same setup was used for 10 min long fiber deposition. Further increase in deposition time did not show any further drift in the deposition region. Electrospinning setup leading to presented fiber deposits with 2D focusing was: Nozzle Voltage $NV = 8\,kV$, Auxiliary electrode separation(in lateral direction) $EE_{x,y} = 110\,mm$, Separation of the two Auxiliary Electrode Planes(in axial direction)$EE_z = 25\,mm$, Nozzle to Collector distance $NC = 90\,mm$, Nozzle to 1st electrode pair distance $NE_1 = 15\,mm$.

Size of the elliptical deposit with respect to frequency of the forcing function is shon in Fig. 4.13, where simulation (considering Kelvin Voigt material model

described in section 5.2, and Maxwell material model described in section 5.3) and experimental results are shown. It can be seen, that with increase of frequency, size of the deposit shrinks, as it was for the 1D fiber steering.

Orientation of the elliptical fiber deposit depends on the application of forcing function to auxiliary electrodes. This is shown in Fig. 4.14

The tilt of the deposit is given by the collector electrode position along the axis of electrospinning device with respect to the auxiliary electrodes. If moved in between the two auxiliary electrode planes, vertical orientation of the ellipse can be achieved. Eccentricity of the ellipse is given by the separation of these two auxiliary electrode planes. If all four electrodes are placed in one plane, fibers are collected as a diagonal line. With increasing offset of the two electrode planes, eccentricity of the elliptical deposit decreases. This can be seen in Fig. 4.15, where four different values for the electrode pair separation were used. Circular deposition, however, has not yet been achieved.

Lateral position of the elliptical deposit within the collector electrode (diagonals of the square crated by auxiliary electrodes, when looking from the tip of the nozzle along the axis of the device) on the collector can be controlled by adjustment of the duty cycle of the forcing function applied to auxiliary electrodes. Three different functions in terms of duty cycle and resulting fiber deposit are shown in Fig. 4.14

Investigating microscopic alignment of the collected fiber reveals, that it stays buckled even in case of 2D steering. It does not have such dense buckles as in case of 1D steering created at the ends of line-like deposits, but this buckling is more evenly distributed over the length of the deposited pattern. This can be seen in Fig. 4.17

Addition of another electrode pairs to the electrospinning device did not improve neither the macroscopic alignment (sharpness of the deposit), nor the microscopic fiber straightness. Up to eight electrode pairs (16 auxiliary electrodes) were used.

4.3 Impact of Fiber Steering on Fiber Properties

In previous sections of this chapter, it was shown how electrodynamic fiber steering influences its deposition on a static, grounded collector electrode. This section discusses impact of such steering on the collected fiber properties. As was shown in Fig. 4.4, velocity of the fiber propagation depends on the frequency of the potential function applied to auxiliary electrodes. Based on this, an assumption that electrodynamic steering of different frequency would lead to different fiber stretch (and therefore different fiber diameter) was built. To examine this, a series of SEM images of unsteered, 1D steered and 2D steered fibers were investigated and compared. Fig. 4.18 shows an SEM image of one of each fiber deposit. It was found, that the fiber diameter in all three cases (no steering, 1D steering and 2D fiber steering) was the same. It was ranging from 240 nm to 300 nm. This means, that the electrodynamic steering does not provide any additional stretch of the fiber, but only partially straightens it, and aligns it.

A reason for this might be, that the majority of the fiber inside the steering device is already dry, and so solid. Therefore, the fiber does not stretch any longer, and its diameter stays constant. Dryness of the fiber we investigated by collecting it at various nozzle-to-collector (NC) distances and investigating by the optical microscope. Fig. 4.19 contains a set of images of the fiber collected at various NC distances. The wet fiber in these figures can be recognizes as a thick fiber, or close to drying, as a fiber that does not undergo the buckling instability as it deposits on the collector electrode. The later can be seen in the steered fiber deposit collected at NC=45 mm, or in the unsteered fiber collected at NC=60mm. The performed set of experiments contained the unsteered fiber extrusion, and electrodynamically steered fiber extrusion, with frequency of the forcing function ranging from 40 Hz to 160 Hz. The average fiber drying distance of electrodynamically steered fiber was

found to be NC=45.8 mm, with standard deviation of =2.18 mm. The unsteered fiber extruded under the same working parameters dries on average in NC=66.75 mm, with =3.03 mm. This set of experiments was performed with the nozzle voltage at 8kV. Results of the fiber drying distance were used in the mathematical model development, described in the following chapter of this work.

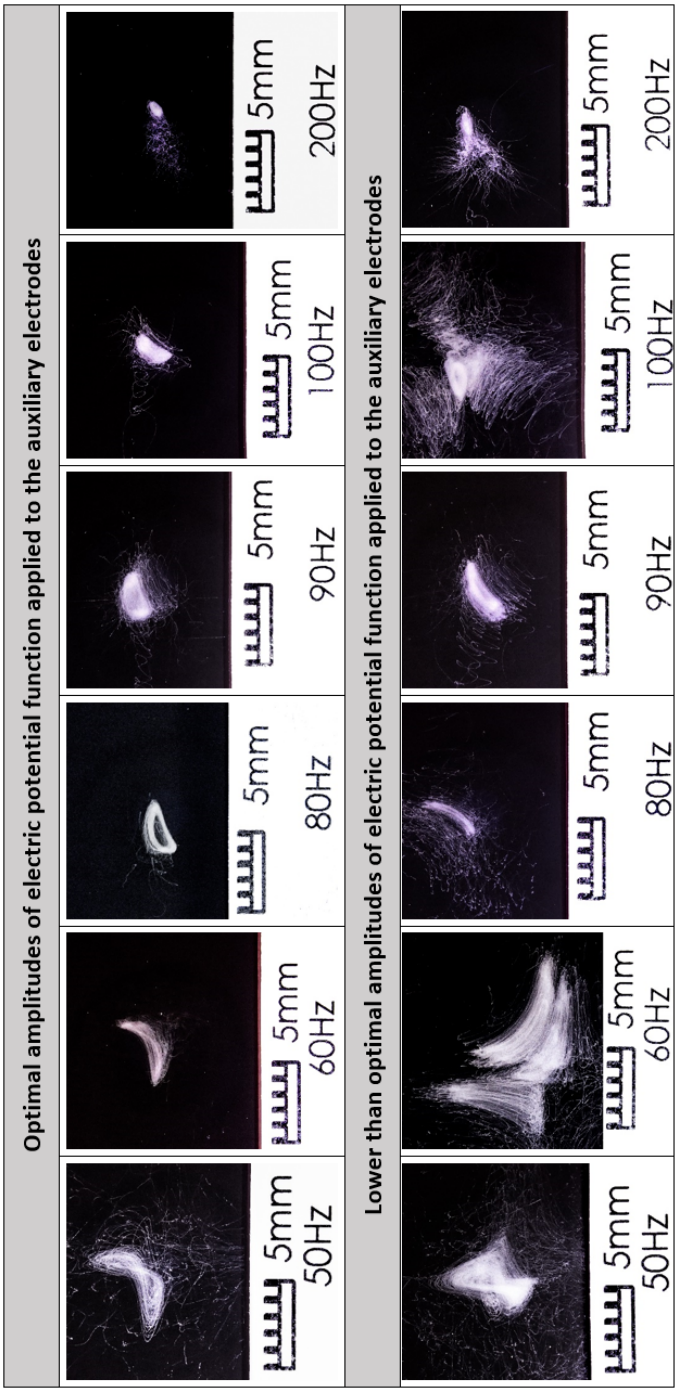

Figure 4.7: Experimentaly obtained fiber deposition pattern as a function of the forcing function frequency and amplitude applied to electrodes of the linear quadrupole trap.

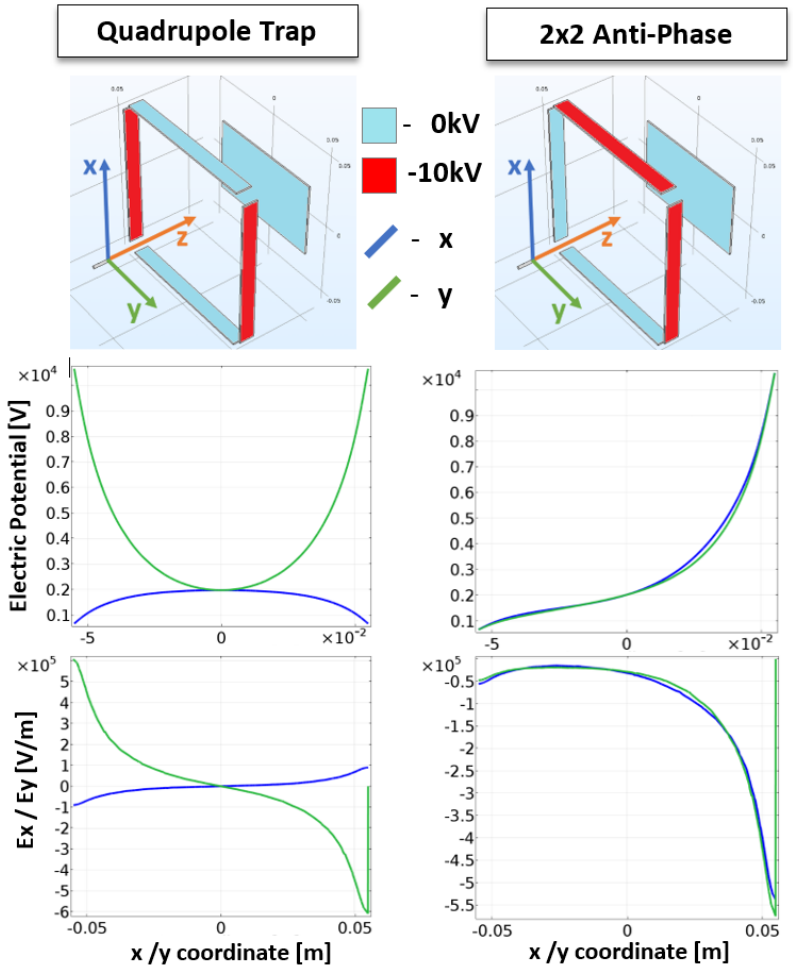

Figure 4.8: FEA analysis of lateral electric field components in between the auxiliary electrodes of the linear quadrupole trap and expanded 1D steering. Results are shown for one state of the applied potential function. In the other one, high and low potentials applied to electrodes would be simply swapped.

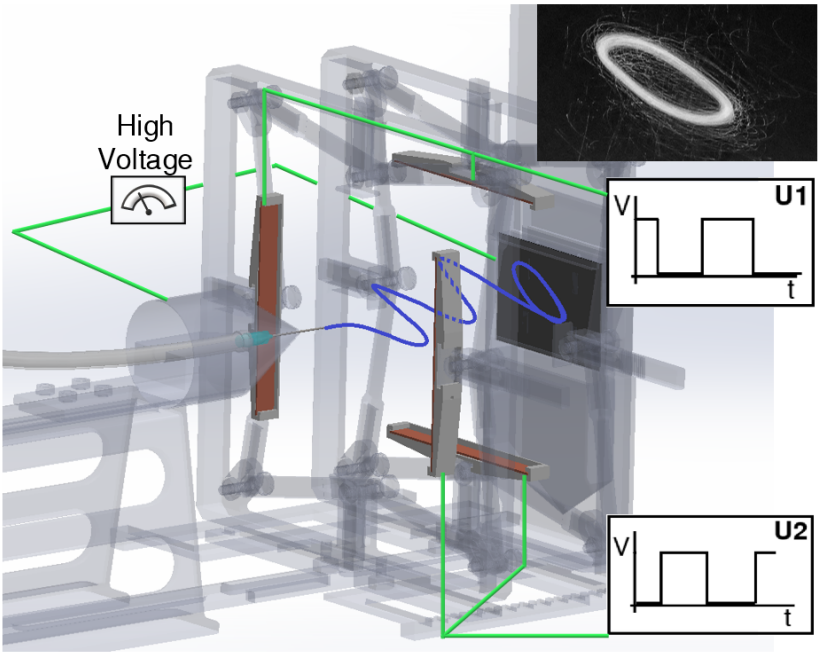

Figure 4.9: Electrospinning device with two pairs of auxiliary electrodes, for 2D electrodynamic steering of the fiber. Visualization of the fiber behavior within the device is shown in blue, and an actual fiber deposit obtained experimentally with 2D electrodynaic steering is shown in upper right corner.

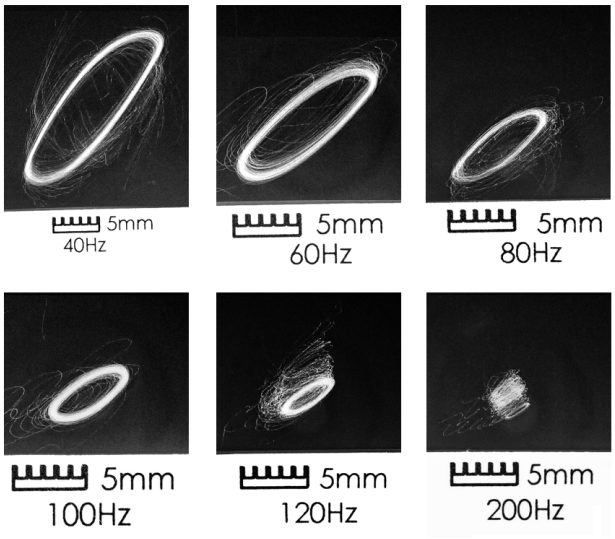

Figure 4.10: Experimentally obtained electrospun PEO nanofiber deposition patterns from PEO + DiH_2O solution, and their dependence on the frequency of forcing function applied to auxiliary electrodes in 2D electrodynamic steering.

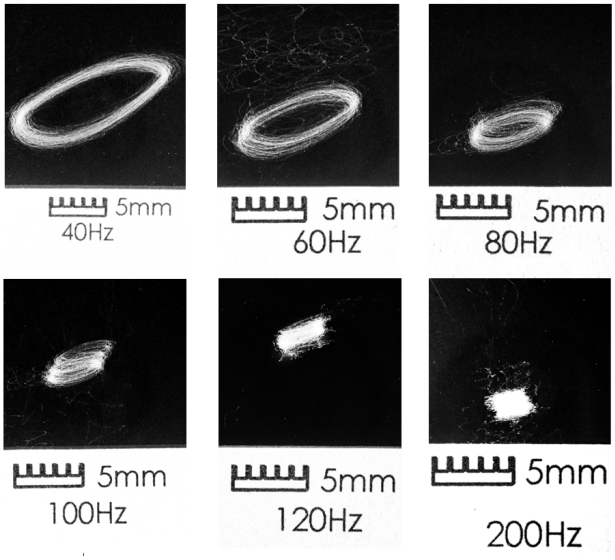

Figure 4.11: Experimentally obtained electrospun PEO nanofiber deposition patterns from PEO + EtOH + DiH_2O solution, and their dependence on the frequency of forcing function applied to auxiliary electrodes in 2D electrodynamic steering.

Figure 4.12: Experimentally obtained electrospun PEO nanofiber deposition patterns from PEO + EtOH + DiH_2O solution with frequency of the forcing function f=40 Hz with deposition time of T=10 min.

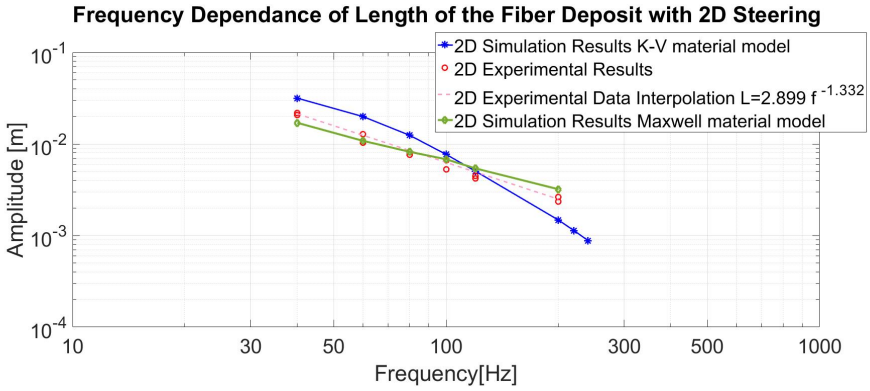

Figure 4.13: Dependence of the length of the fiber deposit on frequency of the forcing function in 2D steering settings. Length of the deposit is a size of the ellipse along the semi-major axis. Electrospinning parameters: Nozzle to collector distance $NC = 90\,mm$, Nozzle to 1st auxiliary electrode pair $NE_1 = 20\,mm$, 1st Electrode Pair to 2nd Electrode Pair $EE_Z = 25\,mm$, Electrode separation $EE = 110\,mm$, Nozzle voltage $NV = 7\,kV$, Flow rate $FR = 0.06\,ml/hr$.

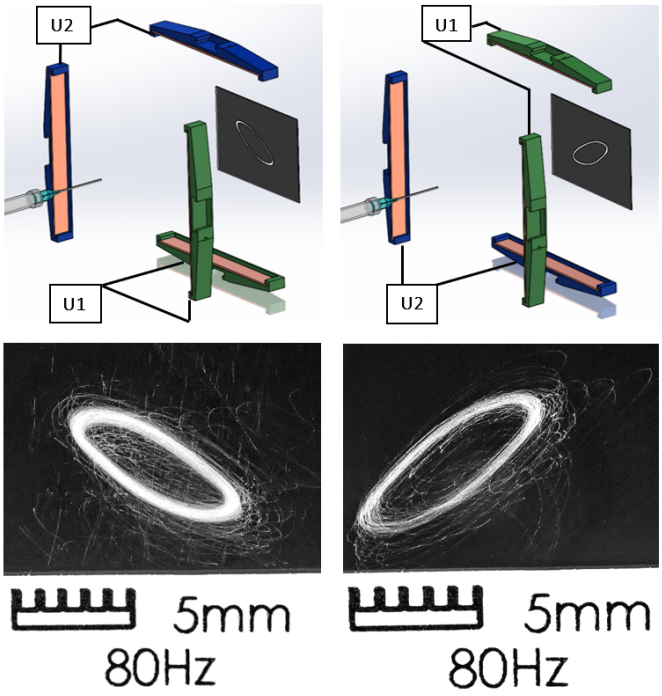

Figure 4.14: Orientation of the elliptical deposition region based on the auxiliary electrode pairing (application of the AC potential on auxiliary electrodes).

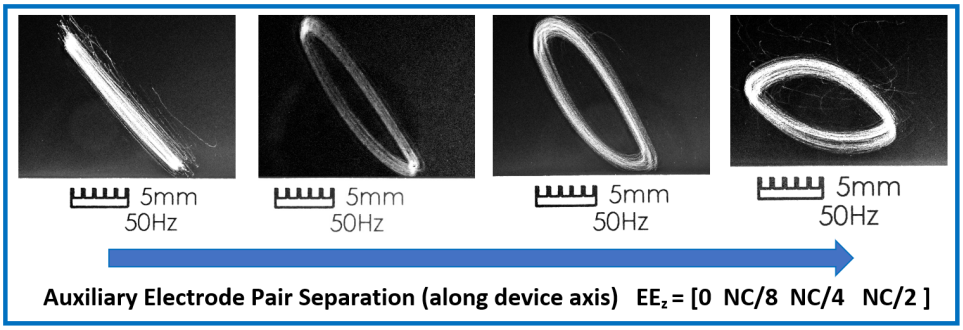

Figure 4.15: Fiber deposit dependency on axial separation of the two electrode pairs in 2x2 electrodes in anti-phase setup.

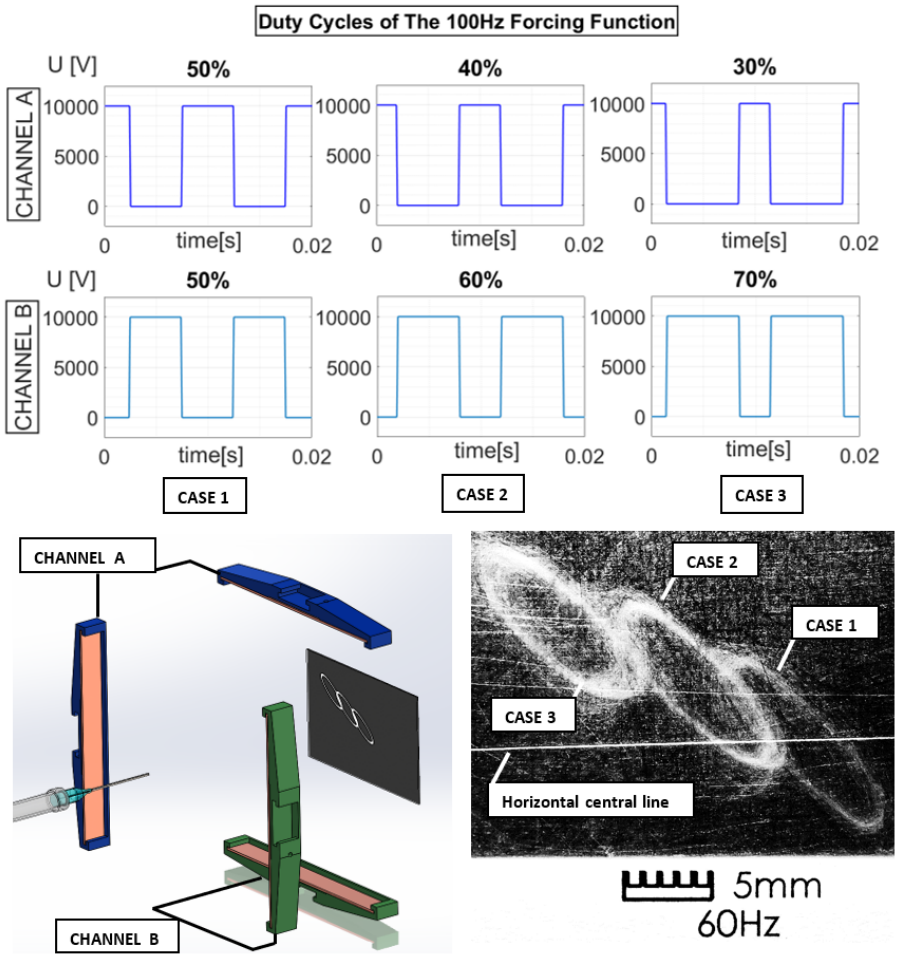

Figure 4.16: Impact of a different forcing function duty cycle on a lateral position of the fiber deposit

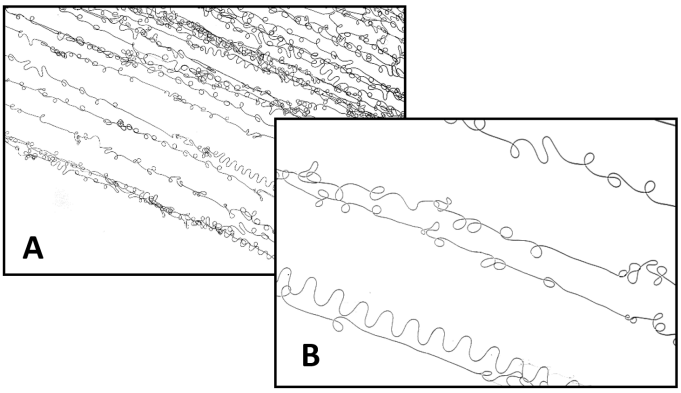

Figure 4.17: Microscopic view of the deposited electrospun fiber with 2D steering at 40 Hz. A: 100x Zoom, B: 200x Zoom.

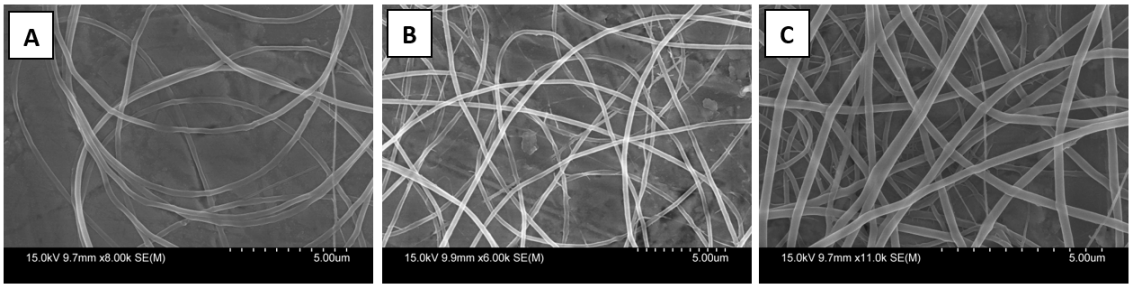

Figure 4.18: Sequence of SEM images of PEO fiber extruded from solution of $6wt\%$ of PEO, $74wt\%$ of EtOH and $20wt\%$ of DiH_2O. A- unsteared, B- with 1D electrodynamic steering at f=80 Hz, C- 2D electrodynamic fiber steering at f=80 Hz.

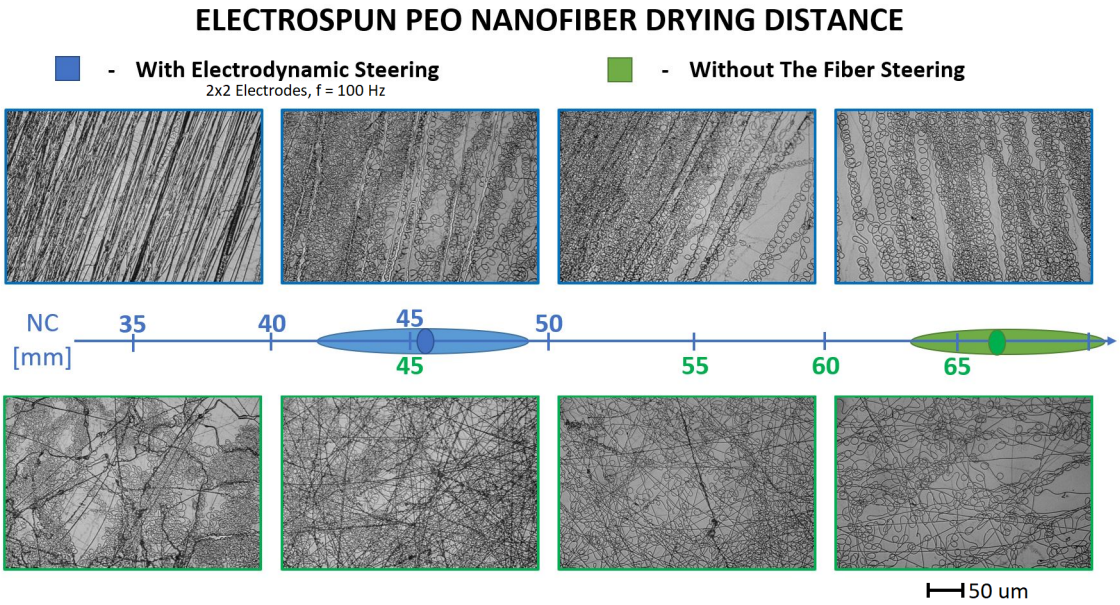

Figure 4.19: Sequence of fiber deposits at different nozzle-to-collector (NC) distances, for both electrodynamically steered fiber(top row-blue), and unsteered fiber(bottom row-green). The average drying distances are marked on the axis by two dark ellipses of corresponding color, with wider ellipse representing the range of measurements

Chapter 5

Mathematical Modelling

5.1 External Electric Field

Regardless of the developed model of the fiber itself, knowing the electric field distribution within the electrospinning device is one of the vital aspects of development of reliable electrospinning fiber extrusion model. Especially, as the emphasis lies on the electrodynamic steering of this extruded fiber. The electric potential distribution and its derivative, electric field, can be obtained analytically for specific focusing devices like a linear quadrupole trap. In Paul's linear quadrupole trap (in our case expanded by the axial coordinate (z-axis) dependent term), electric potential distribution is described by equation Eqn. 5.1.

$$\Phi = \frac{1}{2}\left(U_{DC} + U_{AC}\cos\left(\omega\, t\right)\right)\left(\alpha x^2 - \beta y^2\right) - \gamma\, z \tag{5.1}$$

where α, β and γ are coefficients corresponding to the electrode geometry. Linear electrostatic traps typically operate in two-directions using a alternating fields. In a given cycle, one of the directions has confining action, while the transversal direction is anti-confining. By choosing a frequency that matches the motion of the fiber, it is possible to constrain it to a quasi-periodic trajectory by alternating the confining and anti-confining directions. This is illustrated by the electric field in the trap (x - confining, y - anti-confining) in Eqn. 5.2 and 5.3, respectively. The electric field along the z-axis of the device is described by Eqn. 5.4 and is not intended to confine the fiber.

$$E_x = -\frac{\partial \Phi}{\partial x} = -\alpha\left(U_{DC} + U_{AC}\cos\left(\omega\, t\right)\right) x \tag{5.2}$$

$$E_y = -\frac{\partial \Phi}{\partial y} = \beta \, (U_{DC} + U_{AC} \, \cos(\omega \, t)) \, y \tag{5.3}$$

$$E_z = -\frac{\partial \Phi}{\partial z} = \gamma \tag{5.4}$$

To satisfy the Laplace equation, ($\Delta \, \Phi = 0$) one arrives at $\alpha = \beta$, which should hold under the assumption that the net charge on the fiber is small compared to the charges on the confining electrodes. Then external electric forces on a fiber segment with an electric charge of Q are as given in Eqn. 5.5, Eqn. 5.6 and Eqn. 5.7.

$$F_x = -\alpha \, Q \, (U_{DC} + U_{AC} \, \cos(\omega \, t)) \, x \tag{5.5}$$

$$F_y = \alpha \, Q \, (U_{DC} + U_{AC} \, \cos(\omega \, t)) \, y \tag{5.6}$$

$$F_z = \gamma \, Q \tag{5.7}$$

Then equations of motion for single charged particle, of mass M and electric charge Q, in a linear quadrupole trap in transverse direction are described by the Mathieu equation Eqn.5.8,. Axial propagation of the particle throughout the trap is described by Eqn. 5.10.

$$\frac{d^2x}{dt^2} + \alpha \, \frac{Q}{M} \, (U_{DC} + U_{AC} \, \cos(\omega \, t)) \, x = 0 \tag{5.8}$$

$$\frac{d^2y}{dt^2} - \alpha \, \frac{Q}{M} \, (U_{DC} + U_{AC} \, \cos(\omega \, t)) \, y = 0 \tag{5.9}$$

$$\frac{d^2x}{dt^2} - \gamma \, \frac{Q}{M} = 0 \tag{5.10}$$

Analytical solution and stability regions of the Mathieu equation are known [**?**] in terms of frequency and amplitude of the applied harmonic forcing function. In

our application, strings of charged particles are propagating through the trap. This not only introduces additional non-linear terms in equations of motion (mechanical forces, internal Coulomb forces, Stokes drag force), but also significantly increases the number of degrees of freedom (based on fiber discretization). Analytical solution of such system of differential equations becomes not practically feasible, and so the system stability regions need to be found using numerical and experimental studies.

5.2 Kelvin Voigt model

To predict the behavior of the fiber extruded with different electrospinning device parameters or electrode layouts, mathematical model of the fiber was created. Initially, a simple model, where the fiber was discretized into just five beads was assumed. Mass and electric charge on the fiber were then divided and assigned to the beads. As discussed in chapter 4, majority of the fiber inside the steering device is already dry. For this dry (solid) fiber, Kelvin-Voigt material model is more suitable than Maxwell material model, generally used for the initial stages of the jet extrusion with a significant strain. Also, for this fully solidified fiber, material properties (density, Young‘s modulus, etc.) of the PEO need to be used, as opposed to the material properties of the polymeric solution. Furthermore, a steady-state mass distribution inside the device is assumed, where these was no net accumulation or loss of mass at each node. This allowed for the beads to be fixed in transverse planes. Fig. 5.1 contains a visualization of this model, and corresponding equations of motion are sown in Eqn. 5.11[52].

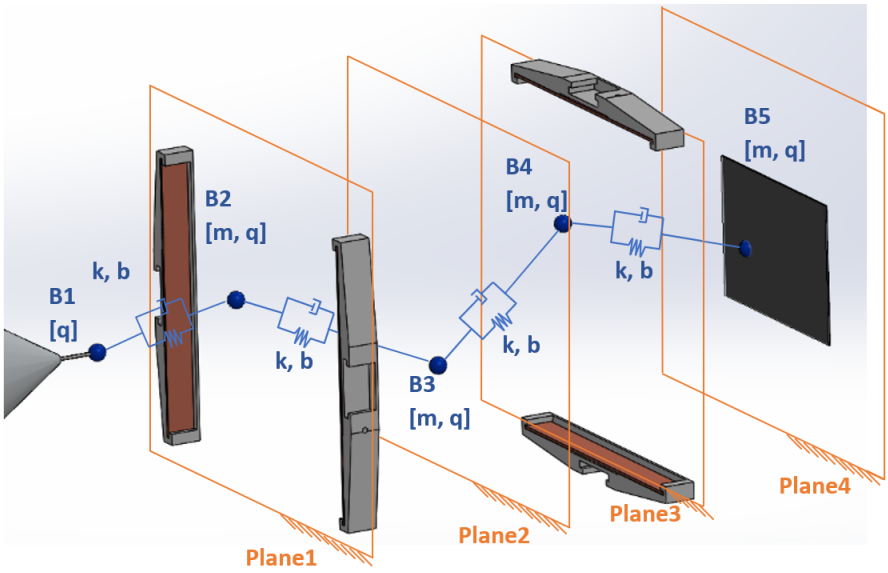

Figure 5.1: Kelvin-Voigt material model of the discretized nanofiber. Bead B1 is fixed, and beads B2 through B5 are restricted to move in x-y planes 1–4. External coulomb forces from electric field created by auxiliary electrodes are applied to beads B2–B4.[7]

$$
\begin{aligned}
& m\,\ddot{x}_{j,i} + c_{Stokes}\,\dot{x}_{j,i} + c_{struct}\,\frac{d\,L_{i,i-1}}{d\,t}\,\frac{(x_{j,i} - x_{j,i-1})}{L_{i,i-1}} - c_{struct}\,\frac{d\,L_{i,i+1}}{d\,t}\,\frac{(x_{j,i} - x_{j,i+1})}{L_{i,i+1}} + \\
& + k\,(x_{j,i} - x_{j,i-1})\left(1 - \frac{L}{L_{i,i-1}}\right) - k\,(x_{j,i+1} - x_{j,i})\left(1 - \frac{L}{L_{i,i+1}}\right) - \\
& - \sum_{k=1}^{n}\left(\frac{k_e\,(\lambda_q\,L)^2}{L_{i,k}^3}\,(x_{j,i} - x_{j,k})\right) + F_{i,j} = 0
\end{aligned}
\tag{5.11}
$$

where $j = [1, 2]$ $, i = [1, n]$ $, i, j \in N$. n is the number of beads to which the fiber is discretized (n=5 in this case), and j represents axis in Cartesian system.$x_{j,i}$ is then the j-th component of a position vector $\bar{x}$ of the i-th bead. $L_{i,i-1}$ is a length of the fiber segment between i-th and $(i-1)$-th bead and is expressed in Eqn. 5.12

$$L_{i,i-1} = \sqrt{\sum_{j=1}^{3} \left(x_{j,i} - x_{j,i-1}\right)^2} \tag{5.12}$$

λ_q is a linear charge density on the fiber, k_e is a Coulomb's constant $k_e = \frac{1}{4\,\pi\,\epsilon_0}$, c_{Stokes} is a Stokes drag coefficient, c_{struct} is a structural damping coefficient, L is the initial length of the fiber segment between two beads, and k is a PEO fiber stiffness coefficient. Mass of the fiber was calculated from density of the PEO $\rho_{PEO} = 1.21 \times 10^3 [kg/m^3]$. As described in previous section, from SEM microscopy of the deposited fiber,its diameter is constant for both electrodynamically steered and un-steered extrusion. The constant diameter of 300 nm was then assumed for the whole fiber model. Mass concentrated in a bead is then given by Eqn. 5.13, where A is a fiber cross-section and L is length of the fiber segment.

$$m = L\,A\,\rho = \frac{\pi\ \left(3 \times 10^{-7}\right)^2 [m^2]\, 1.21 \times 10^3 [kg/m^3]\, L[m]}{4} = 1.71 \times 10^{-12} [kg]$$
$$\text{for } L = 2 \times 10^{-2} [m] \tag{5.13}$$

Linear charge density on the fiber was calculated from electric current measurements on the collector electrode and from the fiber arrival rate v. In Eqn. 5.14, I is an electric current on the fiber, calculated from Ohms law. U is a potential measured on the collector electrode and R is the resistance between this electrode and ground. Dividing the electric current on the fiber by its velocity gives the amount of electric charge carried by the fiber per its length. Average fiber velocity, or fiber arrival rate, of $v = 4.8[m]$ was estimated from length of the fiber collected per half period of the forcing function. From the series of performed experiments, the fiber velocity decreases with increasing forcing function frequency (6.6 m/s at f=40 Hz to 3m/s at f=320 Hz), but stays approximately the same for 1D and 2D fiber steering.

$$\lambda_q = \frac{I}{v} = \frac{U}{R\,v} = \frac{0.055[V]}{153\,[\Omega]\,4.8[m/s]} = 7.49 \times 10^{-8} [C/m] \tag{5.14}$$

As the deposited fiber is dry, and so non-conductive, flow of electrons from grounded collector electrode through the fiber is not assumed. The electric current I measured, is then considered to be solely from charge carried by the fiber.

Stiffness of the fiber was initially taken from interval of published values obtained from AFM measurements of the PEO fiber stiffness [53], and then eventually adjusted, so the simulations match the experimental results. Adjusted Young modulus was still kept within the value interval reported by above referenced articles. Fiber stiffness coefficient is a function of Young modulus, fiber diameter and its length, as shown in Eqn. 5.15.

$$k = \frac{E\,A}{L} = \frac{7 \times 10^{9}[Pa]\,\pi\,\left(3 \times 10^{-7}\right)^{2}[m^{2}]}{4\,L[m]} = 0.0247[N/m] \qquad if\ L = 2 \times 10^{-2}[m] \tag{5.15}$$

There were two different types of damping considered in the model. Structural damping and Stokes drag. Stokes drag coefficient was first calculated as in Eqn. 5.16, as for a non-spherical particle movement at low Reynolds number (Re=0.08) [54].In Eqn. 5.16, an equivalent diameter of the needle-like particle is calculated as $\mathrm{d}_{eq} = d\left(\frac{L}{d}\right)^{1/3}$, μ is the dynamic viscosity of the air, and the shape correction factor f_{shape} is given by Eqn. 5.17. In this equation, E is the aspect ratio of given non-spherical (needle-like) particle. $E = \frac{d}{L}$. Based on the equivalent diameter, the Knudsen number is $Kn = 0.0053$, leading to the Cunningham slip correction factor of C=1.014, which is within the noise of the simulation. As shown in the Fig. 5.1, model of the discretized fiber consists of straight segments of significantly lower length than the electrospun fiber length is in reality. Therefore, the above obtained Stokes drag coefficient would be underestimated, and so it was a subject to an adjustment, together with the structural damping coefficient. Final adjusted values of Stokes drag coefficient of $C_{Stokes} = 2.3 \times 10^{-6}[Ns/m]$ and structural damping

coefficient of $C_{struct} = 1 \times 10^{-5}[Ns/m]$ were used.

$$C_{Stokes} = 3\pi\mu_f \, d_{eq} \, f_{shape} = 4.35 \times 10^{-7} \, [Ns/m] \tag{5.16}$$

$$f_{shape} = \frac{\frac{4}{3}E^{\frac{2}{3}}}{\ln 2E - \frac{1}{2}} \tag{5.17}$$

External Coulomb forces $F_{i,j}$ are nonzero for beads inside the device (beads 2-4), and were obtained from an FEA analysis of the electrospinning device with corresponding electrode layout. Electric field x and y components were found as a function of x and y coordinate in x-y planes, where beads are located. These electric field components are shown in Fig. 5.2, together with the electric potential distribution in these x-y planes (Plane 1 – Plane 3).

Simulation results for 1D steering are simply lines of different lengths that can be seen in Fig. 4.2. 2D steering simulation results, are shown in FIG.5.3 and the deposition region size dependency on a forcing function frequency is shown in Fig. 4.10.

To better match the size and shape of the simulated deposition pattern with experimental results, structural damping coefficient of the fiber and Stokes drag coefficients were varied. Damping coefficients were chosen for the tuning of the model, as these were the material properties that could not be measured or found in available literature.

Simulation data show, that the value of an air drag coefficient significantly influences the fiber behavior, what is in contrast with previous findings [13]. Neither simulations, nor the experimental results performed within the frequency range of 20 – 400 Hz, found any resonance peaks. Fiber behaved as an over-damped system, with decreasing oscillation amplitude over increasing forcing function frequency. However, this model does not represent the fiber movement very well, as it does not

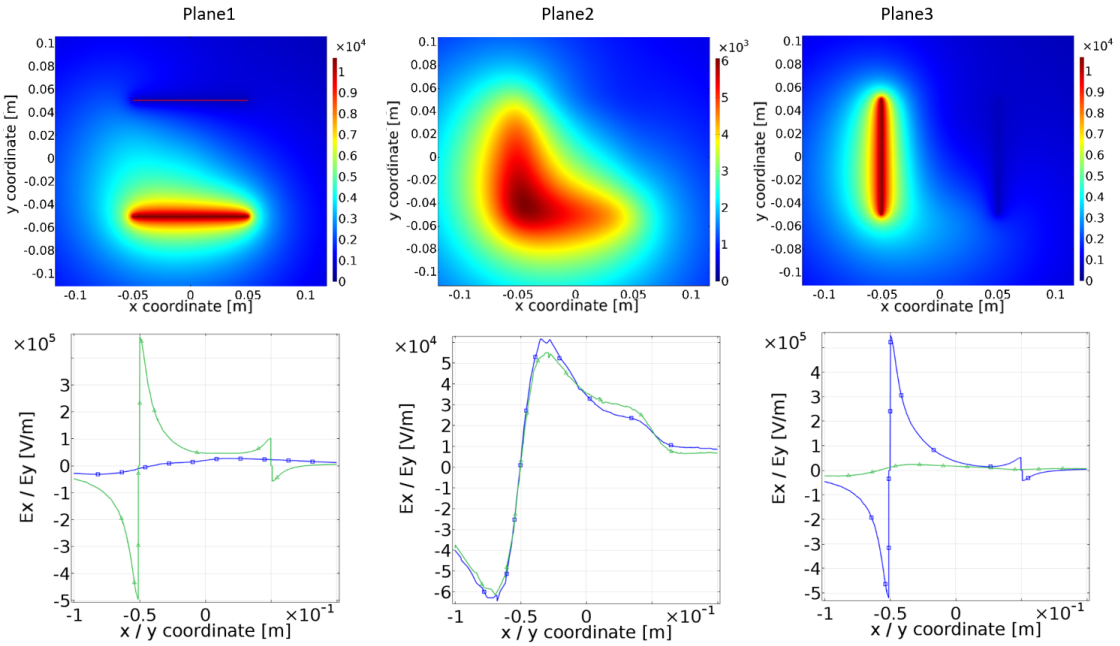

Figure 5.2: Top row: Electric potential distribution in planes 1-3; Bottom row: Electric field x(blue square) and y(green triangle) components along x resp. y axis in planes Plane1 - Plane3.

exhibit the coiling, caused by the electric charge driven bending instability. Nor it reliably represents the fiber behavior and deposition, in various auxiliary electrode configurations. For this reason, a less constraint model, with more degrees of freedom was constructed.

5.3 Maxwell Material Model

Most of the researchers focusing on electrospinning process modeling are using Maxwell material model [8, 13]. Reason for this is, that it is a viscoelastic material model, having both elastic and viscous properties. Maxwell material model can be represented by a pure viscous damper and purely elastic spring connected in

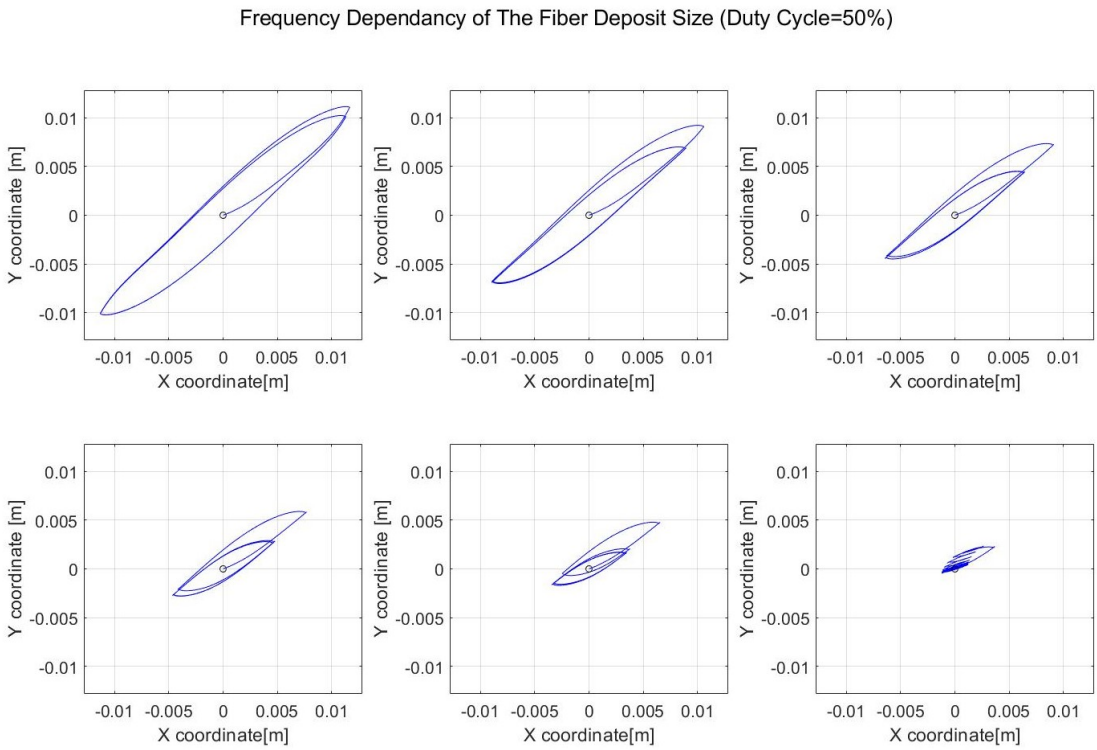

Figure 5.3: Simulation results with external Coulomb forces corresponding to a 2D electrodynamic steering. Results are for range of frequencies $F = [40, 60, 80, 100, 120, 200]Hz$

series, as shown in the Fig. 5.4

Considering the inertial forces, viscoelastic forces and surface tension of the liquid solution, Coulombic repulsion between individual beads, external Coulomb forces exerted on each bead by the electric field generated by all the electrodes in electrospinning device and Stokes drag force from fiber movement in the air, the equation of motion for i-th bead in j-th direction is of the form as shown in Eqn. 5.18.

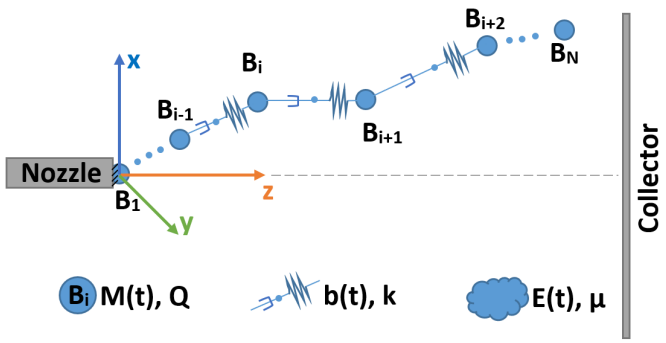

Figure 5.4: Electrospinning fiber extrusion model, assuming Maxwell - viscoelastic material.

$$
\begin{aligned}
\ddot{x}_{i,j}(t) = &-\frac{b_{ST_i} + b_{STOKES}}{M_i}\,\dot{x}_{i,j}(t) - \frac{k_{ST_i}}{M_i}\,x_{i,j}(t) - \\
&- \frac{k}{M_i\,L_{i,i-1}}\,(L_{i,i-1} - R_i(t) - L_0)\,(x_{i,j}(t) - x_{i-1,j}(t)) + \\
&+ \frac{k}{M_i\,L_{i,i+1}}\,(L_{i,i+1} - R_{i+1}(t) - L_0)\,(x_{i+1,j}(t) - x_{i,j}(t)) - \\
&+ E1_j(x_{i,j}(t))\,\frac{Q}{M_i}0.5\,(\mathrm{sgn}(\cos((\omega\,t))) + 1) - \\
&- E2_j(x_{i,j}(t))\,\frac{Q}{M_i}0.5\,(\mathrm{sgn}(\cos((\omega\,t + \pi))) + 1) + \\
&+ \frac{1}{M_i}\sum_{k=1}^{n}\left(ke\,q_k\,Q\,L_{i,k}^{-\frac{5}{2}}\,(x_{i,j}(t) - x_{k,j}(t))\right)
\end{aligned}
\tag{5.18}
$$

Here, $j = [1,3]$ $, i = [1,n]$ $, i,j \in N$. n again represents the number of beads in the system, which in this model grows with the fiber propagation, and index j represents axis of the Cartesian system.$x_{i,j}$ is then the j-th component of a position vector $\bar{x}$ of the i-th bead. $L_{i,i-1}$ is a length of the fiber segment between i-th and $(i-1)$-th bead and is expressed in Eqn. 5.12

The electric charge carried by the individual bead is Q. Charge dissipation of

the bead while it propagates trough the air is neglected. However, as the bead reaches the collector electrode, its charge starts to dissipate. That is why its charge changes to a function of time in the equation of motion. This is described in more detail in 5.3.2.

Terms containing coefficients b_{ST_i} and k_{ST_i} are additional viscous and elastic forces that represent surface tension of the liquid solution close to the tip of the nozzle, and are applied only in this region. These coefficients are described in more detail in 5.3.1.

Mass(M_i) concentrated in the individual beads of the discretized fiber, is similarly as the above described surface tension, function of the solvent evaporation, and is described in section 5.3.4.

Stokes drag coefficient(b_{STOKES}) was again calculated according to [54], shown in Eqn. 5.16 in section 5.2.

An additional time dependent term in the equation of motion($R_i(t)$), is a state variable containing information on the stretch of the viscous element of the fiber. The differential equation for this dash-pot stretch is expressed in Eqn. 5.19.

$$\dot{R}_i(t) = \frac{k\left(L_{i,i-1} - R_i(t) - L_0\right)}{b_{STRUCT_i}} \tag{5.19}$$

This additional state equation was obtained from the sum of the forces acting on the point in between the dash-pot and the spring. To keep these two elements in one line, these two forces, viscous and elastic, must be of same size and opposite direction. The damping coefficient b_{STRUCT_i} is a function of the bead‘s position along the axis of the design, and is designed to represent solidification of the fiber. Therefore, there is a minimum of the structural damping function at the tip of the nozzle, where the solution is of lowest viscosity, and increasing with distance

from the nozzle tip, reaching its maximum at the distance where the fiber is fully solidified, and staying high until the fiber‘s collection . Damping coefficient b_{STRUCT_i} as a function of the axial coordinate of the electrospinning device is shown in Fig. 5.10

External Coulomb force is calculated from the point charge approximation of the external electric field (named as$E1_j\left(x_{i,j}\left(t\right)\right)$ and $E2_j\left(x_{i,j}\left(t\right)\right)$ in the equation of motion) generated by electrodes of the electrospinning device, described in the section 5.3.3 of this chapter. As indicated, these electric field functions are functions of the position of the bead, and time. This means, that in every time-step, electric field components are obtained from the electric field approximation individually for every single bead.
In the following subsections, individual parameters of the simulation and fiber are discussed in greater detail, together with their impact on the fiber behavior.

5.3.1 Bead Creation

The simulation starts with just two beds with mass and electric charge, connected to each other via damper and spring in series. The first one is fixed at the tip of the nozzle, and the second one is free to move in all directions. Because of the Coulombic repulsion between these beads and because of the strong electric field generated by the nozzle, pointing outwards, exerting external Coulomb forces on the second bead, it accelerates away from the tip of the nozzle. This causes sudden deformation(elongation) of the elastic component and linear deformation(elongation) of the viscous element of the material. The elastic component then slowly starts to contract, as the viscous element continues to stretch. As the distance between these beads reaches twice the initial distance, new bead is added in between the two beads. The deformation of the spring stays the same, just the stretch of the damper

is reduced, as its stretch rate and not the stretch itself generates the viscous force acting on the bead. This way, no force impulses are introduced, other than the Coulombic repulsion between existing bead and the newly introduced one. To do this in MATLAB, ODE event function was used, to interrupt the solver when the distance between the first two beads reaches desired value($2L_0$). Then the number of beads is increased, what increases the length of the state vector by seven ($x, y, z, damper\ stretch, \dot{x}, \dot{y}, \dot{z}$). Initial conditions for the newly introduced bead are chosen in such way, that no additional disturbance to the system is introduced. Position of the bead is in between the two existing beads, velocity is equal to the moving bead, and initial damper deformation is calculated such the spring is initially undeformed. The ODE solver is then restarted, and the process keeps repeating until specified maximum number of beads is reached. Small perturbations in form of small changes in initial conditions of the introduced bead did not show any impact on the fiber behavior downstream.

To include the effect of surface tension of the liquid polymeric solution close to the tip of the nozzle, additional fiber stiffness and damping was introduced. Such radially acting damping and stiffness, even very small with respect to structural damping and stiffness of the fiber, helped to stabilize the fiber extrusion and reduced oscillation of the fiber in proximity to the nozzle. The damping and stiffness coefficients corresponding to the surface tension of the Taylor cone are shown in Fig. 5.10, in comparison to structural damping and stiffness coefficients.

5.3.2 Bead Collection

Initially, a bead reaching the collector electrode was removed from the system. This was done similarly to the new bead introduction, via additional ODE event function, checking a position of the last bead in the system. Removal of the bead reduced number of DOFs, and so limiting the system size. While it had a positive effect on the computation time, some important parameters of the device and fiber

properties were ignored. The most important ones are electric charge dissipation of the collected fiber and physical connection of the propagating fiber to the already collected one.

For this reason, beads reaching the collector electrode were fixed in space, and their electric charge was dissipated. Considering the underlying fiber layer as an dielectric in a capacitor, then this electric charge dissipation can be considered to be a capacitor discharge. Based on the time constant then the fiber behavior can be investigated. Resulting fiber deposition for two different values of the charge dissipation time constant can be seen in Fig. 5.5.

Physical connection between the propagating fiber and deposited fiber caused, that in some electrode configurations, segments of fiber upstream deposited prior to the downstream segments. For this reason, beads after the collection and charge dissipation still could not have been removed, as it could have caused such fiber loops to be cut. With no bead elimination, but fast addition at the tip of the nozzle, size of the solved systems grew very quickly, what significantly increased the computation time.

5.3.3 Point Charge Approximation

On top of the high number of degrees of freedom of the fiber model, various auxiliary electrode configurations and potential functions needed to be considered and examined. For this reason, numerical calculation of the electric field distribution over the analytical calculation was chosen.

Initially, nodal solutions of an FEA analysis for each desired auxiliary electrode configuration were imported to MATLAB, and four - dimensional function (x,y,z,U) was interpolated over the imported data. Derivative of the potential function with respect to x, y and z directions then led to corresponding components of the electric field function. Performing electrostatic FEA analysis in ANSYS or COMSOL and importing results into MATLAB proved itself to be neither practical, nor time

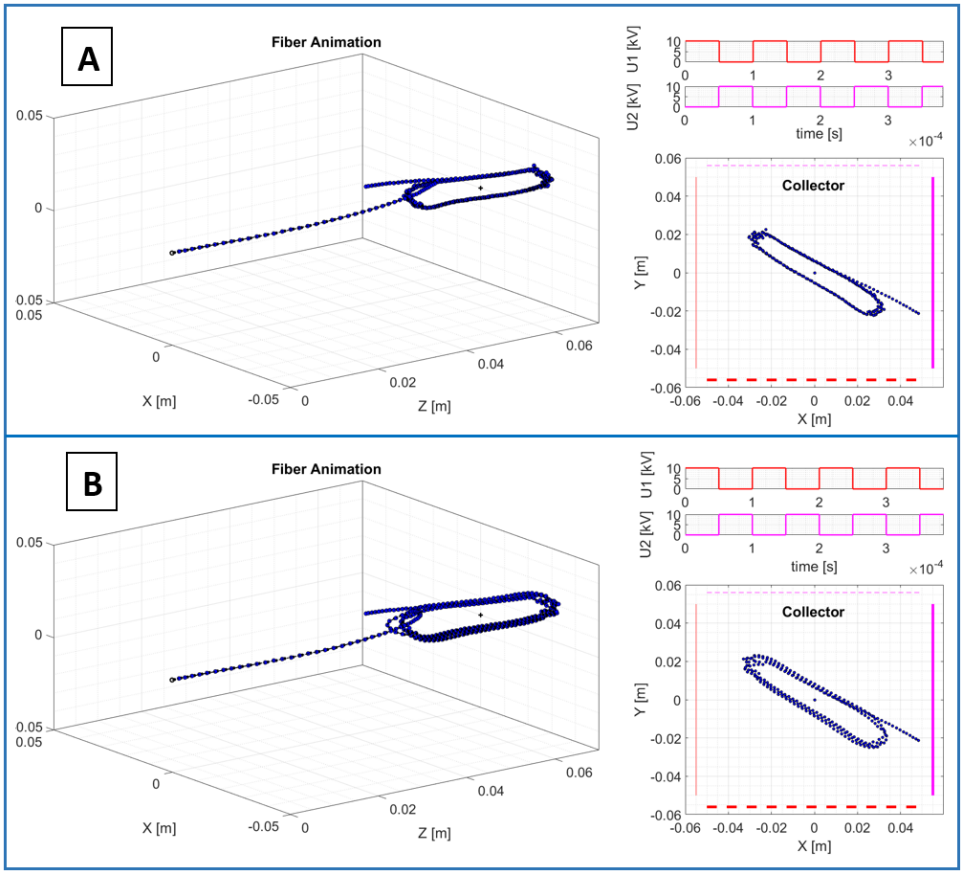

Figure 5.5: Simulated impact of an electric charge dissipation of deposited fiber on the fiber deposit. A - Charge dissipation time constant of $\tau = 10\,\mu s$, B - Charge dissipation time constant of $\tau = 1\,ms$. Experimental results are suggesting the time constant closer to the case B.

effective. Especially, if higher accuracy of the electric field distribution within the device is desired. For this reason, point charge approximation was added to the electrospinning model. Electric field components, as a function of location within the device were then built, and used in the fiber extrusion simulation. This electric field approximation was not only more accurate than high order polynomial interpolation over the FEA results, but also more time effective. This time effectiveness allowed the individual electric field component functions to be

called in every iteration, for every bead of the fiber. Comparison of the point charge approximation results and FEA(COMSOL) results for electric potential and field distributions is shown at the end of this sub-section

The point charge approximation assumes every electrode in the device to be discretized into a set of point charges. Electric potential at any point of the device is then given by the Eqn. 5.20, where Q_i is the electric charge on i-th point charge, r_i is the distance between each of these point charges and the point, at which the electric potential is calculated, and k_e is a Coulomb's constant. Coulomb's constant is $k_e = \frac{1}{4\pi\varepsilon_0} \doteq 8.988 \times 10^9\, Nm^2/C^2$.

$$\phi = \sum_{i=1}^{N} \frac{k_e\, Q_i}{r_i} \tag{5.20}$$

Individual electric field component functions, as gradients of the electric potential in individual directions are defined as in Eqn. 5.21. Here $j \in [1, 3]$, and so u_j represents the Cartesian coordinate. $\Delta u_{i,j}$ is then the distance between i-th point charge and the point of interest, in j-th direction.

$$E_{u_j} = \sum_{i=1}^{N} \frac{k_e\, Q_i}{r_i^2} \frac{\Delta u_{i,j}}{r_i} = \sum_{i=1}^{N} \frac{k_e\, Q_i\, \Delta u_{i,j}}{\sqrt{\sum_{j=1}^{3} \Delta u_{i,j}^2}^3} \tag{5.21}$$

To assign appropriate electric charge to the individual discretized points, MATLAB built in least square method - based optimization function was used. Initially, rough estimate for individual charges were assigned to this set of points, and electric potential at inspection points was defined. The inspection points were selected to lay on the surfaces of individual electrodes, so the electric potential at these inspection points was known. The optimization function then returns optimized point charges, which lead to smallest electric potential error at the inspection points. Electric field component functions were then built from such optimized point charges.

As a square potential function was applied to the auxiliary electrodes, two sets of

electric field functions were built. In the fiber extrusion simulation, corresponding electric field distribution function was called based on the simulation time and forcing function frequency.
Comparison of the electric potential distribution between FEA results and point charge approximation in multiple planes within the electrospinning device is shown in figures Fig. 5.6 and Fig. 5.7.

Electric field x and y components along these axis between both sets of auxiliary electrodes, and z component electric field along the axis of the device, for FEA and point charge approximation, are shown in figure Fig. 5.8.

As the applied potentials to the auxilary electrodes by the square functions are in this investigation always in anti-phase, two different potential functions were obtained. One for each state of the square potential function. These are the $E1_j\left(x_{i,j}\left(t\right)\right)$ and $E2_j\left(x_{i,j}\left(t\right)\right)$ functions in the equation of motion(Eqn. 5.18) of an individual bead in the developed Maxwell material model of the electrospun fiber.

With satisfactory accuracy of the electric field approximation used in the fiber extrusion simulation, fiber propagation and deposition with different settings of the auxiliary electrodes can be examined. As shown in Fig. 4.15, with increase of the auxiliary electrode pair separation along the axis of the device, eccentricity of the elliptical deposit increases. Response of the proposed fiber model to increasing separation of the electrode pairs is shown in Fig. 5.9. In simulation results displayed in this figure, mass loss due to solvent evaporation, nor the Stokes drag were assumed. It can be seen, that the simulated fiber deposit shape closely follows the experimental results and the elliptical deposit not even changed its eccentricity, but also the tilt of the deposit followed the experimental results. However, it also can be seen that the size of the simulated fiber deposit is not representing reality (at 40Hz forcing function, deposit of only about 20 mm was experimentally obtained as opposed to 80mm from simulation), nor did the simulated fiber develop bending

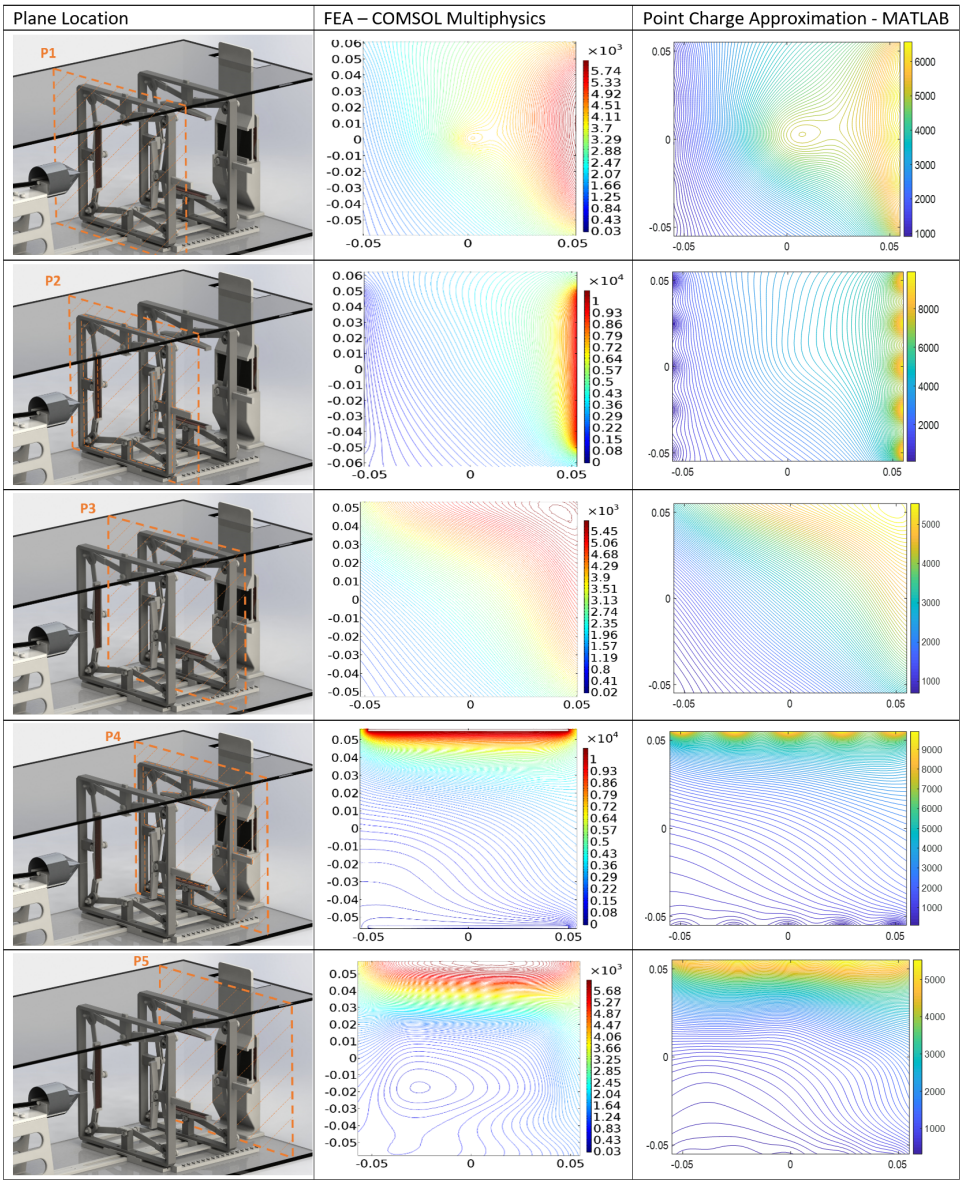

Figure 5.6: Electric potential distribution comparison between FEA analysis and Point charge approximation in Matlab in multiple transverse planes of 2x2 fiber steering electrode setup.

instabilities.

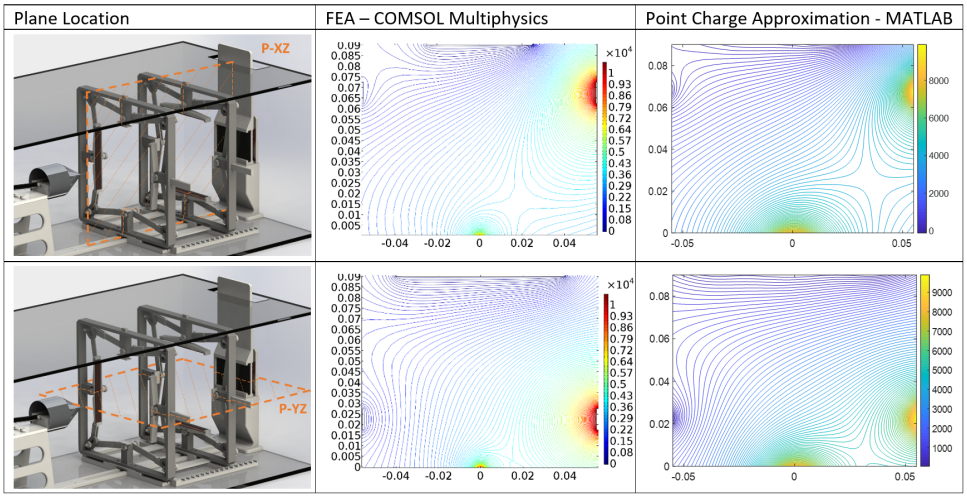

Figure 5.7: Electric potential distribution comparison between FEA analysis and Point charge approximation in Matlab in multiple longitudinal planes of 2x2 fiber steering electrode setup.

For this reason, mass loss due to evaporation and Stokes drag were added, and resulting fiber behavior is described in the following subsection.

5.3.4 Fiber Mass

As the polymeric solution of 5 - 10wt% of PEO in water was used, drying of the fiber has significant impact on the fiber mass loss and it needed to be considered in the model. Based on experimental results described in Fig. 4.19, approximate fiber mass-loss function (as a function of axial coordinate of the device) was constructed and can be seen in Fig. 5.10.

5.3.5 Viscoelasticity of the Fiber

Viscosity of the material is tightly connected to the solvent content in the polymeric jet. As the fiber dries, becomes solid, it looses its viscous properties. Viscosity, resp. structural damping coefficient function was therefore constructed as shown in

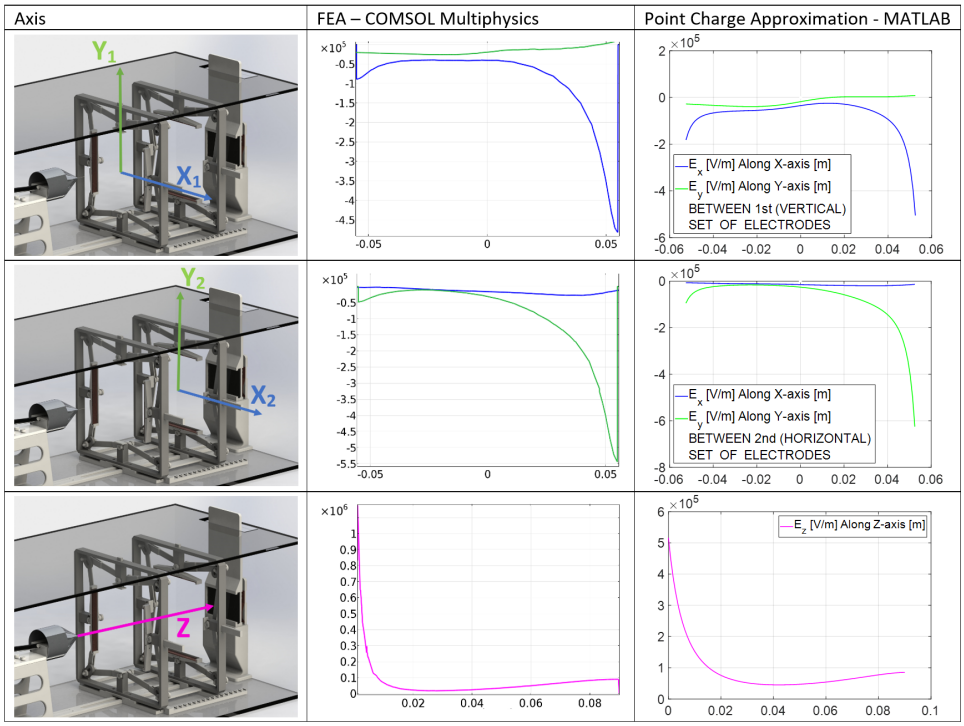

Figure 5.8: Comparison of individual electric field components from FEA and point charge approximation along highlighted axes of the device.

Fig. 5.10.

With implementation of Stokes drag and mass loss due to solvent evaporation, the simulation of fiber extrusion still led to an elliptic deposit, and on top of that started to exhibit the bending instability. However, only one order of the instability was developed, and the fiber deposit still did not match the experimental results in its size. This can be seen in Fig. 5.11, where extrusion at frequency of the forcing function of $f = 40\,Hz$ led to a deposit three times larger than the experimentally obtained deposit. Because the fiber segment length of only L=0.1 mm was used for the simulation result displayed in Fig. 5.11, it was only run to see the developed instability and not the full fiber deposit on the collector electrode. With such fine fiber discretization, simulation of the full fiber deposit would become computation-

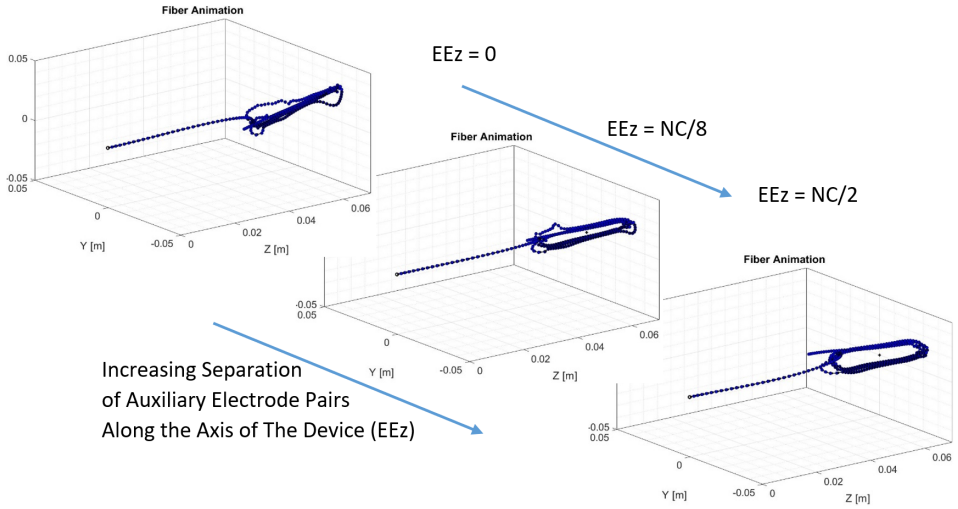

Figure 5.9: Eccentricity of the elliptical deposit as function of the auxiliary electrode separation.

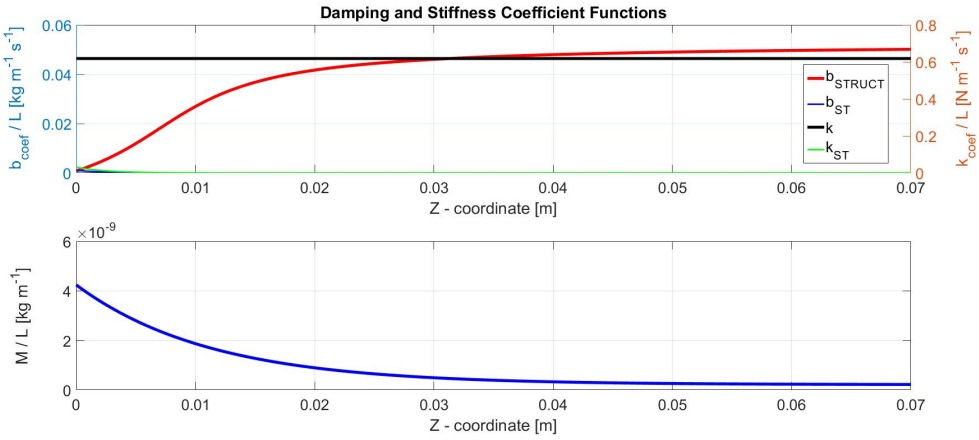

Figure 5.10: Influence of solvent evaporation on mass, damping and stiffness coefficients of the viscoelastic fiber model. These coefficients were built as a function of axial position of the bead inside the device.

ally extremely expensive.

It was experimentally found [8], that electrospun PEO nanofiber leads to smallest electric charge driven instability with loop diameter of about 200 nm. As the Fig. 5.11 shows, bending instability developed in the simulation led to

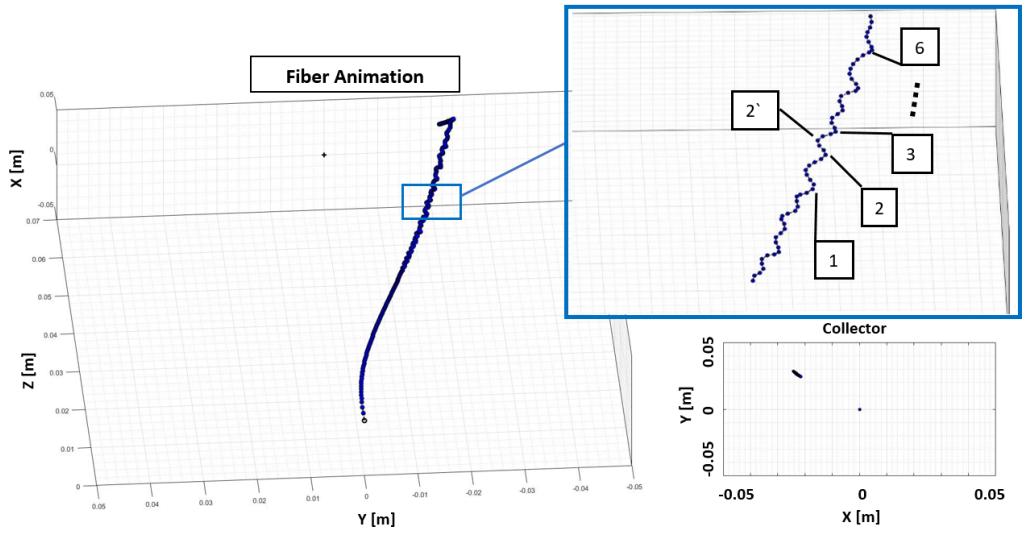

Figure 5.11: Bending instability development on simulated fiber extrusion with use of 2D steering at 40 Hz.

steady state loop size of about 1mm, what suggests, that another order of bending instability should be developed on top of the exhibited one. This is not achievable in the simulation, ast the required fiber discretization would lead to extremly large set of degrees of freedom, resulting in extremly long computational time. For this reason, mass and fiber stiffness were adjusted, to represent the accumulated coiled fiber within the discretized fiber segment. To do this, it was assumed, that individual orders of bending instability lead to the same geometry of the coiled fiber. So if the exhibited order of bending instability of the fiber led to a specific ratio of pitch to diameter of the fiber coiling, the bending instability of higher order that is built on top of the previous one, will have the same pitch to diameter ratio. With this assumption, mass and stiffness coefficient corrections were calculated as described in series of equations Eqn. 5.22 - Eqn. 5.26, and depicted in Fig.5.12.
In the Fig. 5.11, individual turnes of the fiber are numbered, and coordinates of marked points were used to describe helical geometry of the fiber. Pitch of the fiber helix is calculated in Eqn. 5.22, and its diameter in Eqn. 5.23,

$$p = \frac{u_{1,6}}{5\,|u_{1,6}|} \doteq 1.6\,mm \tag{5.22}$$

where $u_{1,6}$ is a position vector between points 1 and 6, and $|u_{1,6}|$ is its size.

$$D = |u_{2',3}| - u_{2',3} \cdot u_{1,6} \doteq 1.4\,mm \tag{5.23}$$

Then the length (and also mass) ratio of helical to straight fiber segment can be expressed as in Eqn. 5.24.

$$\frac{L_{helix}}{L_{straight}} = \frac{\sqrt{(\pi D)^2 + p^2}}{p} \doteq 3 \tag{5.24}$$

To calculate the stiffness coefficient correction, bending stiffness of the straight beem-like segment is compared to a helical spring stiffness as shown in the Fig. 5.12. Axial strain energy of the straight solid fiber segment under non-axial loading is neglected compared to bending strain energy, what leads to a deflection of the tip of the straight segment as described in Eqn. 5.25,

$$\delta_{straight} = \frac{Fl^3}{3EJ} = \frac{64Fl^3}{3E\pi d} \doteq 1.63 \times 10^{16}\frac{F}{E} \tag{5.25}$$

where J is an area moment of inertia of a circular cross-section, d is the fiber diameter, E is Young's modulus and l is the length of the fiber segment. Strain energy of a helical fiber segment is a sum of shear and torsion strain, and leads to the deflection expressed in Eqn. 5.26.

$$\delta_{helical} = \frac{8FC^3}{Gd}\left(1 + \frac{0.5}{C^2}\right) \doteq 1.399 \times 10^{16}\frac{F}{G} \tag{5.26}$$

Here $C = \frac{D}{d} \doteq 769$, as D is the diameter of the helix and d is again the fiber thickness. G is the shear modulus of the PEO. If then deformations of these two fiber segments caused by the same force F are compared, stiffness coefficient ratio of $\frac{k_{straight}}{k_{helical}} \doteq 850$ can be obtained.

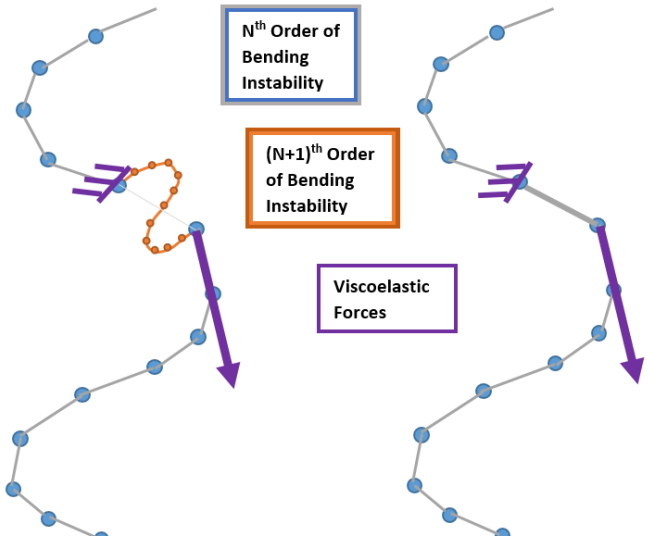

Figure 5.12: Method of addition of an order of bending instability, leading to mass and stiffness coefficient corrections.

With the stiffness coefficient and mass of the fiber correction, to represent looped fiber within the discretized fiber segment, the size of the fiber deposit was not reduced to the size of the experimentally obtained fiber deposit. The reason for this was the high velocity of the fiber, as many researchers modeling the electrospinning process reported [13]. Neither the structural damping nor the Stokes drag were able to reduce the propagation velocity of the fiber. As the fiber propagation is propelled by the electric charges on the fiber moving in the electric field created by the electrodes of the device, an assumption was made, that the electric charge carried by the fiber is in reality lower than measured. The discrepancy between the assumed charge and measured would be caused by the indirect measurement of the electric charge. As the charge was calculated from electric current on the fiber and velocity of propagation of such fiber. In this calculation, it was assumed, that there is no electron flow trough the fiber, and so the measured current is 100% from the electric charge fixed on the fiber, and transported to the collector by the moving fiber.

With reduction of the electric charge carried by the fiber, it became less responsive to the external electric field, and its velocity of propagation decreased. With further tuning of this charge, and Stokes drag coefficient, a match between the experimental and simulated fiber deposit size was achieved, while still keeping the simulated shape of the deposit equal to the experimental one. Simulated size of the deposit as a function of the frequency of the potential function applied to auxiliary electrodes of the device is shown in Fig. 4.13, together with experimental results and results of Kelvin-Voight material model simulations.

A fiber behavior during the extrusion, together with the fiber deposit is shown in Fig. 5.13, together with the material properties and device parameters used in the simulation. The MATLAB code itself can be found in the Appendix A of this work.

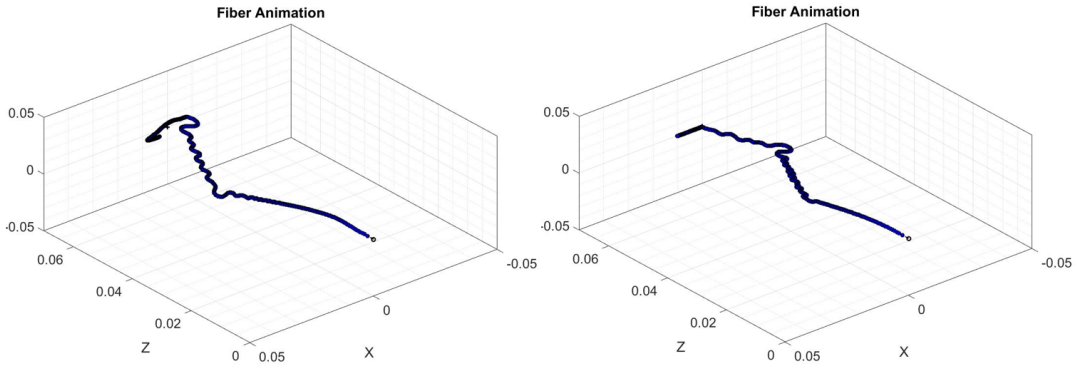

M	2.1206 x 10^{-13}	[kg]	Q	7.4074 x 10^{-13}	[C]
L	1.0000 x 10^{-3}	[m]	NV	8.0000 x 10^{3}	[V]
K	6.1819 x 10^{-4}	[N/m]	EV	0 / 1 x 10^{4}	[V]
b_{STOKES}	4.7937 x 10^{-8}	[kg/s]	f	40	[Hz]
b_{STRUCT}	5.0500 x 10^{-5}	[kg/s]	NC	7.0000 x 10^{-2}	[m]

Figure 5.13: PEO fiber extrusion and deposition simulation results for viscoelastic model of the fiber during an electrospinning process, with electrodynamic steering. Left: with 2D electrodynamic fiber steering; Right: with 1D fiber steering. Table below the figure lists the device parameters and initial values of the material properties. Time/position dependent material properties were changing according to functions shown in Fig. 5.10

Comparing performance of the two developed models, both are capable of accurate fiber deposit shape and size prediction. The viscoelastic model has on top of

that capability to predict the fiber extrusion and bending instability development as the fiber propagates towards the collector electrode. This, however, is very costly in terms of the computational time, as the system of stiff nonlinear ODEs grows with the growing fiber. This trade-off analysis can be seen in Tab. 5.14, comparing these two models.

Material Model	Prediction Capability				Computation Time	
	Extrusion		Deposition			
	Propagation	Instability	Pattern	Size	Fast	Slow
Kelvin-Voigt	✗	✗	✓	✓	✓	✗
Maxwell	✓	✓	✓	✓	✗	✓

Figure 5.14: Trade-off analysis of the two developed mathematical models of electrospun nanofiber

Chapter 6

Applications

In this section, application of developed electrodynamic fiber steering technique in preparation of tubular structure composed of aligned electrospun polymer nanofibers is described. As the application suggests, the flat static collector electrode was replaced by a cylindrical collector electrode of diameter of desired tubular fibrous structure. For both, artificial nerve graft and expandable coronary drug-eluting stent structures, tube constructed of uni-axially oriented fibers is desired. This can be achieved with application of 1D electrodynamic steering described in section 4.1. The fiber, forced to oscillate in the horizontal plane, was collected on a slowly rotating tubular substrate in case of the expendable catheter application, or in between two slowly rotating rods in case of the nerve graft.

6.1 Expandable Catheter

As previously stated, axially oriented fiber is desirable for such application, as it would potentially support large radial strains of such structure. With the radial expansion of the tubular catheter, these fibers would only be partially pulled apart but still retain the tubular structure because of numerous layers of the fiber, that would prevent the wall from being structurally compromised. With conventional fiber collection on top of the spinning mandrel or drum, fiber coiled around the tubular substrate would quickly reach its fracture point if the tube was radially inflated. This hypothesis was tested, and results are discussed in this chapter. Several electrospinning setups, employing the 1D electrodynamic fiber steering -

leading to axially oriented fibers, were tested from the point of view of resulting structure quality and production efficiency. Individual setups can be seen in Fig. 6.1

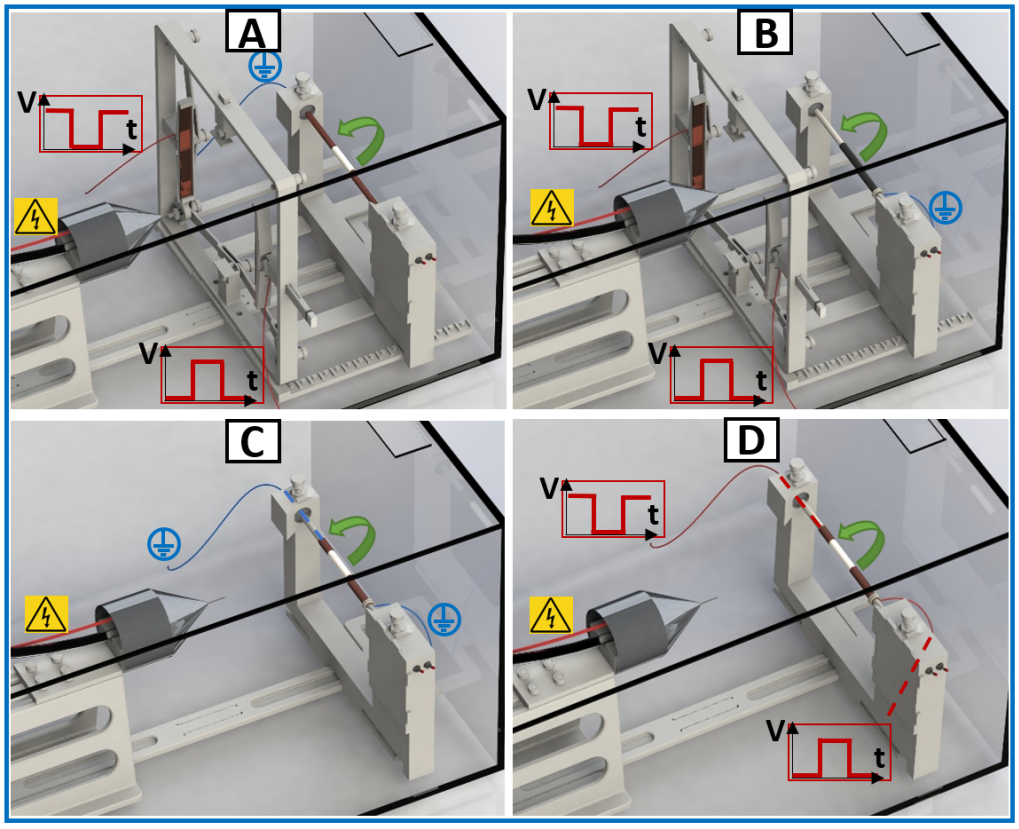

Figure 6.1: Four different electrospinning setups leading to axial fiber deposition along a tubular substrate, examined from fiber alignment and extrusion efficiency point of view.

6.1.1 Experimental Setup

A) Continuous, horizontally oriented, rotating, grounded rod, with the latex substrate used as a collector, and one set of vertically oriented auxiliary electrodes to steer the fiber in the horizontal plane. The fiber is therefore forced to deposit alternatively on both sides of the latex tube, what leads to the fiber collection on

top of the electrically non-conductive substrate as well. Frequency of the square potential function, applied to the auxiliary electrodes, must lie within a specific frequency interval, which is (for given polymeric solution) a function of electric potentials applied to individual electrodes, distances between them and length of the desired tubular structure. Higher limit of this interval is given by the threshold frequency, at which the fiber still has time to travel between the individual exposed ends of the grounded rod, and lower limit is the frequency, at which the fiber could reach the auxiliary electrode. For the larger lengths of the catheter structures, this frequency range becomes very narrow, and it becomes unpractical.

B) Primary problem with electrospun fiber collection on a latex substrate is, that it is electrically non-conductive. This is because the collected electric charge, contained by the fiber, builds up on top of such substrate and eventually starts to repel the incoming fiber, or eventually stops the electrospinning, as the electric field that draws the fiber diminishes beneath the threshold value. For this reason, coating of the latex substrate by an electrically conductive material would eliminate its charging, and the length of the fiber deposit then dos not have to be unnecessarily long, just to bridge the conductive parts of the collector, as it was in previous case. This would lead to higher fiber use efficiency ale less process limitations.
For these reasons, latex tubular substrate was painted with carbon paint and the fiber was deposited along its axis using 1D steering method, as in previous case. The carbon paint, however, created a hard, brittle shell on top of the latex tube, which started to crack already during its solidification and failed immediately as was attempted to be inflated. With loss of the structural integrity, it started to fall apart and not only polluted the fiber deposit, but also torn it to pieces. This effect could possibly be prevented with thin film coating (sputtering), where only several nm of metal would be deposited on top of the latex substrate, but consequently, this film would be impossible to remove without damaging the fiber deposit. In Fig. 6.2,

fiber deposit on top of the carbon painted latex tube is shown, where the cracks in the paint are clearly visible

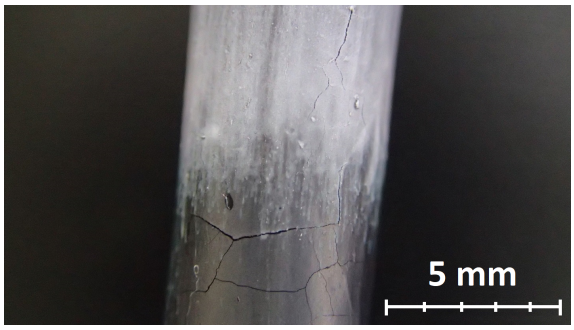

Figure 6.2: Axially oriented polymer fiber deposited on top of the carbon-painted latex tube. Cracks in the carbon paint developed during its drying.

C) A rod with two conductive, individually grounded ends and insulating central piece, with no additional steering was used, as described in [21]. This method relies on the electric charge accumulation on the side of the rod where fiber is being deposited, what eventually cases it to jump to its other side. Such bridging of the two conductive sides of the rod then leads to a fiber deposition on top of the non-conductive part, or installed latex substrate. While this method is very simple, as it does not require any additional fiber steering, it is very slow in terms of the tube production. It leads to massive fiber deposits on both sides of the conductive parts, while depositing very little fiber in between them.

D) The last experimental setup is based on the two previous setups, where an electrically conductive rod, with non-conductive material or gap in its center is used as a collector electrode. Electrodynamic steering is not implemented through the use of auxiliary electrodes, but with the square potential function applied directly to the conductive sides of the collector electrode. This way the fiber deposition switching between individual ends of the collector is driven by the frequency of the

applied potential function. This method proved itself to be the most effective in terms of the fiber quality, amount of the fiber deposited on the latex substrate and predictability/repeatability. For this reason, this method was used for the sample production described in the following section of this work.

6.1.2 Experimental Procedure

At this, initial, stage of work, electrospun polymer structure was not removed from the substrate before the testing. For this reason, flexible tubular substrate was desirable, and so latex was selected. Latex tubes of various diameters were then dip-molded, vulcanized and stored in a clean environment, until used as substrate for the inflatable electrospun catheter. A layer of PEO fibers was electrospun on top of the substrate, to the point, when substrate was fully covered. Production method D, with 1D electrodynamic fiber steering, described in the previous subsection(6.1.1) was used for the fiber deposition. Square electric potential functions applied to individual sides of the slowly rotating rod were of peak-to-peak amplitude of 10 kV and mean of 2 kV. A shift of the potential function mean from 5 kV (as described in 1D steering introduction - section 4.1) to 2 kV was done in order to establish sufficient axial electric field component in the device, and so to stabilize the fiber extrusion. When original 5 kV mean of the potential function was kept, with increasing frequency of this function, electrospinning process was terminated.

Once the sufficient amount of PEO nanofibers was collected on top of the latex substrate, the tube was carefully removed from the collector rod. To be able to investigate the fibers after the tubes inflation by SEM microscope, the tube could not have been inflated by compressible air, as the de-pressurizing of the SEM chamber would cause additional expansion and possibly rupture of the tube. Neither it could have been inflated with liquid, as this would lead to a

SEM damage, if the tube accidentally ruptured inside the chamber. For this reason, it was inflated by molten paraffin, which solidified after the inflation and therefore allowed for SEM investigation of the collected fiber. Fig. 6.3 shows the collected fibers both before, and after the tube inflation, where its diameter increased approximately by 50% (from 8.3 mm to 12 mm) . From the SEM images of un-inflated and inflated tube, it can be seen, that fibers on the un-inflated substrate have dominant axial orientation and are almost fully straightened. As expected, percentage of the axially oriented fibers, and also fiber straightness on the inflated substrate is higher, what corresponds to the stretch of the fiber introduced by the substrate inflation. From comparison of the two samples, it also can be seen, that the fiber density of inflated tube is significantly lower than of un-inflated. Drop in the fiber density is expected, as the surface area of the tube is increased with inflation, but not in such dramatic extent. This excessive fiber density decrease can be possibly attributed to the fiber loss due to fiber rupture.

The tube inflation process did not result only in increase of diameter of the tube, but also in it‘s elongation. On top of that, the shape of the tube was changed from cylinder to the barrel-like shape. This would eventually lead do an additional strain on the fibers on top of such substrate. Even perfectly axially aligned fibers would be stretched, possibly exceeding the breaking point. To reduce the risk of a fiber rupture, partially buckled fiber collection might be desirable. To control the straightness of the fiber in such process, angular velocity of the substrate during the fiber collection needs to be changed. At lower velocity, the fiber is more axially oriented, but less straight. As the angular velocity of the substrate is increased, fiber is more stretched, but at the same time starts to coil around the substrate, and so deviate from the axial orientation. The straightness of the fiber as a response to change of the angular velocity of the substrate can be seen in Fig. 6.4.

Inflatable catheter application requires a stand-alone tube composed of the

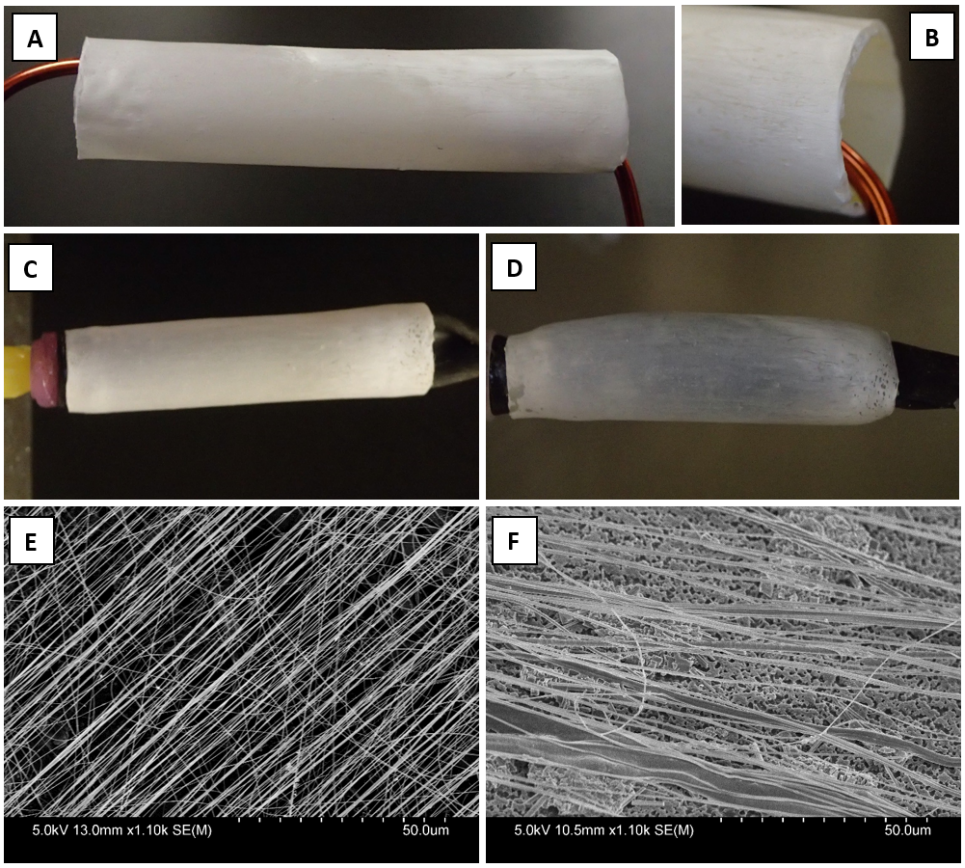

Figure 6.3: A, B, C, E - Tubular structure composed of axially oriented straigth PEO nanofibers on latex substrate before the inflation. D, F - After the inflation by molten paraffin (diameter increase by 50%)

polymer nanofiber, as opposed to fibers on a irremovable substrate. Production capability of such tube was examined, and such tube was achieved with above described deposition method, and a thick layer deposition. The resulting structure had sufficient structural stability to be then removed from the substrate and examined. Images of such tube are shown in Fig. 6.5, where from SEM images, it can be seen the primary orientation of the fiber but also thet the fiber was not completely dry at the time of the deposition, resulting in partially merged fibers. To avoid this, spinning distance simply needed to be increased, what would provide

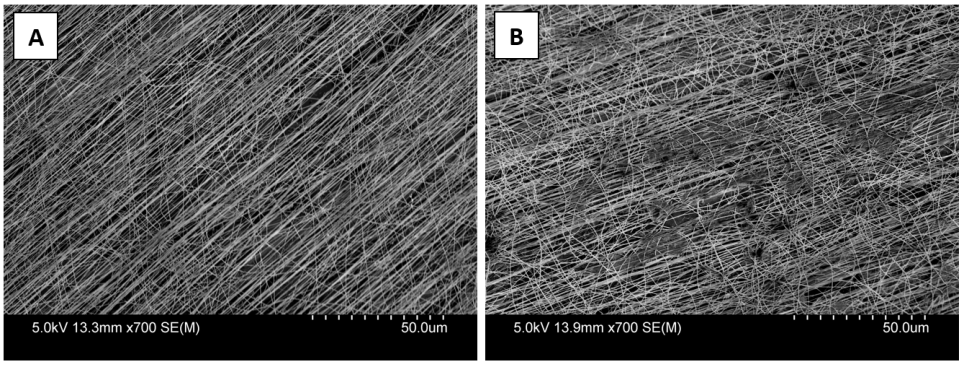

Figure 6.4: Fiber deposit along the axis of rotating tubular substrate of different frequency. A - $f = 1.18\,Hz$ and B - $f = 0.15\,Hz$

additional drying time to the fiber before its deposition.

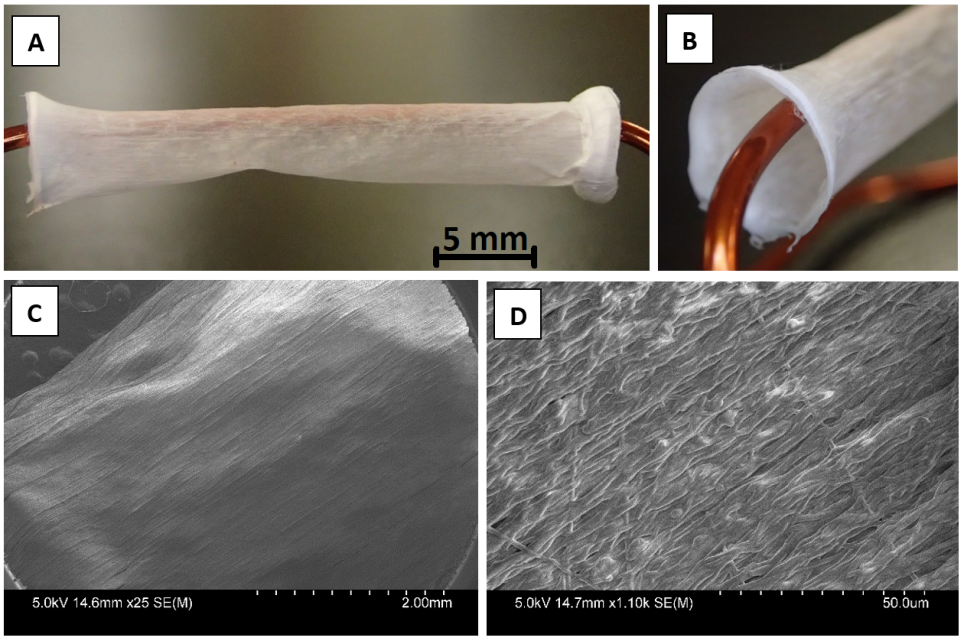

Figure 6.5: Images of the stand alone PEO nanofiber formed tubular structure, with axially oriented fibers. Orientation of the fiber is visible in SEM images(C, D), where D also suggests wet fiber deposit

.

6.2 Nerve Graft

As described in section 1.3, highly aligned parallel fibers are required for the nerve graft application. It is not enough for the fibers to create a tubular structure as was described in the inflatable catheter application. Here, for the directional support of the regenerating nerve cell, essentially a full rod needs to be created. This means, parallel straight fibers must be collected with no underlying substrate, and form a structurally stable rod, which can be manipulated without a fiber damage. For such production process, similar method as for the inflatable catheter was used. A collector device consisting of two thin rods separated by a gap of length L, rotating with the same RPM, and individually connected to two square potential functions in anti-phase was used. Electrospinning setup with such collector device is shown in Fig. 6.6.

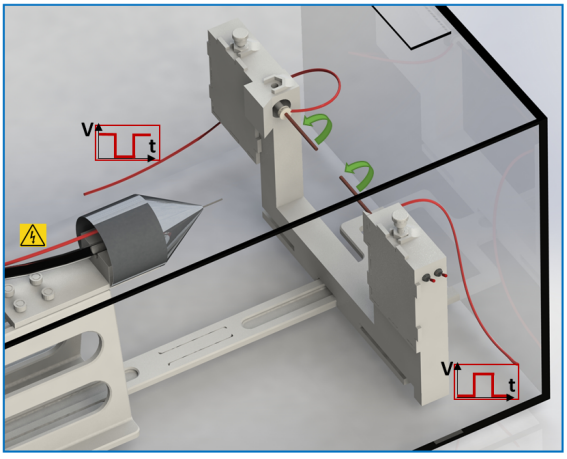

Figure 6.6: Electrospinning setup with 1D electrodynamic steering incorporated in the fiber collector, leading to collection of solid cylindrical deposit with axially oriented fibers

When the fiber extrusion is initiated, fiber is attracted to the rod with low potential and so the oscillatory movement of the fiber is enforced. Such movement between these individual segments of the collector, again bridges these segments.

If the overhang fibers were completely straight, a tube of inner diameter equal to the diameter of the two rods would be created. However, as these fibers are not perfectly straight, what can be seen from Fig. 6.4, this process would lead to a full, not tubular, structure. This is as if the inner wall of the tube collapsed inwards and filled the inner space of the tube. This would be true only for relatively small diameter of used collector rods. With increasing diameter, a cavity inside the deposited overhang fiber would be formed. It is also extremely important, that the rods are perfectly axially aligned, and that their angular velocity is equal. If these conditions are not satisfied, resulting structure would exhibit following defects.
Axial miss-alignment of collection rods:

- Fiber collected in between such rods would undergo repetitive stretch, which could eventually lead to deformed or ruptured fibers.

Different angular velocity of collection rods:

- Difference in RPM of these two rods, would result in twisting of the deposited fiber. This would again lead to a fiber deformation, change of axial fiber alignment and eventually to a fiber damage and ruptured structure.

Fig. 6.7 shows successfully collected structure, and Fig. 6.8 an SEM image of such structure, coated by 7 nm of gold coating to eliminate sample charging. It can be seen, that the structure is indeed composed of well aligned fibers. The thinner fibers visible in the deposit, having orientation mostly perpendicular to the main fiber deposit, are result of a fiber branching, or splaying. This was previously described by [13], and is most probably a consequence of locally decreased surface tension on the extruded polymer jet, what leads to the creation of thin fiber branch originating from this location. improvement of the fiber deposit in this term can be achieved by increasing the surface tension of the polymeric solution. This could be often done by even small increase of the PEO concentration in the solution, or by

changing chemical composition of the polymeric solution (addition of salt, change of solvent or polymer).

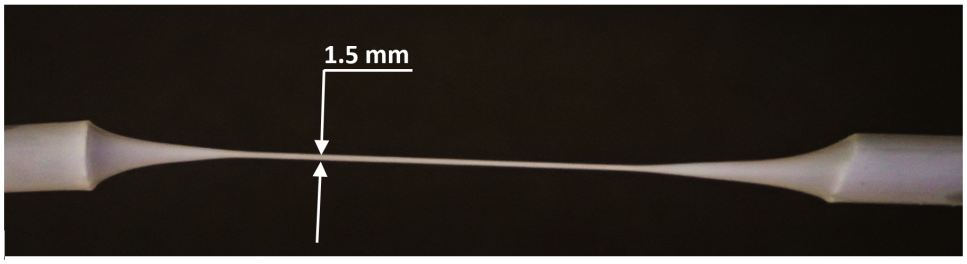

Figure 6.7: Image of solid cylindrical structure for nerve graft application, composed of axially aligned fibers

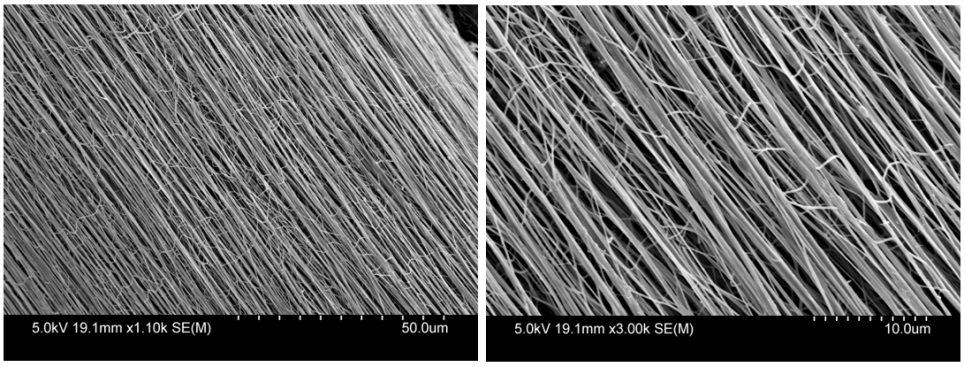

Figure 6.8: SEM Images of solid cylindrical structure for nerve graft application, composed of axially aligned fibers

Chapter 7

Conclusions & Discussion

Electrospinning is a versatile nanofiber production technique, which has attracted a widespread interest over the recent years. This is mostly because of wide variety of nanofiber applications, predominantly in biomedical engineering. In this work, electrospinning working parameters, fiber focusing and steering, modeling and applications were investigated and described. Following conclusions were drawn for each section of this work.

7.1 Conclusions

7.1.1 Working Parameters

Material properties of a polymeric solution play crucial role for the fiber extrusion. Solution of 5 wt% of PEO in DiH_2O, was found to be ideal for the electrospinning. Lowering the PEO content decreases surface tension of the solution to the point when it is no longer able to support the fiber extrusion, and it turns into electrospraying. Higher than ideal polymeric concentration leads to premature fiber solidification, what leads to beaded fiber or nozzle clogging. Impact of nozzle voltage on the Taylor cone stability and consequently on deposited fiber quality was experimentally demonstrated. For the fiber extruded from 5 wt% of PEO in DiH_2O solution, with nozzle to collector distance of NC=80 mm, ideal nozzle voltage was found to be 8 kV. These electrospinning parameters leads to a continuous fiber extrusion of constant diameter of $250 \pm 30\,nm$ and dry fiber deposition on the

collector electrode. Collector electrode resistivity was found to have significant impact on sharpness of the fiber deposit, as it influences the electric charge dissipation from collected fibers. Slow charge dissipation causes the deposition region to drift, what diminishes the effect of fiber focusing or steering. To further increase the focusing/steering capability, electric conductivity of the solution can be increased by addition of charge carriers into the polymeric solution. However, responsiveness of polymer fiber, extruded from LiBr enriched solution, to external electric field showed no measurable improvement. Not only the fiber steering capabilities were not significantly improved, but at LiBr concentration of 0.2 wt% the fiber started to loose integrity, and at 0.5 wt% led only to electrospraying.

7.1.2 Electrostatic Focusing

Property of the fiber, that it carries charge, was used to exert Coulomb forces on such fiber, from the external electric field. Electrostatic focusing was introduced to the electrospinning device by a single pair of auxiliary electrodes. Most effective focusing setup,found experimentally, led to the smallest circular fiber deposit of area $A = 40\,mm^2$ (Fig. 3.7). Electrostatic focusing capabilities were found to be significantly limited by the requirement to maintain non-negative axial electric field component in the electrospinning device, with minimum electric field at the tip of the nozzle of $E_{zmin} = 1.6 \times 10^6\,[v/m]$. With lower electric field in the proximity to the nozzle, fiber extrusion would not be initiated. With vanishing axial electric field component in the electrospinning device, fiber is partially or fully diverted from its path to the collector electrode, or the fiber extrusion is terminated. With intentionally unstable fiber extrusion and partial loss of the fiber due to vanishing axial electric field, narrow line-like deposit was achieved (Fig. 3.9). Even though the fiber deposit is stretched into a linear deposit, the fiber is deposited randomly (with no alignment) on microscopic level. To actively control the fiber alignment,

electrodynamic fiber steering needs to be implemented.

7.1.3 Electrodynamic Steering

In electrodynamic fiber steering, AC voltage (with mean lower than NV) was applied to the auxiliary electrodes of the device. This way, negative axial electric field component and resulting fiber reversion or extrusion termination were prevented. A positive electric field path connecting the nozzle and collector was then maintained at all times. Changing this path in time, steers the fiber and forces it to deposit on the collector electrode in a pattern defined by this path. This creates a requirement, that frequency of the potential function generating the steering external electric field must be of such frequency, that the fiber will never reach a surface of the auxiliary electrode. Square potential functions in anti-phase, used for such steering, were selected to maximize the potential difference between individual auxiliary electrodes at any time, and so to maximize lateral steering forces acting on the charged fiber. It was shown, that by changing the number and positions of auxiliary electrodes within the electrospinning device, shape and size of the fiber deposit can be controlled. In this work, linear (1D) and planar (2D) fiber deposition patterns on a flat static collector electrode were described. Length of the linear deposit achieved with 1D steering, as a function of frequency of potential function applied to auxiliary electrodes was found to be $L_{1D} = 4.832\, f^{-1.43}\, [m]$ on interval $f = [40\ \ 200]\, Hz$. Length of the semi-major axis of 2D steered elliptical deposit as a function of frequency was found to be $L_{2D} = 1.45\, f^{-1.332}\, [m]$, on the same frequency range as for 1D steering. Axial separation of the two electrode pairs in 2D steering defines eccentricity of such elliptical deposit. Larger the separation, smaller the eccentricity. Circular deposit, however, was not achieved. Shift of the elliptical deposit along the semi-major axis can be controlled by pulse width modulation (PWM) of the potential functions, and the orientation of an elliptical deposit is

defined by physical position, resp. orientation of the auxiliary electrodes. Further addition of auxiliary electrodes to the electrospinning device did not improve the fiber alignment or straightness, nor led to new deposition patterns. The fiber properties were found to be independent of the fiber steering, as the diameter and morphology of the fiber was found to be the same for unsteered, 1D steered and 2D steered fiber at various frequencies of the forcing function.

7.1.4 Mathematical Model

Two mathematical models of the electrospinning were built. Kelvin-Voigt fiber model, assuming a solid fiber with no net mass accumulation inside the device, which can predict the fiber deposit shape and size, and is computationally very fast. However, it can not predict the fiber propagation, and the fiber can not develop bending instability. Second, viscoelastic (Maxwell material) fiber model, predicts the fiber extrusion, propagation and deposition, but because of its size, it is computationally extremely slow and not feasible for the fiber deposit prediction. This model considers the fiber growth, mass reduction and viscosity increase due to solvent evaporation, surface tension of the Taylor cone, charge dissipation after the collection on collector electrode, Coulomb repulsion between individual beads of the fiber, and external Coulomb forces from the electric field generated by auxiliary electrodes. To accurately compute external electric field, point charge approximation was built and implemented into the model. Accuracy of such approximated electric field distribution was demonstrated by comparison to FEA analysis results. Simulated fiber develops up to two orders of bending instabilities but did not develop higher orders, possibly because of the fiber discretization. For this reason, mass and stiffness coefficient corrections were applied, to adjust for the missing mass, accumulated in the highest order of bending instability. (described by Reneker [8], with fiber loops of $D = 200\,\mu m$ in diameter). Fiber bending stiffness

and bending damping were not considered in neither of the models, what resulted in a need of air drag increase (720x in Kelvin-Voigt model and 40x in Maxwell material model), to decrease the lateral movement of the fiber. In addition to that, to match the simulated and experimental fiber deposit sizes, linear charge density of the viscoelastic fiber was tuned to $\lambda_q = 7.4 \times 10^{-10}\, C/m$, which is two orders of magnitude lower then the measured value given in Eq. 5.14. This difference in the charge carried by the fiber was presumably caused by an incorrect assumption, that there is no charge moving trough the extruded fiber.

7.1.5 Applications

Application of the developed electrodynamic fiber steering was demonstrated on preparation of two different cylindrical fibrous structures, composed of axially oriented fibers. For such application, cylindrical substrate or collector electrode was used. It was also found, that it was more efficient to move the electrodynamic fiber steering from the auxiliary electrodes, to the collector level, as then the unintended collection on these auxiliary electrodes was avoided. This also allowed to collect the fiber on electrically non-conductive substrate like latex, placed in between the two segments of the collector. Utilizing such method, hollow tubular structure, composed of axially oriented polymer fibers was prepared. As required for the coronary drug-eluting stent application, such structure needs to allow for radial expansion without being structurally compromised. After expansion of the sample, it was found that even though the fibers were initially axially oriented, already a 50% increase in diameter caused a noticeable fiber loss in the structure. This is possibly a consequence of problematic inflation of the tube, which led to both lateral and radial expansion, and so to additional strain of the deposited fibers. The same fiber steering method without use of a substrate led to successful preparation of a solid cylindrical structure, containing axially oriented straight fibers. For a

nerve graft application, straightness of the fiber, together with its alignment is crucial to provide a directional support for the regenerating nerve. A structure of such properties was prepared utilizing the 1D electrodynamic steering, in combination with a pair of low diameter, slowly rotating (1.15Hz) co-axially organized collector rods. Extruded fiber was then deposited in between these rods, creating a solid cylindrical structure. Diameter of such structure is given by the deposition time and diameter of the two rods. Examined sample was of diameter of D=1.5 mm.

7.2 Future Work

An initial examination of use of Poly(lactic acid) (PLA) solution in binary solvents of Acetone + Chloroform and Acetone + DMF in electrospinning device with electrodynamic focusing was performed, and showed promising results in terms of higher structural stability and flexibility than PEO structures. However, the extrusion process needs to be improved, as fast evaporation of the solvent and consecutive nozzle clogging prevented from continuous fiber extrusion. Also, extruded PLA fibers were not as responsive to the electrodynamic steering as the PEO fibers were. Therefore, increase of conductivity of PLA solution should be considered.

A reliable technique for controlled tubular substrate inflation will need to be developed, to be able to inflate low diameter tubes and to prevent the fiber damage.

Appendix A

Appendix A

A.1 Matlab Code for Kelvin-Voight material model simulation

```
1
2  clear all, clc
3
4  %% Design Device Parameters
5  Noz_Col=0.06;       %[m]
6  N=0.0012;               %Nozzle Diameter [m]
7  Noz_el=Noz_Col/2;
8
9  %experimental results to be matched
10 parameters=['Nozzle_to_Collector=',num2str(Noz_Col),'[m]','  ...
11 Nozzle_to_Electrode=',num2str(Noz_el),'[m]','  ...
12 Electrode_Voltage=10/0.6 [kV]'];
13 exp_freq=[40 45 50  55  60  65  70  75  80  ...
14 85  90  95  100 110 120 140 160 180 200 220];
15 exp_L=1e-3*[24.49 20.2 16.995 16.4 14.655 11.865 10.585 9.435 ...
16 9.845 8.685 9.005 7.885 5.98 5.56 5.37 4.55 4.53 3.085 ...
      2.746666667 2.13];
17
18 %%    CALCULATION
19 L=Noz_el/2;
20 d=(3e-7);                %Fiber diameter 1e-7=100nm
21 ro=1e3;                   %water density(as only 5% of PEO )
```

```
22 M=L*pi*d^2/4*ro;
23 ni=(1.983e-5);          %dynamic viscosity
24 %Stokes drag
25 c=3*pi*ni*(1.5*d^2*L)^(1/3)*1.3*720;
26 c4=c;            %increased drag on last beed-on collector
27  E=7e9;      %  Young moduli of individual PEO fibres
28 k=E*3.14*d^2/4/L;% stiffness coefficient
29 b=1e-5;      % Structural damping coefficient
30 I=1e-7;      % El current measurement
31 v=4.8;  %2.25;  % Fiber velocity measurement
32 qq=I/v*L;        % El charge
33 ke=8.9875517873681764e9;
34
35 %name corrections
36     L0=L; m=M;
37
38 %% Electric field
39
40 %FOR Noz_El=35, NV=10kV
41 AK1=1.2e6;       %beed between the nozzle and trap
42 AINT1=-5.2e4;
43 AK2=-2.5e6;      %beed in the trap
44 AINT2=-6.5e4;
45 AK3=-1.3e6;      %beed between the trap and collector
46 AINT3=-3.8e4;
47
48 % %FOR Noz_El=25, NV=8kV
49 % AK1=1e6;       %beed between the nozzle and trap
50 % AINT1=-0.55e5;
51 % AK2=-2e6; %beed in the trap
52 % AINT2=-0.7e5;
53 % AK3=-1.2e6;   %beed between the trap and collector
54 % AINT3=-0.4e5;
55
```

```
56 f=40;
57 omega=2*pi*f;
58 alpha= k*L/M;
59 gamma=ke*qq^2/M;
60
61 %% Numerical solu
62
63 % steady state spring length
64 leq=roots([1 -Noz_Col/4 0 -k*ke*qq^2]);
65 L=leq(1);
66 % ICs
67 z=[Noz_Col/4 Noz_el 3/4*Noz_Col Noz_Col];
68 x0=[-N/2 0 -N/2 0 -N/2 0 -N/2 0 -N/2 0 -N/2 0 -N/2 0 -N/2 0];
69 xf=-N/2;  yf=-N/2;  zf=0;
70 t_step=0.00001;
71 T_max=0.1;
72
73 %ODE options
74 opts = odeset('RelTol',1e-9,'AbsTol',1e-9);
75 cycle=5;
76 increment=20;
77 f=40:increment:cycle*increment+40+100;
78   for ii=1:length(f)
79
80     omega=2*pi*f(ii);
81   % forcingfunction=1    cos
82     [t1,x1]=ode15s(@(t,x) ...
          single_fib1(t,x,z,k,ke,qq,m,c,L,omega,xf,yf,...
83 zf,AK1,AINT1,AK2,AINT2,AK3,AINT3,b,c4),0:t_step:T_max,x0,opts);
84         xmax_cos_tr(iii,ii)=max(x1(:,5))-min(x1(:,5));
85         xmax_cos_col(iii,ii)=max(x1(:,13))-min(x1(:,13));
86   % forcingfunction=2    square
87     [t2,x2]=ode15s(@(t,x) ...
          single_fib2(t,x,z,k,ke,qq,m,c,L,omega,xf,yf,...
```

```
zf,AK1,AINT1,AK2,AINT2,AK3,AINT3,b,c4),0:t_step:T_max,x0,opts);
        xmax_sq_tr(iii,ii)=max(x2(:,5))-min(x2(:,5));
        xmax_sq_col(iii,ii)=max(x2(:,13))-min(x2(:,13));

%% plot

    scrsz=[1 1 1600 900];

    if ii==1
        %plot device layout parameteters

fig2=figure('OuterPosition',[1 440 820 125],'Color',[1 1 1]);
txt4 = uicontrol('Style','text',...
'Position',[10 10 800 ...
   20],'FontSize',[12],'HorizontalAlignment','left',...
'String',parameters);

        %plot material and field parameteters
props1=['Fiber_diam=',num2str(d),'[m]',' E=',num2str(E),'[Pa]',' ...
k(depends on d,E)=',num2str(k),'[Pa*m]','     ...
m(depends on d)=',num2str(M),'[kg]'];
props2=['Fiber_Velocity=',num2str(v), ' [m/s]','    ...
Fiber_Charge(depends on v)=',num2str(qq), ' [C]','    ...
b(fiber damping)=',num2str(b), ' [[N*s/m]]','      ...
c(depends on d)=',num2str(c), ' [N*s/m]'];
fig3=figure('OuterPosition',[1 440 1220 150],'Color',[1 1 1]);
txt5 = uicontrol('Style','text',...
'Position',[10 35 1200 ...
   20],'FontSize',[12],'HorizontalAlignment','left',...
'String',props1);
txt6 = uicontrol('Style','text',...
'Position',[10 10 1200 ...
   20],'FontSize',[12],'HorizontalAlignment','left',...
'String',props2);
```

```
119
120      end
121    end
122
123  fig4=figure('OuterPosition',[1 40 scrsz(3) ...
         scrsz(4)-40],'Color',[1 1 1]);
124  loglog(exp_freq,exp_L,'-r',f,xmax_cos_col(iii,:),'-b',f,...
125  xmax_sq_col(iii,:),'-k',f,xmax_cos_tr(iii,:),'--b',f,...
126  xmax_sq_tr(iii,:),'--k'),
127  xlabel('Frequency[Hz]','FontSize',12),ylabel('Amplitude ...
         [m]','FontSize',12)
128
129  fig5=figure('OuterPosition',[1 40 scrsz(3) ...
         scrsz(4)-40],'Color',[1 1 1]);
130  interp=4.832*[40 220].^(-1.43);
131  loglog(exp_freq,exp_L,'or',f,xmax_cos_col(iii,:),'-b',f,...
132  xmax_sq_col(iii,:),'-k'),
133  xlabel('Frequency[Hz]','FontSize',12),ylabel('Amplitude ...
         [m]','FontSize',12),
134  hold on, loglog([40 220],interp,'--','Color',[1 0.5 0.5]);
135
136
137  %% fun
138  function xp=single_fib1(t,x,z,k,ke,qq,m,c,L,omega,xf,yf,zf,...
139  AK1,AINT1,AK2,AINT2,AK3,AINT3,b,c4)
140  % Distances between beads
141  L_1f=sqrt((x(1)-xf)^2+(x(3)-yf)^2+(z(1)-zf)^2);
142  L_2f=sqrt((x(5)-xf)^2+(x(7)-yf)^2+(z(2)-zf)^2);
143  L_3f=sqrt((x(9)-xf)^2+(x(11)-yf)^2+(z(3)-zf)^2);
144  L_4f=sqrt((x(13)-xf)^2+(x(15)-yf)^2+(z(4)-zf)^2);
145  L_12=sqrt((x(5)-x(1))^2+(x(7)-x(3))^2+(z(2)-z(1))^2);
146  L_13=sqrt((x(9)-x(1))^2+(x(11)-x(3))^2+(z(3)-z(1))^2);
147  L_14=sqrt((x(13)-x(1))^2+(x(15)-x(3))^2+(z(4)-z(1))^2);
148  L_23=sqrt((x(9)-x(5))^2+(x(11)-x(7))^2+(z(3)-z(2))^2);
```

```
149 L_24=sqrt((x(13)-x(5))^2+(x(15)-x(7))^2+(z(4)-z(2))^2);
150 L_34=sqrt((x(13)-x(9))^2+(x(15)-x(11))^2+(z(4)-z(3))^2);
151
152 % Bead velocities
153 v_1f=(x(3)-yf)*x(4)+(x(1)-xf)*(x(2));
154 v_12=(x(7)-x(3))*(x(8)-x(4))+(x(5)-x(1))*(x(6)-x(2));
155 v_23=(x(11)-x(7))*(x(12)-x(8))+(x(9)-x(5))*(x(10)-x(6));
156 v_34=(x(15)-x(11))*(x(16)-x(12))+(x(13)-x(9))*(x(14)-x(10));
157
158 % State matrix
159 xp = [x(2) ;    k/m*(x(5)-x(1))*(1-L/L_12)+b/m*(x(5)-...
160
161 x(1))*(v_12/L_12^2)-c/m*x(2)-k/m*(x(1)-xf)*(1-L/L_1f)-...
162 b/m*(x(1)-xf)*(v_1f/L_1f^2)+ke/m*qq^2*(x(1)-xf)/L_1f^3-...
163 ke/m*qq^2*(x(5)-x(1))/L_12^3-ke/m*qq^2*(x(9)-x(1))/L_13^3-...
164 ke/m*qq^2*(x(13)-x(1))/L_14^3+qq/m*(AK1*x(1)+AINT1*cos(omega*t));...
165
166 x(4) ;    ke/m*qq^2*(x(3)-yf)/L_1f^3-c/m*x(4)-...
167 k/m*(x(3)-yf)*(1-L/L_1f)+k/m*(x(7)-x(3))*(1-L/L_12)-...
168 b/m*(x(3)-yf)*(v_1f/L_1f^2)+b/m*(x(7)-x(3))*(v_12/L_12^2)-...
169 ke/m*qq^2*(x(7)-x(3))/L_12^3-ke/m*qq^2*(x(11)-x(3))/L_13^3-...
170 ke/m*qq^2*(x(15)-x(3))/L_14^3;...
171
172 x(6) ;    ke/m*qq^2*(x(5)-x(1))/L_12^3-c/m*x(6)-...
173 k/m*(x(5)-x(1))*(1-L/L_12)-b/m*(x(5)-x(1))*(v_12/L_12^2)+...
174 ke/m*qq^2*(x(5)-xf)/L_2f^3-ke/m*qq^2*(x(9)-x(5))/L_23^3-...
175 ke/m*qq^2*(x(13)-x(5))/L_24^3+qq/m*(AK2*x(5)+AINT2*cos(omega*t));...
176
177 x(8) ;    ke/m*qq^2*(x(7)-x(3))/L_12^3-c/m*x(8)-...
178 k/m*(x(7)-x(3))*(1-L/L_12)-b/m*(x(7)-x(3))*(v_12/L_12^2)+...
179 ke/m*qq^2*(x(7)-yf)/L_2f^3-ke/m*qq^2*(x(11)-x(7))/L_23^3-...
180 ke/m*qq^2*(x(15)-x(7))/L_24^3;...
181
```

```
x(10);     ...
    k/m*(x(13)-x(9))*(1-L/L_34)+b/m*(x(13)-x(9))*(v_34/L_34^2)-...
c/m*x(10)-k/m*(x(9)-x(5))*(1-L/L_23)-b/m*(x(9)-x(5))*(v_23/L_23^2)+...
ke/m*qq^2*(x(9)-xf)/L_3f^3+ke/m*qq^2*(x(9)-x(1))/L_13^3+...
ke/m*qq^2*(x(9)-x(5))/L_23^3-ke/m*qq^2*(x(13)-x(9))/L_34^3+...
qq/m*(AK3*x(9)+AINT3*cos(omega*t));...

x(12);     ...
    k/m*(x(15)-x(11))*(1-L/L_34)+b/m*(x(15)-x(11))*(v_34/L_34^2)-...
c/m*x(12)-k/m*(x(11)-x(7))*(1-L/L_23)-b/m*(x(11)-x(7))*(v_23/L_23^2)+...
ke/m*qq^2*(x(11)-yf)/L_3f^3+ke/m*qq^2*(x(11)-x(3))/L_13^3+...
ke/m*qq^2*(x(11)-x(7))/L_23^3-ke/m*qq^2*(x(15)-x(11))/L_34^3;...

x(14);     -c4/m*x(14)-k/m*(x(13)-x(9))*(1-L/L_34)-...
b/m*(x(13)-x(9))*(v_34/L_34^2)+ke/m*qq^2*(x(13)-xf)/L_4f^3+...
ke/m*qq^2*(x(13)-x(1))/L_14^3+ke/m*qq^2*(x(13)-x(5))/L_24^3+...
ke/m*qq^2*(x(13)-x(9))/L_34^3;...

x(16);     -c4/m*x(16)-k/m*(x(15)-x(11))*(1-L/L_34)-...
b/m*(x(15)-x(11))*(v_34/L_34^2)+ke/m*qq^2*(x(15)-yf)/L_4f^3+...
ke/m*qq^2*(x(15)-x(3))/L_14^3+ke/m*qq^2*(x(15)-x(7))/L_24^3+...
ke/m*qq^2*(x(15)-x(11))/L_34^3];
end

function xp=single_fib2(t,x,z,k,ke,qq,m,c,L,omega,xf,yf...
,zf,AK1,AINT1,AK2,AINT2,AK3,AINT3,b,c4)
% Distances between beads
L_1f=sqrt((x(1)-xf)^2+(x(3)-yf)^2+(z(1)-zf)^2);
L_2f=sqrt((x(5)-xf)^2+(x(7)-yf)^2+(z(2)-zf)^2);
L_3f=sqrt((x(9)-xf)^2+(x(11)-yf)^2+(z(3)-zf)^2);
L_4f=sqrt((x(13)-xf)^2+(x(15)-yf)^2+(z(4)-zf)^2);
L_12=sqrt((x(5)-x(1))^2+(x(7)-x(3))^2+(z(2)-z(1))^2);
L_13=sqrt((x(9)-x(1))^2+(x(11)-x(3))^2+(z(3)-z(1))^2);
L_14=sqrt((x(13)-x(1))^2+(x(15)-x(3))^2+(z(4)-z(1))^2);
```

```
214 L_23=sqrt((x(9)-x(5))^2+(x(11)-x(7))^2+(z(3)-z(2))^2);
215 L_24=sqrt((x(13)-x(5))^2+(x(15)-x(7))^2+(z(4)-z(2))^2);
216 L_34=sqrt((x(13)-x(9))^2+(x(15)-x(11))^2+(z(4)-z(3))^2);
217
218 % Bead velocities
219 v_1f=(x(3)-yf)*x(4)+(x(1)-xf)*(x(2));
220 v_12=(x(7)-x(3))*(x(8)-x(4))+(x(5)-x(1))*(x(6)-x(2));
221 v_23=(x(11)-x(7))*(x(12)-x(8))+(x(9)-x(5))*(x(10)-x(6));
222 v_34=(x(15)-x(11))*(x(16)-x(12))+(x(13)-x(9))*(x(14)-x(10));
223
224 % State matrix
225 xp = [x(2) ;    k/m*(x(5)-x(1))*(1-L/L_12)+...
226 b/m*(x(5)-x(1))*(v_12/L_12^2)-c/m*x(2)-k/m*(x(1)-xf)*(1-L/L_1f)-...
227 b/m*(x(1)-xf)*(v_1f/L_1f^2)+ke/m*qq^2*(x(1)-xf)/L_1f^3-...
228 ke/m*qq^2*(x(5)-x(1))/L_12^3-ke/m*qq^2*(x(9)-x(1))/L_13^3-...
229 ke/m*qq^2*(x(13)-x(1))/L_14^3+qq/m*(AK1*x(1)+...
230 AINT1*square(omega*t+pi/2));...
231
232       x(4) ;    ke/m*qq^2*(x(3)-yf)/L_1f^3-c/m*x(4)-...
233 k/m*(x(3)-yf)*(1-L/L_1f)+k/m*(x(7)-x(3))*(1-L/L_12)-...
234 b/m*(x(3)-yf)*(v_1f/L_1f^2)+b/m*(x(7)-x(3))*(v_12/L_12^2)-...
235 ke/m*qq^2*(x(7)-x(3))/L_12^3-ke/m*qq^2*(x(11)-...
236 x(3))/L_13^3-ke/m*qq^2*(x(15)-x(3))/L_14^3;...
237
238 x(6) ;    ke/m*qq^2*(x(5)-x(1))/L_12^3-c/m*x(6)-...
239 k/m*(x(5)-x(1))*(1-L/L_12)-b/m*(x(5)-x(1))*(v_12/L_12^2)+...
240 ke/m*qq^2*(x(5)-xf)/L_2f^3-ke/m*qq^2*(x(9)-x(5))/L_23^3-...
241 ke/m*qq^2*(x(13)-x(5))/L_24^3+qq/m*(AK2*x(5)+...
242 AINT2*square(omega*t+pi/2));...
243
244 x(8) ;    ke/m*qq^2*(x(7)-x(3))/L_12^3-c/m*x(8)-...
245 k/m*(x(7)-x(3))*(1-L/L_12)-b/m*(x(7)-x(3))*(v_12/L_12^2)+...
246 ke/m*qq^2*(x(7)-yf)/L_2f^3-ke/m*qq^2*(x(11)-x(7))/L_23^3-...
247 ke/m*qq^2*(x(15)-x(7))/L_24^3;...
```

```
248
249  x(10);     k/m*(x(13)-x(9))*(1-L/L_34)+...
250 b/m*(x(13)-x(9))*(v_34/L_34^2)-c/m*x(10)-...
251 k/m*(x(9)-x(5))*(1-L/L_23)-b/m*(x(9)-x(5))*(v_23/L_23^2)+...
252 ke/m*qq^2*(x(9)-xf)/L_3f^3+ke/m*qq^2*(x(9)-x(1))/L_13^3+...
253 ke/m*qq^2*(x(9)-x(5))/L_23^3-ke/m*qq^2*(x(13)-x(9))/L_34^3+...
254 qq/m*(AK3*x(9)+AINT3*square(omega*t+pi/2));...
255
256  x(12);     k/m*(x(15)-x(11))*(1-L/L_34)+...
257 b/m*(x(15)-x(11))*(v_34/L_34^2)-c/m*x(12)-...
258 k/m*(x(11)-x(7))*(1-L/L_23)-b/m*(x(11)-x(7))*(v_23/L_23^2)+...
259 ke/m*qq^2*(x(11)-yf)/L_3f^3+ke/m*qq^2*(x(11)-x(3))/L_13^3+...
260 ke/m*qq^2*(x(11)-x(7))/L_23^3-ke/m*qq^2*(x(15)-x(11))/L_34^3;...
261
262  x(14);     -c4/m*x(14)-k/m*(x(13)-x(9))*(1-L/L_34)-...
263 b/m*(x(13)-x(9))*(v_34/L_34^2)+ke/m*qq^2*(x(13)-xf)/L_4f^3+...
264 ke/m*qq^2*(x(13)-x(1))/L_14^3+ke/m*qq^2*(x(13)-x(5))/L_24^3+...
265 ke/m*qq^2*(x(13)-x(9))/L_34^3;...
266
267  x(16);     -c4/m*x(16)-k/m*(x(15)-x(11))*(1-L/L_34)-...
268 b/m*(x(15)-x(11))*(v_34/L_34^2)+ke/m*qq^2*(x(15)-yf)/L_4f^3+...
269 ke/m*qq^2*(x(15)-x(3))/L_14^3+ke/m*qq^2*(x(15)-x(7))/L_24^3+...
270 ke/m*qq^2*(x(15)-x(11))/L_34^3];
271 end
```

A.2 Matlab Code for Maxwell material model simulation

A.2.1 Point Charge Approximation

```
1 clear all, clc
2 global tland told
3
```

```
4  % This is a setup for 2D steering with 2 pair of auxiliary ...
       electrodes
5  % in anti-phase. If different electrode setup is required, ...
       coordinates
6  %of all additional point charges need to be supplied, together with
7  %the desired potential in their proximity.
8  %(To be able to optimize point charge values)
9  NV=8e3;     % Nozzle Voltage
10 EV=10e3;         % Auxiliary Electrode High
11 NC=0.07;         % Nozzle to Collector Distance
12 EE=0.11;         % Lateral Auxiliary Electrode Separation
13 NE1=NC/4;        % Nozzle to 1st Auxiliary Electrode Pair Distance
14 EEZ=NC/2;        % Axial Auxiliary Electrode Pair Separation
15 NE2=NE1+EEZ;     % Nozzle to 2nd Electrode Pair
16 % Auxiliary electrode geometry
17 El=0.1;
18 Ew=0.01;
19 % Collector geometry
20 Ch=0.05;
21 Cw=0.08;
22 %Nozzle diameter
23 Nd=0.002;
24
25
26 % Point Charge Positions
27 pos=[0,0,0-Nd*6;                                        %nozzle
28
29     -EE/2-Ew/2,-El/2,NE1;                              %el_1 top
30     -EE/2-Ew/2,El/4,NE1;                               %el_1 mid_top
31     -EE/2-Ew/2,0,NE1;                                     %el_1 middle
32     -EE/2-Ew/2,-El/4,NE1;                              %el_1 mid_bot
33     -EE/2-Ew/2,El/2,NE1;                               %el_1 bottom
34
35      EE/2+Ew/2,El/2,NE1;                               %el_2 bottom
```

```
36      EE/2+Ew/2,-El/4,NE1;                          %el_2 mid_bot
37      EE/2+Ew/2,0,NE1;                                 %el_2 middle
38      EE/2+Ew/2,El/4,NE1;                           %el_2 mid_top
39      EE/2+Ew/2,-El/2,NE1;                          %el_2 top
40
41     -El/2,EE/2+Ew/2,NE2;                          %el_3 left
42     -El/4,EE/2+Ew/2,NE2;                          %el_3 mid_left
43     0,EE/2+Ew/2,NE2;                              %el_3 middle
44     El/4,EE/2+Ew/2,NE2;                           %el_3 mid_right
45     El/2,EE/2+Ew/2,NE2;                           %el_3 right
46
47     El/2,-EE/2-Ew/2,NE2;                          %el_4 right
48     El/4,-EE/2-Ew/2,NE2;                          %el_4 mid_right
49     0,-EE/2-Ew/2,NE2;                             %el_4 middle
50     -El/4,-EE/2-Ew/2,NE2;                         %el_4 mid_left
51     -El/2,-EE/2-Ew/2,NE2;                         %el_4 left
52
53     Cw/2,0,NC+Ew*2;                                %Col_top
54     0,0,NC+Ew*2;                                %Col_mid
55     0,Ch/2,NC+Ew*2;                                 %Col_right
56     0,-Ch/2,NC+Ew*2;                                %Col_left
57     -Cw/2,0,NC+Ew*2];                             %Col_bottom
58
59 ke=8.9875517873681764e9;        % Coulomb`s constant
60 Qel=EV*Ew/2/ke;                 % Initial point charge values
61 Qn=NV*Nd/2/ke;
62 % PQ=     nozzle        1st el (H)            2nd el (L)         ...
63 %   3rd el (H)              4th el (L)              collector   ]
64 PQi1=[        Qn;       Qel*ones(5,1);      -Qel*ones(5,1); ...
65  Qel*ones(5,1);      -Qel*ones(5,1);      -Qel*ones(5,1)];
66 PQi2=[        Qn;       -Qel*ones(5,1);     Qel*ones(5,1); ...
67  -Qel*ones(5,1);      Qel*ones(5,1);      -Qel*ones(5,1)];
68
69 %% Point Charge Optimization
```

```
70 % Inspection points
71 posi=[0,0,0;                                  %nozzle
72
73     -EE/2,-El/2,NE1;                         %el_1 top
74     -EE/2,El/4,NE1;                          %el_1 mid_top
75     -EE/2,0,NE1;                             %el_1 middle
76     -EE/2,-El/4,NE1;                         %el_1 mid_bot
77     -EE/2,El/2,NE1;                          %el_1 bottom
78
79      EE/2,El/2,NE1;                          %el_2 bottom
80      EE/2,-El/4,NE1;                         %el_2 mid_bot
81      EE/2,0,NE1;                             %el_2 middle
82      EE/2,El/4,NE1;                          %el_2 mid_top
83      EE/2,-El/2,NE1;                         %el_2 top
84
85     -El/2,EE/2,NE2;                          %el_3 left
86     -El/4,EE/2,NE2;                          %el_3 mid_left
87     0,EE/2,NE2;                              %el_3 middle
88     El/4,EE/2,NE2;                           %el_3 mid_right
89     El/2,EE/2,NE2;                           %el_3 right
90
91     El/2,-EE/2,NE2;                          %el_4 right
92     El/4,-EE/2,NE2;                          %el_4 mid_right
93     0,-EE/2,NE2;                             %el_4 middle
94     -El/4,-EE/2,NE2;                         %el_4 mid_left
95     -El/2,-EE/2,NE2;                         %el_4 left
96
97     Cw/2,0,NC;                              %Col_top
98     0,0,NC;                                   %Col_mid
99     0,Ch/2,NC;                               %Col_right
100    0,-Ch/2,NC;                              %Col_left
101    -Cw/2,0,NC];                            %Col_bottom
102
103 % control vector - Expected potential at inspection points
```

```
104 CV1=[NV EV*ones(1,5) zeros(1,5) EV*ones(1,5) zeros(1,5) ...
        zeros(1,5)]';
105 CV2=[NV zeros(1,5) EV*ones(1,5) zeros(1,5) EV*ones(1,5) ...
        zeros(1,5)]';
106
107 r=zeros(length(PQi1));
108 for i=1:length(PQi1)
109     for j=1:length(PQi1)
110         r(i,j)=1/sqrt(sum((pos(i,:)-posi(j,:)).^2));
111     end
112 end
113 C1=(ke*PQi1)'.*ones(length(PQi1)).*r';
114 C2=(ke*PQi2)'.*ones(length(PQi2)).*r';
115
116 % Built in least square error based optimization
117 coef1=lsqnonneg(C1,CV1);
118 coef2=lsqnonneg(C2,CV2);
119
120 % Point charge correction application
121 PQ1=PQi1.*coef1
122 PQ2=PQi2.*coef2
123 Ey1=@(x,y,z)  sum(   ...
        ((pos(:,2)-y*ones(length(pos(:,1)),1))*ke.*PQ1)'./ ...
124 sqrt(sum(transpose(([x y ...
        z].*ones(length(pos(:,1)),3)-pos).^2))).^3  );
125
126 Ex1=@(x,y,z)  sum(   ...
        ((pos(:,1)-x*ones(length(pos(:,1)),1))*ke.*PQ1)'./ ...
127 sqrt(sum(transpose(([x y ...
        z].*ones(length(pos(:,1)),3)-pos).^2))).^3  );
128
129 Ez1=@(x,y,z)  sum(   ...
        ((pos(:,3)-z*ones(length(pos(:,1)),1))*ke.*PQ1)'./ ...
```

```
130 sqrt(sum(transpose(([x y ...
       z].*ones(length(pos(:,1)),3)-pos).^2))).^3  );
131
132 Ey2=@(x,y,z)  sum(   ...
       ((pos(:,2)-y*ones(length(pos(:,1)),1))*ke.*PQ2)'./ ...
133 sqrt(sum(transpose(([x y ...
       z].*ones(length(pos(:,1)),3)-pos).^2))).^3  );
134
135 Ex2=@(x,y,z)  sum(   ...
       ((pos(:,1)-x*ones(length(pos(:,1)),1))*ke.*PQ2)'./ ...
136 sqrt(sum(transpose(([x y ...
       z].*ones(length(pos(:,1)),3)-pos).^2))).^3  );
137
138 Ez2=@(x,y,z)  sum(   ...
       ((pos(:,3)-z*ones(length(pos(:,1)),1))*ke.*PQ2)'./ ...
139 sqrt(sum(transpose(([x y ...
       z].*ones(length(pos(:,1)),3)-pos).^2))).^3  );
140
141
142
143 %% Potential Function
144 Pot1=@(x,y,z)sum(ke*PQ1'./sqrt(sum(transpose(([x y z]. ...
145 *ones(length(pos(:,1)),3)-pos).^2))))
146 E1=@(x,y,z)sum(ke*PQ1'./sum(transpose(([x y z]. ...
147 *ones(length(pos(:,1)),3)-pos).^2)))
148
149 Pot2=@(x,y,z)sum(ke*PQ2'./sqrt(sum(transpose(([x y z]. ...
150 *ones(length(pos(:,1)),3)-pos).^2))))
151 E2=@(x,y,z)sum(ke*PQ2'./sum(transpose(([x y z]. ...
152 *ones(length(pos(:,1)),3)-pos).^2)))
153
154 %% XZ Plane Potential distribution
155
156 [X,Y,Z]=meshgrid(linspace(-EE/2,EE/2,101), ...
```

```
157 linspace(-EE/2,EE/2,101),linspace(0,NC,101));
158 xzpot=zeros(size(X(:,:,1)));
159 xzE=zeros(size(X(:,:,1)));
160 zz(:,:)=Z(:,1,:);
161 zz=zz';
162 xx=X(:,:,1);
163 for i=1:length(X(:,1,1))
164     for j=1:length(X(1,:,1))
165 xzpot(i,j)=Pot1(xx(i,j),0,zz(i,j));
166 xzE(i,j)=E1(xx(i,j),0,zz(i,j));
167     end
168 end
169
170 figure;
171 subplot(2,2,1),surf(X(:,:,1),zz,xzpot),title('U[V]');
172 xlabel('X[m]');ylabel('Z[m]');zlabel('U[V]');view([1,0.2,0.5]);
173 subplot(2,2,2),contour(X(:,:,1),zz,xzpot,100);
174 colorbar;title('U[V]');xlabel('X[m]');ylabel('Z[m]');
175 subplot(2,2,3),surf(X(:,:,1),zz,xzE),title('E[V/m]');
176 xlabel('X[m]');ylabel('Z[m]');zlabel('U[V]');view([1,0.2,0.5]);
177 subplot(2,2,4),contour(X(:,:,1),zz,xzE,100);
178 colorbar;title('E[V/m]');xlabel('X[m]');ylabel('Z[m]');
179
180
181 %% YZ Plane Potential distribution
182
183 yzpot=zeros(size(X(:,:,1)));
184 yzE=zeros(size(X(:,:,1)));
185 zz=zz';
186 yy=Y(:,:,1);
187 for i=1:length(Y(1,1,:))
188     for j=1:length(Z(1,:,1))
189 yzpot(i,j)=Pot1(0,yy(i,j),zz(i,j));
190 yzE(i,j)=E1(0,yy(i,j),zz(i,j));
```

```
191     end
192 end
193
194 figure;
195 subplot(2,2,1),surf(yy,zz,yzpot),title('U[V]');
196 xlabel('Y[m]');ylabel('Z[m]');zlabel('U[V]');view([1,0.2,0.5]);
197 subplot(2,2,2),contour(yy,zz,yzpot,100);
198 colorbar;title('U[V]');xlabel('Y[m]');ylabel('Z[m]');
199 subplot(2,2,3),surf(yy,zz,yzE),title('E[V/m]');
200 xlabel('Y[m]');ylabel('Z[m]');zlabel('U[V]');view([1,0.2,0.5]);
201 subplot(2,2,4),contour(yy,zz,yzE,100);
202 colorbar;title('E[V/m]');xlabel('Y[m]');ylabel('Z[m]');
203
204 figure;plot3(pos(1,1),pos(1,2),pos(1,3),'oy', pos([2:6, ...
       12:16],1),pos([2:6, 12:16],2), ...
205 pos([2:6, 12:16],3),'or', pos([7:11, 17:26],1),pos([7:11, ...
       17:26],2),pos([7:11, 17:26],3),'ob');
206 view([0,1,-0.2]);xlabel('x'),ylabel('y'),zlabel('z')
207
208 %% XY Plane Potential distribution
209 xypot_E1=zeros(size(xx));
210 % xyE_E1=zeros(size(xx));
211 xypot_E2=zeros(size(xx));
212 % xyE_E2=zeros(size(xx));
213 xypot_E12=zeros(size(xx));
214 % xyE_E12=zeros(size(xx));
215 xypot_E2C=zeros(size(xx));
216 % xyE_E2C=zeros(size(xx));
217
218 yy=Y(:,:,1);
219 for i=1:length(X(:,1,1))
220     for j=1:length(X(1,:,1))
221 xypot_E1(i,j)=Pot1(xx(i,j),yy(i,j),NE1);
222 % xyE_E1(i,j)=E(xx(i,j),yy(i,j),NE1);
```

```
223
224 xypot_E12(i,j)=Pot1(xx(i,j),yy(i,j),NE1+EEZ/2);
225 % xyE_E12(i,j)=E(xx(i,j),yy(i,j),NE1+EEz/2);
226
227 xypot_E2(i,j)=Pot1(xx(i,j),yy(i,j),NE2);
228 % xyE_E2(i,j)=E(xx(i,j),yy(i,j),NE2);
229
230 xypot_E2C(i,j)=Pot1(xx(i,j),yy(i,j),NC-(NC-NE2)/2);
231 % xyE_E2C(i,j)=E(xx(i,j),yy(i,j),(NC-NE2)/2);
232     end
233 end
234
235 figure;
236 subplot(2,2,1),contour(xx,yy,xypot_E1,100);
237 colorbar;title('E1');xlabel('X[m]');ylabel('Y[m]');
238 subplot(2,2,2),contour(xx,yy,xypot_E12,100);
239 colorbar;title('E1-E2');xlabel('X[m]');ylabel('Y[m]');
240 subplot(2,2,3),contour(xx,yy,xypot_E2,100);
241 colorbar;title('E2');xlabel('X[m]');ylabel('Y[m]');
242 subplot(2,2,4),contour(xx,yy,xypot_E2C,100);
243 colorbar;title('E2-Col');xlabel('X[m]');ylabel('Y[m]');
244
245 %% EF components along axis
246
247 Ey2=@(x,y,z)  sum(   ...
       ((pos(:,2)-y*ones(length(pos(:,1)),1))*ke.*PQ1)'. ...
248 /sqrt(sum(transpose(([x y ...
       z].*ones(length(pos(:,1)),3)-pos).^2))).^3  );
249
250 Ex2=@(x,y,z)  sum(   ...
       ((pos(:,1)-x*ones(length(pos(:,1)),1))*ke.*PQ1)'. ...
251 /sqrt(sum(transpose(([x y ...
       z].*ones(length(pos(:,1)),3)-pos).^2))).^3  );
252
```

```
253 Ez2=@(x,y,z)  sum(   ...
       ((z*ones(length(pos(:,1)),1)-pos(:,3))*ke.*PQ1)'. ...
254 /sqrt(sum(transpose(([x y ...
       z].*ones(length(pos(:,1)),3)-pos).^2))).^3  );
255
256 Ey1=@(x,y,z)  sum(   ...
       ((pos(:,2)-y*ones(length(pos(:,1)),1))*ke.*PQ2)'. ...
257 /sqrt(sum(transpose(([x y ...
       z].*ones(length(pos(:,1)),3)-pos).^2))).^3  );
258
259 Ex1=@(x,y,z)  sum(   ...
       ((pos(:,1)-x*ones(length(pos(:,1)),1))*ke.*PQ2)'. ...
260 /sqrt(sum(transpose(([x y ...
       z].*ones(length(pos(:,1)),3)-pos).^2))).^3  );
261
262 Ez1=@(x,y,z)  sum(   ...
       ((z*ones(length(pos(:,1)),1)-pos(:,3))*ke.*PQ2)'. ...
263 /sqrt(sum(transpose(([x y ...
       z].*ones(length(pos(:,1)),3)-pos).^2))).^3  );
264
265 Xa=linspace((-EE+0.005)/2,(EE-0.005)/2,101)'; Ya=Xa; ...
       Za=linspace(0,NC,101)';
266 for i=1:length(Ya)
267 EYa11(i)=Ey1(0,Ya(i),NE1);
268 EXa11(i)=Ex1(Xa(i),0,NE1);
269 EYa12(i)=Ey1(0,Ya(i),NE2);
270 EXa12(i)=Ex1(Xa(i),0,NE2);
271 EZa1(i)=Ez1(0,0,Za(i));
272
273 EYa21(i)=Ey2(0,Ya(i),NE1);
274 EXa21(i)=Ex2(Xa(i),0,NE1);
275 EYa22(i)=Ey2(0,Ya(i),NE2);
276 EXa22(i)=Ex2(Xa(i),0,NE2);
277 EZa2(i)=Ez2(0,0,Za(i));
```

```
278 end
279 figure;
280 subplot(1,4,1),plot(Xa,EXa11);xlabel('X[m]');ylabel('E_x[V/m]');
281 subplot(1,4,2),plot(Ya,EYa11);xlabel('Y[m]');ylabel('E_y[V/m]');
282 subplot(1,4,3),plot(Xa,EXa12);xlabel('X[m]');ylabel('E_x[V/m]');
283 subplot(1,4,4),plot(Ya,EYa12);xlabel('Y[m]');ylabel('E_y[V/m]');
284 figure;
285 subplot(1,4,1),plot(Xa,EXa21);xlabel('X[m]');ylabel('E_x[V/m]');
286 subplot(1,4,2),plot(Ya,EYa21);xlabel('Y[m]');ylabel('E_y[V/m]');
287 subplot(1,4,3),plot(Xa,EXa22);xlabel('X[m]');ylabel('E_x[V/m]');
288 subplot(1,4,4),plot(Ya,EYa22);xlabel('Y[m]');ylabel('E_y[V/m]');
```

A.2.2 Fiber Model Definition and Result Display

```
1  %% Material Properties
2  l=1e-3;                        % Fiber segment initial length
3  Ls = l;
4  d=(3e-7);                     % Fiber diameter 300nm
5  ro=1e3;                        % water density(as only 5% PEO )
6  M=l*pi*d^2/4*ro;
7  ni=(1.983e-5);              % dynamic viscosity
8  % Stokes drag
9  c=3*pi*ni*(1.5*d^2*l)^(1/3)*1.25*40;
10 CDmax=5.0500e-05;  % Initial structural damping coefficient
11 E=7e9;                          % Young moduli of individual PEO ...
       fibers
12 k=E*3.14*d^2/4/l;      % Stiffness coefficient
13 I=1e-7;          % Electric current measurement
14 v=2.25;                         % Measured fiber velocity
15 Q=I/v*l;               % Electric charge
16 ke=8.9875517873681764e9;    % Coulomb`s constant
17
```

```
18 T = 10;
19 L= NC;
20 % Frequency of the potential function applied to auxiliary ...
       electrodes
21 W = 80*2*pi;
22
23 % Corrections
24 Q=Q/60;
25 k=k/800;
26 M=M*3
27
28 % Max number of beads
29 Iteration=500;
30
31 N = 2; Initial = [0 1e-4   0 1e-4   0 Ls   0   0 0 0];
32 Data = struct; U_max = zeros(Iteration,1); Um_max = ...
       zeros(Iteration,1);
33 Us_max = zeros(Iteration,1); Uc_max = zeros(Iteration,1); U_min ...
       = zeros(Iteration,1);
34 Um_min = zeros(Iteration,1); Us_min = zeros(Iteration,1); Uc_min ...
       = zeros(Iteration,1);
35 T_max = 0;
36 Data(1).RR=[];Data(1).L=[];
37 Data(1).VV=[];Data(1).Vz=[];
38
39 RES=[]; PosDel=zeros(3,1); fix=0; told=[0;0];tland=[0;0]; ...
       tnew=[0;0]; t_tot=[];
40 for kk = 1:Iteration
41 disp(kk);
42 options = odeset('Events',@(t,y)Events(t,y,N,NC,Ls));
43
44 [t,y,te,ye,ie] = ode15s(@(t,y)
45 Dynamics(t,y,N,NC,M,k,Ls,c,CDmax,Q, ...
46 ke,W,T_max,Ex1,Ey1,Ez1,Ex2,Ey2),[0 T],Initial,options);
```

```
47
48
49  Uc = zeros(length(t),1); Us = zeros(length(t),1);
50  R = zeros(size(y,1),3*(N-1));
51  LL=zeros(length(t),Iteration); V=zeros(length(t),N-1);
52      for n=1:length(t)
53          L = zeros(N-1,N); us = zeros(N-1,N); uc = zeros(N-1,N);
54          for i = 1:N-1
55              for j = i+1:N
56                  L(i,j) = ...
                        sqrt((y(n,j)-y(n,i))^2+(y(n,j+N)-y(n,i+N))^2 ...
57                              +(y(n,j+2*N)-y(n,i+2*N))^2);
58                  uc(i,j) = (ke*Q^2)/(L(i,j));
59
60              end
61                  us(i,i+1) = 0.5*k*(L(i,i+1) - y(n,3*N+i) -Ls)^2;
62                  R(n,i:N-1:3*(N-1)) = y(n,(1:N:3*N)+i)- ...
                        y(n,3*N+i). ...
63                  *[(y(n,i+1)-y(n,i)) (y(n,i+1+N)-y(n,i+N)) ...
                        (y(n,i+1+2*N)-y(n,i+2*N))]/L(i,i+1);
64                  V(n,i)=sqrt(sum(y(n,(4*N-1:N-1:6*N-3)+i).^2));
65
66          end
67          Uc(n,1) = sum(sum(uc));
68          Us(n,1) = sum(sum(us));
69          LL(n,1:N-1)=flip(sum(L(:,2:end).*eye(N-1,N-1)));
70
71      end
72  % create database for R values
73  Data(1).RR(end+1:end+length(t), ...
74  1:Iteration)=zeros(length(t),Iteration);
75  Data(1).RR(end-length(t)+1:end,1:N-1)= ...
76  flip(y(:,3*N+1:4*N-1),2);
```

```
77  t_tot(end+1:end+length(t))=t'+T_max; ...

78  Data(1).L(end+1:end+length(t),1:Iteration)=LL;
79  % create database for Velocity
80  Data(1).VV(end+1:end+length(t), ...
81  1:Iteration)=zeros(length(t),Iteration);
82  Data(1).VV(end-length(t)+1:end,1:N-1)=flip(V,2);
83  Data(1).Vz(end+1:end+length(t),1:Iteration)= ...
84  zeros(length(t),Iteration);
85  Data(1).Vz(end-length(t)+1:end,1:N-1)=y(:,7*N-4:-1:6*N-2);
86
87      Um = 0.5*M*sum(y(:,4*N:7*N-4).^2,2);
88      U = Um + Us + Uc;
89
90  U_max(kk,1) = max(U); Um_max(kk,1) = max(Um); Us_max(kk,1) = ...
       max(Us);
91  Uc_max(kk,1) = max(Uc); U_min(kk,1) = min(U); Um_min(kk,1) = ...
       min(Um);
92  Us_min(kk,1) = min(Us);      Uc_min(kk,1) = min(Uc);
93  Data(kk).N = N; Data(kk).Y = y(:,1:3*N); Data(kk).Xe = ...
       zeros(size(y,1),1);
94  Data(kk).Ye = zeros(size(y,1),1); Data(kk).Ze = -ones(size(y,1),1);
95  Data(kk).R = R; Data(kk).U = [U Um Us Uc]; Data(kk).t = t + ...
       T_max; T_max = max(Data(kk).t);
96
97      if      ie == 1
98  %length of the new segment is Ls; direction of the new bead`s ...
       position vector is the same as the old ones`
99  L0=Ls*y(end,2:N:2*N+2)/norm(y(end,2:N:2*N+2));
100 V0 = y(size(y,1),4*N:N-1:6*N-2)/4 );
101
102 %update initial conditions
103 Initial = [0 L0(1,1) y(size(y,1),2:N) 0 L0(1,2) ...
       y(size(y,1),N+2:2*N) 0 L0(1,3)  ...
```

```
104 y(size(y,1),2*N+2:3*N) 0 y(size(y,1),3*N+1)-Ls ...
        y(size(y,1),3*N+2:4*N-1) V0(1,1)  ...
105 y(size(y,1),4*N:5*N-2) V0(1,2) y(size(y,1),5*N-1:6*N-3) V0(1,3) ...
        y(size(y,1),6*N-2:7*N-4)];
106
107
108     N = N + 1;        % Add a bead to the system      DOFs + 4
109     tland=[0;tland]; % Expand the vector containing bead landing ...
            times
110     told=[0;told];
111
112     end
113 end
114 % Compute the Δ_L elongation(+)/compression(-) of the springs at ...
        all time steps. plot over the t_tot
115 Data(1).Spring=Data(1).L-Data(1).RR-Ls;
116 Data(1).Spring_cor=Data(1).Spring;
117 Data(1).Spring_cor(Data(1).Spring_cor==-Ls)=0;
118
119 figure;
120 subplot(3,1,1);plot(t_tot,Data(1).L(:,1:3));title('Fiber ...
        Segment(L)');xlabel('t[s]'); ylabel('L[m]');
121 subplot(3,1,2);plot(t_tot,Data(1).Spring_cor(:,1:3));
122 title('Δ_L spring (L-R-Ls)(elong+/compress-)');xlabel('t[s]'); ...
        ylabel('del_L[m]');
123 subplot(3,1,3);plot(t_tot,Data(1).RR(:,1:3));title('Damper ...
        Stretch');xlabel('t[s]'); ylabel('R[m]');
124
125 figure;
126 subplot(3,1,1);plot(t_tot(2:end), ...
127 (Data(1).RR(2:end,1:3)-Data(1).RR(1:end-1,1:3)). ...
128 /[(t_tot(2:end)-t_tot(1:end-1))' (t_tot(2:end)- ...
129 t_tot(1:end-1))' (t_tot(2:end)-t_tot(1:end-1))']) ...
```

```
130 ;title('Damper Stretch Velocity-num derivative ...
       dR/dt');xlabel('t[s]'); ylabel('R[m/s]');
131 subplot(3,1,2);plot(t_tot,Data(1).VV(:,1:3));title('Bead ...
       Velocity');xlabel('t[s]'); ylabel('V[m/s]');
132 subplot(3,1,3);plot(t_tot,Data(1).Vz(:,1:3));title('Bead ...
       Vel_Z');xlabel('t[s]'); ylabel('V_Z[m/s]');
133
134 % Fiber extrusion animation
135 for kk = 1:size(Data,2)
136 maxx(kk)=max(abs(Data(kk).Xe(end)),abs(Data(kk).Ye(end)));
137 end
138 maxxx=max(maxx);
139 if maxxx==0
140     maxxx=1;
141 end
142 figure('units','normalized','outerposition',[0 0 1 0.95]); ...
       set(gcf,'color','w');
143 subplot('Position',[0.04, 0.08, 0.57, 0.8]);
144 plot3(0,0,0,'o',NC,0,0,'+','LineWidth',2,'Color','k');
145 axis([0 NC -5e-2 +5e-2 -5e-2 +5e-2]); box on; hold on; grid on; ...
       grid minor; pause on;
146 title('Fiber Animation','FontSize',12); xlabel('Z','FontSize',10);
147 ylabel('Y','FontSize',10); zlabel('X','FontSize',10);
148 P02 = plot3(Data(1).R(1,3),Data(1).R(1,1), ...
149 Data(1).R(1,2),'LineStyle','none', ...
150 'Marker','o','MarkerSize',4,'MarkerFaceColor','k', ...
151 'MarkerEdgeColor','k');
152 P03 = plot3(Data(1).Y(1,6),Data(1).Y(1,2), ...
153 Data(1).Y(1,4),'LineStyle','none', ...
154 'Marker','o','MarkerSize',6,'MarkerFaceColor', ...
155 'b','MarkerEdgeColor','k');
156 P04 = plot3(Data(1).Y(1,5:6),Data(1).Y(1,1:2),Data(1).Y(1,3:4), ...
157 'LineStyle','-.','LineWidth',1.5,'Color','k');
```

```
158 P05 = ...
       animatedline('LineStyle','none','Marker','.','MarkerSize',5, ...
159 'MarkerFaceColor','r','MarkerEdgeColor','r');
160 subplot('Position',[0.70, 0.7, 0.27, 0.15]); P10 = ...
       animatedline('LineWidth',1.0,'Color','r');
161 box on; grid on; grid minor; axis([0 T_max -1 1]); title('grad(E_x);
162 +Anti-confining; - Confining ','FontSize',10); ...
       xlabel('time','FontSize',10);
163 subplot('Position',[0.70, 0.45, 0.27, 0.15]); P11 = ...
       animatedline('LineWidth',0.2,'Color','m');
164 box on; grid on; grid minor; axis([0 T_max -1 1]); title('grad(E_y);
165 +Anti-confining; - Confining ','FontSize',10); ...
       xlabel('time','FontSize',10);
166 subplot('Position',[0.70, 0.1, 0.27, 0.27]);axis([-5e-2 +5e-2 ...
       -5e-2 +5e-2]);
167 P23 = plot(Data(1).Y(1,1:2),Data(1).Y(1,3:4),'ob', ...
168 'MarkerSize',4,'MarkerFaceColor','b','MarkerEdgeColor','k')
169 ;axis([-5e-2 +5e-2 -5e-2 +5e-2]); box on; hold on; grid on; grid ...
       minor;
170 title('Collector','FontSize',12); xlabel('X','FontSize',10); ...
       ylabel('Y','FontSize',10);
171
172 for kk = 1:size(Data,2)
173     for n = 1:size(Data(kk).Y,1)
174 set(P02,'XData',Data(kk).R(n,2*Data(kk).N-1:3*(Data(kk).N-1)), ...
175 'YData',Data(kk).R(n,1:1*(Data(kk).N-1)), ...
176 'ZData',Data(kk).R(n,Data(kk).N:2*(Data(kk).N-1))) ...
177
178 set(P03,'XData',Data(kk).Y(n,2*Data(kk).N+2:3*Data(kk).N), ...
179 'YData',Data(kk).Y(n,2:Data(kk).N), ...
180 'ZData',Data(kk).Y(n,Data(kk).N+2:2*Data(kk).N)) ...
181
182 set(P04,'XData',Data(kk).Y(n,2*Data(kk).N+1:3*Data(kk).N), ...
183 'YData',Data(kk).Y(n,1:Data(kk).N), ...
```

```
184 'ZData',Data(kk).Y(n,Data(kk).N+1:2*Data(kk).N)) ...
185
186 addpoints(P05,Data(kk).Ze(n,1),Data(kk).Xe(n,1),Data(kk).Ye(n,1))
187
188 addpoints(P10,Data(kk).t(n,1),square(Data(kk).t(n,1)*W))
189
190 addpoints(P11,Data(kk).t(n,1),-square(Data(kk).t(n,1)*W))
191
192 set(P23,'XData',Data(kk).Y(n,1:Data(kk).N). ...
193 *(Data(kk).Y(n,2*Data(kk).N+1:3*Data(kk).N)>(NC-1e-4)), ...
194 'YData',Data(kk).Y(n,Data(kk).N+1:2*Data(kk).N). ...
195 *(Data(kk).Y(n,2*Data(kk).N+1:3*Data(kk).N)>(NC-1e-4))) ...
196 drawnow limitrate;
197     end
198 end
199
200
201 %% FUNCTIONS
202 function dydt =  ...
203 Dynamics(t,y,N,NC,M,k,Ls,c,CDmax,Q,ke,W,T_max,Ex1,Ey1,Ez1,Ex2,Ey2)
204 global tland told
205
206 dydt = zeros(7*N-4,1); L = zeros(N,N+1); cosQx = zeros(N,N+1); ...
       cosQy = zeros(N,N+1);
207 cosQz = zeros(N,N+1); Fss = zeros(1,N); Fc = zeros(N,N+1);
208
209 %find beads that have reached collector and compute the charge ...
       on these beads
210 if any((NC-y(2*N+1:3*N))<1e-4)
211 tnew=(NC-y(2*N+1:3*N))<1e-4;
212 tland=tland+(T_max+t)*(tnew-told);
213 told=tnew;
214 clear tnew
215
```

```
% Charge dissipation function
q=Q*(¬tland)+told*Q.*exp(-((T_max+t)-tland)/1e-5);                ...

else
    q=Q*ones(1,N);
end
    for i = 1:N-1
        for j = i+1:N
L(i,j) = sqrt((y(j)-y(i))^2+(y(j+N)-y(i+N))^2 ...
+(y(j+2*N)-y(i+2*N))^2);
cosQx(i,j) = (y(j    )-y(i    ))/L(i,j);
cosQy(i,j) = (y(j+  N)-y(i+  N))/L(i,j);
cosQz(i,j) = (y(j+2*N)-y(i+2*N))/L(i,j);
Fc(i,j) = (ke*q(i)*q(j))/(L(i,j)^2);
        end
Fss(i) = k*(L(i,i+1) - y(3*N+i) - Ls);
    end
dydt([2:N N+2:2*N 2*N+2:3*N]) = y(4*N:7*N-4);

% Structural damping function, representing fiber drying
Cs(1:N-1)=CDmax*(atan(10*y(2*N+2:3*N)/NC-1) ...
/2.3+atan(1)/2.2);
dydt(3*N+1:4*N-1) = Fss(1:N-1)./Cs(1:N-1);

% Fix beads that have reached the collector in their current ...
   position
    for i = 2:N
        if NC-y(2*N+i)<1e-4
            dydt(i)=0;
            dydt(N+i)=0;
            dydt(2*N+i)=0;
            dydt(4*N-2+i) = 0;
            dydt(5*N-3+i) = 0;
            dydt(6*N-4+i) = 0;
```

```
248         else
249 % Mass function - representing the H2O evaporation (considering ...
       5wt%PEO in H2O).
250 MM=M*(1+19*exp(-4*y(2*N+i)/45e-3));
251 % stiffness representing the surface tension close to the ...
       nozzle¬
252 klin=k/20*exp(-4*y(2*N+i)/10e-3);
253 % structural damping representing the surface tension close to ...
       the nozzle
254 blin=CDmax/50*exp(-4*y(2*N+i)/10e-3);
255
256 dydt(4*N-2+i) = (-blin*y(4*N-2+i) -klin*y(i) -c*y(4*N-2+i) - ...
       Fss(i-1)*cosQx(i-1,i)+ ...
257 Fss(i)*cosQx(i,i+1)- ...
       Ex1(y(i),y(N+i),y(2*N+i))*square(W*(T_max+t))*Q - ...
258 Ex2(y(i),y(N+i),y(2*N+i))*square(W*(T_max+t)+pi)*Q)/MM;
259
260 dydt(5*N-3+i) = (-blin*y(5*N-3+i) -klin*y(N+i) -c*y(5*N-3+i) - ...
       Fss(i-1)*cosQy(i-1,i)+  ...
261 Fss(i)*cosQy(i,i+1)- ...
       Ey1(y(i),y(N+i),y(2*N+i))*square(W*(T_max+t))*Q -  ...
262 Ey2(y(i),y(N+i),y(2*N+i))*square(W*(T_max+t)+pi)*Q)/MM;
263
264 dydt(6*N-4+i) = (-c/2*y(6*N-4+i) - Fss(i-1)*cosQz(i-1,i)+  ...
265 Fss(i)*cosQz(i,i+1)+ Ez1(y(i),y(N+i),y(2*N+i))*Q)/MM;
266
267
268             for j = 1:i-1
269 dydt(4*N-2+i) = dydt(4*N-2+i) + Fc(j,i)*cosQx(j,i)/MM;
270 dydt(5*N-3+i) = dydt(5*N-3+i) + Fc(j,i)*cosQy(j,i)/MM;
271 dydt(6*N-4+i) = dydt(6*N-4+i) + Fc(j,i)*cosQz(j,i)/MM;
272             end
273             for j = i+1:N
274 dydt(4*N-2+i) = dydt(4*N-2+i) - Fc(i,j)*cosQx(i,j)/MM;
```

```
275 dydt(5*N-3+i) = dydt(5*N-3+i) - Fc(i,j)*cosQy(i,j)/MM;
276 dydt(6*N-4+i) = dydt(6*N-4+i) - Fc(i,j)*cosQz(i,j)/MM;
277             end
278         end
279     end
280 end
281
282
283 % Event function checking length of the first fiber segment
284 function [value,isterminal,direction] = Events(¬,y,N,NC,Ls)
285 value(1) = y(2*N+2) - 2*Ls;
286 isterminal(1) = 1;
287 direction(1) = 0;
288
289 end
```

References

[1] Jinrong Du, Jianheng Liu, Shenglian Yao, Haiquan Mao, Jiang Peng, Xun Sun, Zheng Cao, Yongdong Yang, Bo Xiao, Yiguo Wang, Peifu Tang, and Xiumei Wang. Prompt peripheral nerve regeneration induced by a hierarchically aligned fibrin nanofiber hydrogel. *Acta Biomaterialia*, 55:296 – 309, 2017.

[2] P. Katta, M. Alessandro, R. D. Ramsier, and G. G. Chase. Continuous electrospinning of aligned polymer nanofibers onto a wire drum collector. *Nano Letters*, 4, 2004.

[3] G. Mathew, J. P. Hong, J. M. Rhee, D. J. Leo, and C. Nah. Preparation and anisotropic mechanical behavior of highly-oriented electrospun poly(butylene terephthalate) fibers. *Journal of Applied Polymer Science*, 101(3):2017–2021, 2006.

[4] D. Li, Y. Wang, and Y. Xia. Electrospinning nanofibers as uniaxially aligned arrays and layer-by-layer stacked films. *Advanced Materials*, 16(4):361–366.

[5] E. SMIT, U. BTTNER, and R.D. SANDERSON. 3 - continuous yarns from electrospun nanofibers. In P.J. Brown and K. Stevens, editors, *Nanofibers and Nanotechnology in Textiles*, Woodhead Publishing Series in Textiles, pages 45 – 70. Woodhead Publishing, 2007.

[6] Matthias M L Arras, Christian Grasl, Helga Bergmeister, and Heinrich Schima. Electrospinning of aligned fibers with adjustable orientation using auxiliary electrodes. *Science and Technology of Advanced Materials*, 13(3), 2012.

[7] Rudolf Kyselica, Eniko T. Enikov, and Rein Anton. Electrospinning under lateral electrostatic control in ambient atmosphere. *Journal of Electrostatics*, 98:75 – 81, 2019.

[8] Darrell H. Reneker and Alexander L. Yarin. Electrospinning jets and polymer nanofibers. *Polymer*, 49(10):2387 – 2425, 2008.

[9] Nandana Bhardwaj and Subhas C. Kundu. Electrospinning: A fascinating fiber fabrication technique. *Biotechnology Advances*, 28:325 – 347, 2010.

[10] Jayesh Doshi and Darrell H. Reneker. Electrospinning process and applications of electrospun fibers. *Journal of Electrostatics*, 35(2):151 – 160, 1995.

[11] Geoffrey Ingram Taylor. Disintegration of water drops in an electric field. *Proceedings of the Royal Society of London. Series A. Mathematical and Physical Sciences*, 280(1382):383–397, 1964.

[12] S. N. REZNIK, A. L. YARIN, A. THERON, and E. ZUSSMAN. Transient and steady shapes of droplets attached to a surface in a strong electric field. *Journal of Fluid Mechanics*, 516:349377, 2004.

[13] D.H. Reneker, A.L. Yarin, H. Fong, and S. Koombhongse. Bending instability of electrically charged liquid jets of polymer solutions in electrospinning. *Journal of Applied Physics*, 87(9I):4531–4547, 2000.

[14] A. L. Yarin, S. Koombhongse, and D. H. Reneker. Bending instability in electrospinning of nanofibers. *Journal of Applied Physics*, 89(5):3018–3026, 2001.

[15] C.J. Thompson, G.G. Chase, A.L. Yarin, and D.H. Reneker. Effects of parameters on nanofiber diameter determined from electrospinning model. *Polymer*, 48(23):6913 – 6922, 2007.

[16] T. Han, A.L. Yarin, and D.H. Reneker. Viscoelastic electrospun jets: Initial stresses and elongational rheometry. *Polymer*, 49(6):1651 – 1658, 2008.

[17] A. F. Von Recum, C. E. Shannon, C.n E. Cannon, K. J. Long, T. G. V. Kooten, and J. Meyle. Surface roughness, porosity, and texture as modifiers of cellular adhesion. *Tissue Engineering*, 2(4):241–253, 1996.

[18] A. I. Itl, H. O. Ylnen, C. Ekholm, K. H. Karlsson, and H. T. Aro. Pore diameter of more than 100 m is not requisite for bone ingrowth in rabbits. *Journal of Biomedical Materials Research*, 58(6):679–683, 2001.

[19] W. J. Li, C. T. Laurencin, E. J. Caterson, R.S. Tuan, and F. K. Ko. Electrospun nanofibrous structure: A novel scaffold for tissue engineering. *Journal of Biomedical Materials Research*, 60(4):613–621, 2002.

[20] H.B. Wang, M. E. Mullins, J. M. Cregg, A. Hurtado, M. Oudega, M. T. y Tromble, and R. J. Gilbert. *Journal of Neural Engineering*, 6(1):016001, dec 2008.

[21] A. Subramanian, U. M. Krishnan, and S Sethuraman. Fabrication of uniaxially aligned 3d electrospun scaffolds for neural regeneration. *Biomedical Materials*, 6(2):025004, feb 2011.

[22] Shu Wang, Andrew C.A Wan, Xiaoyun Xu, Shujun Gao, Hai-Quan Mao, Kam W Leong, and Hanry Yu. A new nerve guide conduit material composed of a biodegradable poly(phosphoester). *Biomaterials*, 22(10):1157 – 1169, 2001.

[23] Lijie Zhang and Thomas J. Webster. Nanotechnology and nanomaterials: Promises for improved tissue regeneration. *Nano Today*, 4(1):66 – 80, 2009.

[24] Sing Yian Chew, Ruifa Mi, Ahmet Hoke, and Kam W. Leong. The effect of the alignment of electrospun fibrous scaffolds on schwann cell maturation. *Biomaterials*, 29(6):653 – 661, 2008.

[25] Rahul Sahay, Velmurugan Thavasi, and Seeram Ramakrishna. Design modifications in electrospinning setup for advanced applications. 2011, 11 2011.

[26] H. Yuan, Q. Zhou, and Y. Zhang. 6 - improving fiber alignment during electrospinning. In Mehdi Afshari, editor, *Electrospun Nanofibers*, Woodhead Publishing Series in Textiles, pages 125 – 147. Woodhead Publishing, 2017.

[27] Pavel Kiselev and Joan Rosell-Llompart. Highly aligned electrospun nanofibers by elimination of the whipping motion. *Journal of Applied Polymer Science*, 125:2433–2441, 2012.

[28] B. Sundaray, V. Subramanian, T. S. Natarajan, R.Z Xiang, C.C. Chang, and W.S. Fann. Electrospinning of continuous aligned polymer fibers. *Applied Physics Letters*, 84(7):1222–1224, 2004.

[29] Xiaomei Cai, Ping Zhu, Xizhao Lu, Yifang Liu, Tingping Lei, and Daoheng Sun. Electrospinning of very long and highly aligned fibers. *Journal of Materials Science*, 52(24):14004–14010, Dec 2017.

[30] Park Suk Hee and Yang DongYol. Fabrication of aligned electrospun nanofibers by inclined gap method. *Journal of Applied Polymer Science*, 120(3):1800–1807.

[31] Jinglei Wu and Yi Hong. Enhancing cell infiltration of electrospun fibrous scaffolds in tissue regeneration. *Bioactive Materials*, 1(1):56 – 64, 2016.

[32] Luciana Meli, Jianjun Miao, Jonathan S. Dordick, and Robert J. Linhardt. Electrospinning from room temperature ionic liquids for biopolymer fiber formation. *Green Chem.*, 12:1883–1892, 2010.

[33] C. Grasl, M.M.L. Arras, M. Stoiber, H. Bergmeister, and H. Schima. Electrodynamic control of the nanofiber alignment during electrospinning. *Applied Physics Letters*, 102(5), 2013.

[34] L. M. Bellan and H. G. Craighead. Control of an electrospinning jet using electric focusing and jet-steering fields. *Journal of Vacuum Science & Technology B: Microelectronics and Nanometer Structures*, 24(6), 2006.

[35] Matthias Arras. *Macro-and Microscopical Alignment of Electrospun Fibres with Possible Use for Vascular Grafts: Experiment and Simulation*. 11 2010.

[36] Vince Beachley and Xuejun Wen. Effect of electrospinning parameters on the nanofiber diameter and length. *Materials Science and Engineering: C*, 29(3):663 – 668, 2009.

[37] Tong Lin and Jian Fang. *Fundamentals of Electrospinning & Electrospun Nanofibers*. DEStech Publications, Inc., 2017.

[38] J. Macossay, A. Marruffo, R. Rincon, T. Eubanks, and A. Kuang. Effect of needle diameter on nanofiber diameter and thermal properties of electrospun poly(methyl methacrylate). *Polymers for Advanced Technologies*, 18(3):180–183, 2007.

[39] C. Kuchi, G.S. Harish, and P. S. Reddy. Effect of polymer concentration, needle diameter and annealing temperature on tio2-pvp composite nanofibers synthesized by electrospinning technique. *Ceramics International*, 44(5):5266 – 5272, 2018.

[40] Won Keun Son, Ji Ho Youk, Taek Seung Lee, and Won Ho Park. The effects of solution properties and polyelectrolyte on electrospinning of ultrafine poly(ethylene oxide) fibers. *Polymer*, 45(9):2959 – 2966, 2004.

[41] F. Cengiz and O. Jirsak. The effect of salt on the roller electrospinning of polyurethane nanofibers. *Fibers and Polymers*, 10(2):177–184, 2009.

[42] F. Yalcinkaya, B. Yalcinkaya, and O. Jirsak. Influence of salts on electrospinning of aqueous and nonaqueous polymer solutions. *Journal of Nanomaterials*, 2015:12, 2015.

[43] F. Yalcinkaya, B. Yalcinkaya, and O. Jirsak. Experimental investigation of salt effect on electrospinning parameters and nanofiber morphology. *NANOCON*, 2014.

[44] Z. Li and C. Wang. *Effects of Working Parameters on Electrospinning*, pages 15–28. Springer Berlin Heidelberg, 2013.

[45] Q. Yang, Z. Li, Y. Hong, Y. Zhao, S. Qiu, C. Wang, and Y. Wei. Influence of solvents on the formation of ultrathin uniform poly(vinyl pyrrolidone) nanofibers with electrospinning. *Journal of Polymer Science Part B: Polymer Physics*, 42(20):3721–3726.

[46] Ying Yang, Zhidong Jia, Qiang Li, and Zhicheng Guanand. Experimental investigation of the governing parameters in the electrospinning of polyethylene oxide solution. *IEEE Transactions on Dielectrics and Electrical Insulation*, 13(3):580–585, 2006.

[47] S. De Vrieze, T. Van Camp, A. Nelvig, B. Hagström, P. Westbroek, and K. De Clerck. The effect of temperature and humidity on electrospinning. *Journal of Materials Science*, 44(5):1357–1362, 2009.

[48] Wolfgang Paul. Electromagnetic traps for charged and neutral particles. *Rev. Mod. Phys.*, 62:531–540, Jul 1990.

[49] J.E. Campana. Elementary theory of the quadrupole mass filter. *International Journal of Mass Spectrometry and Ion Physics*, 33(2):101 – 117, 1980.

[50] Rudolf Kyselica, Eniko T. Enikov, and Rein Anton. One- and two-dimensional electrodynamic steering of electrospun polymer nanofibers. *Applied Physics Letters*, 113(18):183705, 2018.

[51] Zhe Song, Sum Wai Chiang, Xiaodong Chu, Hongda Du, Jia Li, Lin Gan, Chengjun Xu, Youwei Yao, Yanbing He, Baohua Li, and Feiyu Kang. Effects of solvent on structures and properties of electrospun poly(ethylene oxide) nanofibers. *Journal of Applied Polymer Science*, 135(5):45787.

[52] Rudolf Kyselica, Eniko T. Enikov, Peter Polyvas, and Rein Anton. Electrostatic focusing of electrospun polymer(peo) nanofibers. *Journal of Electrostatics*, 94:21 – 29, 2018.

[53] L.M. Bellan, J. Kameoka, and H.G. Craighead. Measurement of the young's moduli of individual polyethylene oxide and glass nanofibres. *Nanotechnology*, 16(8):1095, 2005.

[54] E. Loth. Drag of non-spherical solid particles of regular and irregular shape. *Powder Technology*, 182(3):342 – 353, 2008.